University of Canterbury

Master's Thesis

# Investigating the Requirements of 3D Dose Reconstruction via Optical Calorimetry

*A thesis submitted in fulfilment of the requirements for the degree of*
*Master of Science*
*in the Department of Physical and Chemical Sciences*

**June 2022**

| | |
|---|---|
| Author: | Thomas Telford |
| Supervisors: | Dr Alicia Moggré |
| | Dr Juergen Meyer |
| | Dr Steven Marsh |

# Abstract

Optical calorimetry (OC) is a novel form of radiation dosimetry that used two interfering beams of light to measure the radiation induced phase change in a volume of water, and relates the phase change to absorbed dose to water. It presents a promising dosimetric method for the measurement of FLASH therapy beams, where its measurement of dose to water, lack of components perturbing the radiation beam, and dose rate independence avoids many of the technical challenges facing traditional dosimetric methods in these ultra-high dose rate beams. The current OC dosimeter outputs a 2D image of dose, integrated across the volume of water. This study aims to investigate the requirements to accurately reconstruct a 3D dose distribution through performing a tomographic reconstruction upon the 2D OC dosimeter output.

Due to a desire to keep the mechanical complexity of a 3D OC dosimeter design minimised, this work looks at performing a single-projection reconstruction upon radially symmetric radiation beams using the inverse Abel transform, and performing a two-projection reconstruction on simple square and circular radiation beams using a filtered back projection or fast Fourier transform algorithm. A multi-projection reconstruction where the restriction on the number of projections used is removed was also performed, to indicate the level of mechanical complexity such an approach would entail if required.

Reconstruction results showed the single-projection inverse Abel transform method could reconstruct a manually integrated proton beam to an accuracy of better than 1%, but this error increased to 8% when using the projection data generated using the FRED virtual OC dosimeter model. This error could be reduced to below 4% when the level of noise in the FRED dosimeter model was reduced to 1/8th of the full amount, indicating that an accurate 3D reconstruction using a single projection is possible, but a substantial decrease in the noise within the detector system is required. The two-projection method performed accurately in some situations, did not reliably produce accurate reconstructions of simple photon beams with clinical features modelled. The multi-projection reconstruction investigation determined that at least 25 projections would be required to achieve a reconstruction with an error below 2% for all beams investigated, representing a significant increase in mechanical complexity of the OC dosimeter design.

The findings of this work recommend that in order to accurately reconstruct a 3D dose distribution using the OC dosimeter, the single-projection inverse Abel transform method could be used provided the noise in the dosimeter system is reduced, or the multi-projection FBP reconstruction method could be used provided that the additional mechanical complexity of such a design is accounted for.

# Acknowledgements

To my supervisor Alicia Moggré, thank you for all your tireless dedication and commitment throughout the entirety of this project. The constant encouragement and guidance on all thing's medical physics, and being available any time to help in any way possible. Thank you for sharing your scientific knowledge with me, and always challenging me yet encouraging me to get the most out of this project that I could. This thesis would not have been possible without you.

To my supervisor Steve Marsh, thank you for the endless enthusiasm for all things Fourier transform.  Thank you for the endless stream of new ideas and new areas we could investigate, I'm sorry we only got around to looking into half of them. Thank you for persevering through teaching me TOPAS, it can't have been easy, but it was worth it in the end. The enthusiasm you have shown throughout this project was inspirational. And thank you for helping start me off on my journey into the world of medical physics, you will always be the first person I think of when remembering how this all began.

To my supervisor Juergen Meyer, thank you for all the technical advice and wise words of wisdom throughout the duration of this project. The reminders of where we were sitting in the scheme of things, and stopping us from continuously charging off on tangents is one of the main reasons this thesis has gotten to the finish line as well as it has. Your knowledge of things protons, FLASH therapy and DHI, and the ability to explain it was truly invaluable. I will also forever aspire to be able to write a scientific sentence as elegantly as you can.

To my colleague Jackson Roberts, thank you for introducing me to the world of optical calorimetry. When you ran me through the prototype dosimeter and the work you were doing, it was the enthusiasm you showed for it that encouraged me to get on board. Your dedication to the project has been hugely inspirational for encouraging me to do as well on mine. Thank you for the endless guidance on everything FRED and DHI related, I would not have been able to get to where we are today without your support.

Finally, thank you to the Medical Physics and Bioengineering department at the Canterbury District Health Board for taking me on as a registrar and giving me the opportunity to undertake this project. The continued support from the entire Physics team is hugely appreciated, for all things both physics related and not.

# Contents

**Abstract** i

**Acknowledgements** ii

**Contents** iii

**List of Figures** v

**List of Tables** vii

**List of Abbreviations** viii

**Chapter 1: Introduction** .......... 1
- 1.1 Cancer and Radiation Therapy .......... 1
- 1.2 Radiation Dosimetry .......... 3
- 1.3 Research Aim .......... 5

**Chapter 2: Background** .......... 6
- 2.1 Overview of Dosimetry Systems .......... 6
- 2.2 Optical Calorimetry .......... 8
  - 2.2.1 Optical Interferometry .......... 9
  - 2.2.2 Digital Holographic Interferometry .......... 12
  - 2.2.3 The Cavan & Meyer DHI Dosimeter .......... 13
  - 2.2.4 The Optical Calorimetry Dosimeter .......... 15
- 2.3 Dosimetric Quantities and Terminology .......... 17
- 2.4 Tomography .......... 18
  - 2.4.1 Abel Transform .......... 18
  - 2.4.2 Filtered Back Projection .......... 22
  - 2.4.3 Fast Fourier Transform .......... 23
  - 2.4.4 Advanced Reconstruction Methods .......... 23
- 2.5 Concluding Remarks .......... 25

**Chapter 3: Simulation Methods** .......... 27
- 3.1 Radiation Beam Data Simulation .......... 27
- 3.2 Detector System Simulation .......... 31
- 3.3 Quantifying Reconstruction Accuracy .......... 33
  - 3.3.1 1D Gaussian Reconstruction .......... 34
  - 3.3.2 Inverse Abel Transform Reconstruction .......... 34
  - 3.3.3 Filtered Back Projection & Fast Fourier Transform Reconstructions .......... 37

**Chapter 4: Single Projection Reconstruction** .......... 38
- 4.1 *PyAbel* Functionality Tests .......... 38
  - 4.1.1 Gaussian Distribution Reconstruction .......... 39
  - 4.1.2 Proton Beam Reconstruction .......... 43
  - 4.1.3 Photon Beam Reconstruction .......... 46
  - 4.1.4 Concluding Remarks .......... 49

4.2 Proton Beam Reconstruction Characterisation .......... 49
  4.2.1 Filtering .......... 50
  4.2.2 Beam Size .......... 53
  4.2.3 Proton Beam Characterisation Conclusions .......... 55
4.3 FRED Projection Reconstruction .......... 55
4.4 FRED Dosimeter Noise Investigation .......... 61
4.5 Square Field Reconstruction .......... 64
4.6 Concluding Remarks .......... 64

**Chapter 5: Two Projection Reconstruction** .......... 67
5.1 Filtered Back Projection Reconstruction .......... 68
  5.1.1 FBP Filter Choice .......... 71
  5.1.2 Beam Size .......... 71
  5.1.3 Beam Intensity .......... 72
  5.1.4 Beam Noise .......... 74
  5.1.5 Beam Penumbra .......... 74
  5.1.6 Wedged Intensity Beam .......... 76
5.2 Fast Fourier Transform Reconstruction .......... 78
  5.2.1 Beam Size .......... 79
  5.2.2 Beam Intensity .......... 80
  5.2.3 Beam Noise .......... 81
  5.2.4 Beam Penumbra .......... 82
  5.2.5 Wedged Intensity Beam .......... 83
5.3 IMRT Field Reconstruction .......... 85
5.4 Two-Projection Reconstruction Concluding Remarks .......... 86
  5.4.1 Filtered Back Projection .......... 86
  5.4.2 Fast Fourier Transform .......... 87
  5.4.3 IMRT Beam Reconstruction .......... 88

**Chapter 6: Multi-Projection Reconstruction** .......... 89
6.1 Projection Number Investigation .......... 90
  6.1.1 Initial Reconstructions .......... 91
  6.1.2 Beam Noise .......... 93
  6.1.3 Wedged Intensity .......... 95
6.2 Concluding Remarks .......... 96

**Chapter 7: Discussion** .......... 98
7.1 Radially Symmetric Field Reconstruction .......... 99
7.2 Square Field Reconstruction .......... 105
7.3 Complex Field Reconstruction .......... 107
7.4 Future Work .......... 108

**Chapter 8: Conclusion** .......... 111

# List of Figures

Figure 1.1. Illustration of the dose-response curve ........ 3
Figure 2.1. Optical setup of Cavan & Meyer DHI dosimeter ........ 14
Figure 2.2. FRED virtual model of the OC dosimeter ........ 15
Figure 3.1. Beam penumbra comparison ........ 28
Figure 3.2. MATLAB simulated 6X photon beam ........ 29
Figure 3.3. Modelled IMRT radiation beam x-y slice ........ 30
Figure 3.4. TOPAS simulated 70keV proton beam ........ 31
Figure 3.5. TOPAS modelled 20mm proton beam distribution ........ 32
Figure 3.6. MATLAB modelled 160-pixel photon beam distribution ........ 33
Figure 3.7. PDD and $D_{max}$ Profile measurement locations ........ 35
Figure 3.8. Dosimetrically relevant areas of accuracy analysis ........ 36
Figure 4.1. Inverse Abel transform asymmetric Gaussian reconstruction ........ 40
Figure 4.2. Inverse Abel transform reconstruction of a symmetric Gaussian ........ 41
Figure 4.3. Inverse Abel transform TOPAS modelled proton beam reconstruction accuracy ........ 43
Figure 4.4. Onion Bordas inverse Abel transform profile reconstruction accuracy ........ 44
Figure 4.5. Onion Bordas inverse Abel transform PDD reconstruction accuracy ........ 45
Figure 4.6. Inverse Abel transform photon beam profile reconstruction accuracy ........ 48
Figure 4.7. Filtering of TOPAS proton beam profiles ........ 50
Figure 4.8. Reconstruction error with different levels of filtering ........ 51
Figure 4.9. Effects of filtration on reconstruction error ........ 52
Figure 4.10. Reconstruction error as a function of beam size ........ 53
Figure 4.11. Narrow beam inverse Abel transform reconstruction ........ 54
Figure 4.12. TOPAS 35mm proton beam inverse Abel transform reconstruction ........ 55
Figure 4.13. Comparison of integrated projection images of a 30mm TOPAS proton beam ........ 56
Figure 4.14. Effects of beam size on the FRED integrated projection data ........ 57
Figure 4.15. The effects of filtering on the FRED generated projection data ........ 58
Figure 4.16. Reconstruction error for levels of filtering of FRED projection data ........ 58
Figure 4.17. Effects of filtration on FRED projection reconstruction accuracy ........ 59
Figure 4.18. $D_{max}$ profile comparison for FRED integrated projection data ........ 61
Figure 4.19. FRED projections with different levels of modelled noise ........ 62
Figure 4.20. Reconstruction error for FRED projections with varying noise ........ 63
Figure 4.21. Single-projection reconstruction of a MATLAB modelled square field ........ 64
Figure 5.1. Initial two-projection FPB reconstruction attempts ........ 69

Figure 5.2. Relationship between the reconstruction error and dose ....................................... 73
Figure 5.3. Effects of penumbra on two-projection FBP rectangular field reconstruction ......... 76
Figure 5.4. Wedged intensity beam two-projection FBP reconstruction profile comparison ..... 77
Figure 5.5. Initial two-projection FFT reconstruction attempts .................................................. 78
Figure 5.6. Effects of noise on the two-projection FFT reconstruction ...................................... 82
Figure 5.7. Effects of penumbra on two-projection FFT rectangular field reconstruction .......... 83
Figure 5.8. Two-projection FFT reconstruction accuracy for wedged intensity square fields ..... 84
Figure 5.9. Two-projection reconstruction of an IMRT dose distribution .................................. 86
Figure 6.1. FBP reconstruction accuracy metrics with increasing numbers of projections ......... 91
Figure 6.2. Multi-projection IMRT field FBP reconstruction ....................................................... 92
Figure 6.3. Multi-projection FBP reconstruction of an IMRT beam with modelled noise ........... 94
Figure 6.4. Multi-projection FBP IMRT beam with noise profile comparison ............................ 94
Figure 6.5. FBP wedged beam reconstruction accuracy and number of projections................... 95
Figure 6.6. Multi-projection FBP reconstructed wedged square beam profile comparison ....... 96

# List of Tables

Table 4.1 Inverse Abel transform asymmetric Gaussian reconstruction accuracy ..................... 40

Table 4.2 Inverse Abel transform symmetric Gaussian reconstruction accuracy ........................ 42

Table 4.3. Inverse Abel transform proton beam profile reconstruction accuracy ...................... 44

Table 4.4. Inverse Abel transform proton beam PDD reconstruction accuracy .......................... 45

Table 4.5. Inverse Abel transform photon beam profile reconstruction accuracy ...................... 47

Table 4.6. Inverse Abel transform photon beam PDD reconstruction accuracy .......................... 48

Table 4.7. FRED data reconstruction accuracy for different inverse Abel transform methods .. 60

Table 5.1. Two-projection FBP reconstruction accuracy with filter ............................................ 71

Table 5.2. Two-projection FBP reconstruction accuracy with field size ..................................... 72

Table 5.3. Relationship between dose and pixel value for FRED modelled radiation beams . .... 73

Table 5.4. Two-projection FBP reconstruction error for various levels of added noise ............. 74

Table 5.5. Two-projection FBP reconstruction accuracy with penumbra width ......................... 75

Table 5.6. Two-projection FBP reconstruction accuracy for a variety of wedge angles ............. 77

Table 5.7. Two-projection FFT reconstruction accuracy for a variety of beam sizes .................. 80

Table 5.8. Two-projection FFT reconstruction accuracy with beam intensity ............................ 81

Table 5.9. Two-projection FFT reconstruction accuracy with modelled noise levels ................. 81

Table 5.10. Two-projection FFT reconstruction accuracy with penumbra width ........................ 83

Table 5.11. Two-projection FFT reconstruction accuracy with wedge angle .............................. 84

Table 5.12. Two-projection IMRT field reconstruction accuracy................................................. 85

# List of Abbreviations

| | |
|---|---|
| **1D** | One-Dimensional |
| **2D** | Two-Dimensional |
| **3D** | Three-Dimensional |
| **AAPM** | American Association of Physicists in Medicine |
| **CT** | Computed Tomography |
| **CAX** | Central Axis |
| **DHI** | Digital Holographic Interferometry |
| $\mathbf{D_{max}}$ | Depth of Dose Maximum |
| **DNA** | Deoxyribonucleic Acid |
| **EBRT** | External Beam Radiation Therapy |
| **FBP** | Filtered Back Projection |
| **FFT** | Fast Fourier Transform |
| **FT** | Fourier Transform |
| **HeNe** | Helium-Neon |
| **IAEA** | International Atomic Energy Agency |
| **ICRU** | International Commission on Radiation Units and Measurements |
| **IMRT** | Intensity Modulated Radiation Therapy |
| **kV** | Kilovoltage |
| **MC** | Monte Carlo |
| **MRI** | Magnetic Resonance Imaging |
| **MV** | Megavoltage |
| **MeV** | Mega electron-volts |
| **NTCP** | Normal Tissue Complication Probability |
| **OC** | Optical Calorimetry |
| **OPL** | Optical Path Length |
| **PDD** | Percentage Depth Dose |
| **RMSE** | Root Mean Square Error |
| **ROI** | Region of Interest |
| **TCP** | Tumour Control Probability |

# Chapter 1: Introduction

## 1.1 Cancer and Radiation Therapy

Cancer is the unrestrained proliferation of cellular growth resulting from mutations within a cell's deoxyribonucleic acid (DNA), which if left untreated it can lead to severe illness or death [1]. Worldwide in 2020, it was estimated 19.3 million new cancer cases occurred, with 10 million deaths resulting from some form of cancer [2]. Due to population growth and an aging population the number of new cancer cases are projected to increase by nearly 50% to 28.4 million by 2040, indicating a growing need for cancer treatments worldwide. A similar trend is seen in New Zealand cancers statistics, with 24,500 new cancer registrations and 9600 deaths due to cancer in 2017, an increase from 16,000 and 7,300 respectively in 1997 [3]. The annual cost of registered cancers on the NZ health care system was estimated at $500 million in 2011 [4]. The most common treatment options for a cancer patient include surgery, chemotherapy, radiation therapy, or some combination of the above [5,6]. There are advantages and disadvantages to each of the treatment options, a compromise between the effectiveness of the treatment, the local versus systemic effect of the treatment, and the short- and long-term side effects of the treatment, which vary between the different sites within the body cancer can occur [7,8]. It is a common estimate that 50% of all cancer patients would benefit from radiation therapy, either as the primary treatment modality, in addition to chemotherapy or surgery, or a combination of all three [9].

The aim of a radiation therapy treatment is to deliver a lethal dose of radiation to a target volume within the patient, while minimising the dose delivered to the surrounding healthy tissues [10]. The high energy ionizing radiation used is highly damaging to tumour cells, but the amount of dose required to eliminate all cancerous cells can also be damaging to healthy tissue. Radiation prescriptions for various sites within the body are therefore carefully determined from evidence-based research, considering both the dose required to eradicate the tumour and the potential for radiation induced side effects [8,11–13].

The most common form of radiation therapy is External Beam Radiation Therapy (EBRT) [14,15]. This can come in several different forms, including megavoltage (MV) photon beams, mega electron-voltage (MeV) electron beams, or kilovoltage (kV) photon beams. Clinically, MV photons beams delivered from a treatment unit such as a linear accelerator are the most frequently used, where multiple radiation fields can be delivered from different beam angles around the patient. This results in the individual beams converging to deliver a conformal dose to the target volume, a volume consisting of the tumour mass with added margins to account to microscopic spread of the tumour and uncertainties during the treatment delivery [16–18].

For a radiation therapy treatment, the outcome for the patient is dependent on the amount and location of the dose delivered. Insufficient dose to the tumour volume can result in survival of some tumour population, increasing the risk of recurrence of the cancer. On the other hand, if too much dose is delivered this can increase the risk and severity of radiation induced side effects in the treated region [19]. This compromise can be demonstrated with a plot of dose response curves, as shown in Figure 1.1. The tumour control probability (TCP) is the probability that a given dose will result in eradication of a tumour, while the normal tissue complication probability (NTCP) is the probability of radiation induced side effects occurring in healthy tissue. The shape of the TCP and NTCP curves and the relative spacing between them is dependent on the location and stage of the tumour, and the location and radiosensitivity of the healthy tissue surrounding this. The difference between the TCP and NTCP probability curves for a certain level of dose is known as the therapeutic window [20]. The larger the therapeutic window, the greater chance of achieving elimination of the tumour while keeping the probability of side effects occurring low. The size of the therapeutic window is very sensitive to the amount of dose delivered. As shown in Figure 1.1, as the dose is decreased slightly from $D_1$ to $D_2$ this can result in a large decrease in the TCP for only a small reduction in the NTCP.

Alternatively, a small increase in dose would result in a large increase in NTCP for only a small increase in the TCP. Optimising the dose delivered in a treatment to maximise the therapeutic window is crucial to achieve the best possible outcomes for the patient. Therefore, a high level of accuracy in the amount of dose delivered for a radiation therapy treatment is required [21].

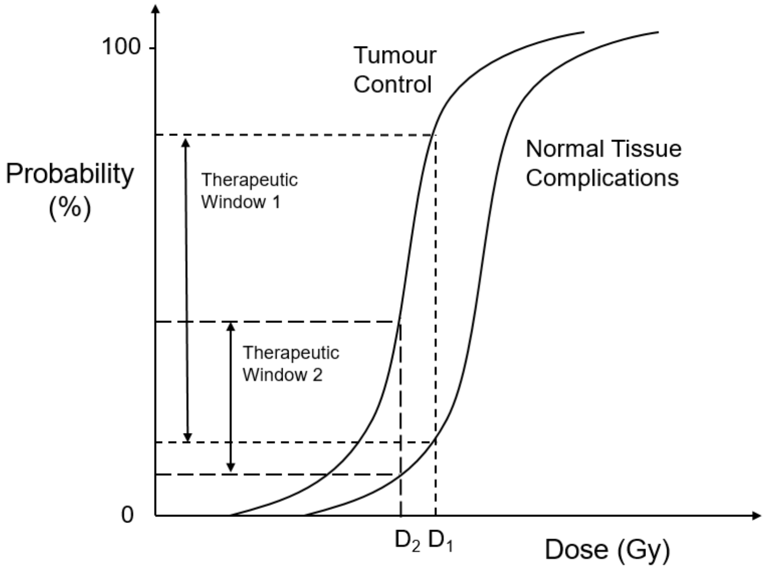

*Figure 1.1. Illustration of the dose-response curve. This shows the relationship between the dose delivered in a radiation therapy treatment and the TCP and NTCP. Two therapeutic windows are shown, relating to the doses $D_1$ and $D_2$. Note the small change in dose resulting in a large change in the position of the treatment on the TCP and NTCP curves, causing a large change in the size of the therapeutic window for that amount of dose.*

New treatment techniques have been developed in recent years that aim to increase the therapeutic window of a radiation therapy treatment, such as FLASH therapy [22,23]. FLASH therapy utilizes ultra-high dose rate radiation beams and is characterised by a reduction in the normal tissue complication rate compared to conventional approaches. However, one of the issues preventing the widespread clinical implementation of this technique is the challenge of accurately measuring the radiation dose from these beams [24–29].

## 1.2 Radiation Dosimetry

Radiation dosimetry describes the measurement of absorbed dose. Dose is the quantity used to measure the amount of energy deposited into a medium by a beam of radiation, and is defined as the quotient of mean energy $d\varepsilon$ imparted to matter of mass $dm$ by ionising radiation. The SI units of dose are joules of energy per kilogram of mass (J $kg^{-1}$), also known as the Gray (Gy).

$$D = \frac{d\bar{\varepsilon}}{dm}. \tag{1.1}$$

Recommendations from the International Commission on Radiation Units and Measurements (ICRU) [18,30] are that the dose delivered to the target volume in a radiation therapy treatment needs to be within ±5% of the prescribed dose. This uncertainty can be divided into two separate aspects of a radiation treatment, the geometric uncertainty associated with patient setup and target volume positioning, and the dosimetric uncertainty based on the amount of dose delivered from the treatment machine [31]. Current clinical dosimetry practises use international dosimetry protocols such as the International Atomic Energy Agency (IAEA) TRS-398 [32] or American Association of Physicists in Medicine (AAPM) TG-51 [33]. Careful adherence to these procedures allows the determination of absorbed dose to water to a combined standard uncertainty of 1.5 – 2%.

As the dose is dependent on the mass of the volume in which it is measured, the choice of medium for this volume of mass is non-trivial. In clinical dosimetry, the quantity of interest is the amount of dose deposited within the patient. Measurements within a patient is not possible, so water is commonly used as a surrogate, as it has similar radiation scattering and absorption properties to soft tissue and is a convenient medium in which to make measurements [34]. Therefore, dose to water is widely considered to be the standard quantity for dosimetric reference and calibration measurements [32,33].

Many types of dosimetry systems are available for making clinical dose measurements. These include ionometric, calorimetric, and chemical, where dose is related to charge, heat, or a molecular change respectively [35]. These methods are described in more detail in Section 2.1. Each method has various strengths and limitations, making it more suited to specific dosimetric applications. For ultra-high dose rate dosimetry however, these traditional methods have limitations, and there is a need for research and development into novel approaches to accurately quantify dose for FLASH beams [24,25,28].

Optical Calorimetry (OC) is a novel dosimetry technique with the potential to overcome a number of the inherent challenges in ultra-high dose rate FLASH dosimetry. OC uses interfering light waves to measure the radiation induced phase change in a volume of water, then relates this back to absorbed dose [36,37]. It has high spatial resolution, can be used at very high dose rates, and can measure two-dimensional (2D) dose distributions. OC measures the dose in water rather than dose in some non-water medium, and has no components of the detector perturbing the radiation beam like in an ionization chamber, so the amount of correction factors required to determine the dose to water is reduced. This has the potential to decrease the uncertainty in the measurements, especially for novel radiation treatments for which these correction factors have not been well established.

Current OC measurements capture a 2D image of integrated dose across a measurement volume, but the potential expansion of optical calorimetry into three-dimensions (3D) has not yet been investigated. To expand to 3D, the 2D integrated dose images would need to be generated from different directions, then a tomographic reconstruction performed to obtain a full 3D dose distribution. This could have large clinical benefits, as a full characterisation of the dose distribution resulting from FLASH therapy beams could potentially be generated from a single measurement, helping address current limitations in FLASH dosimetry.

## 1.3 Research Aim

The aim of this work is to develop a framework for 3D dose reconstruction for an OC dosimeter and investigate the requirements to measure absolute and relative 3D dose distributions. Tomographic reconstruction methods will be investigated to determine the accuracy of 3D dose distributions generated from the OC dosimeter output and make recommendations as to the most suitable approach. The findings of this study will determine the feasibility of and guide the design for the future construction of a prototype 3D OC dosimeter.

# Chapter 2: Background

This chapter provides background on current dosimetry systems, the existing optical calorimetry dosimeter, and how OC has several inherent advantages for use in FLASH dosimetry. The operation of the OC dosimeter will be detailed, along with the physical principles of optical interferometry, digital holographic interferometry, and optical calorimetry on which it is based. Efforts made to create a virtual model of the dosimeter, the verification of this virtual dosimeter, and the use of this in the ongoing refinement of the OC dosimeter will be described. This is followed by a brief overview of several tomographic reconstruction methods used throughout this study.

## 2.1 Overview of Dosimetry Systems

The ideal dosimetry system required for novel delivery techniques such as FLASH therapy would be capable of measuring dose to water with high accuracy and precision, with a large dynamic range and high spatial resolution. The detector response should be linearly related to the amount of dose delivered and be independent of the dose rate of the radiation beam, the beam quality or energy of the beam, and the beam direction. Readout of the detector should be instantaneous, and the system itself should be robust and practical to use. Current dosimetric systems can be broadly categorised into three main methods: calorimetric, ionometric and chemical. While each of these methods share several features with the hypothetical perfect dosimeter described above, each has drawbacks associated with it also.

Calorimetric dosimetry, such as the use of a water calorimeter, is the measurement of the radiation induced temperature increase in a medium, resulting from the transfer of energy to the medium from the radiation in the form of heat [38]. The temperature increase can be related to the energy transferred using the specific heat capacity of the medium. A calorimeter provides a measurement of dose with high accuracy and precision, which is independent of dose rate and energy. Calorimetry can measure absolute dose to water directly, making it the choice of dosimeter for many primary standard dosimetry labs worldwide [39]. But the spatial resolution of a calorimeter is limited by the dimensions of the temperature reading probe, and the presence of this physical probe perturbs the radiation beam, changing the absorbed dose due to scattered radiation. Calorimeters also tend to be large in design, making them impractical for routine clinical dosimetry purposes [40,41].

Ionometric dosimetry, such as the use of a gas-filled ionization chamber or a diode, uses two charged electrodes collect to radiation induced charged particles, generating a current that is measured with an electrometer. This is generally the standard method of routine clinical dosimetry, as ion chambers and diodes are small, robust, and practical to use, provide an instantaneous readout, and measure dose with high accuracy and precision. But a gas filled chamber with a metallic electrode, or a silicon diode are both different mediums to water, so to convert the measured charge into a dose to water several corrections must be applied [42]. Further correction factors must also be applied to account for the perturbation of the radiation fluence by the detector itself. The spatial resolution of an ion chamber is fundamentally limited by the size of the chamber, as the measured dose is averaged throughout the sensitive volume of the chamber. The chamber response is also highly dependent on the beam quality, with different correction factors required for each energy in which it is used. The number of correction factors required to modify the measured quantity to calculate dose results in an increased overall measurement uncertainty [43–46].

Chemical dosimetry is a class of radiation measurement where the chemical composition of the detector is altered upon exposure to radiation. Common examples of chemical dosimetry include the Fricke dosimeter, where the radiation induced conversion of $Fe^{2+}$ to $Fe^{3+}$ ions is measured [35,47], and radiochromic film, where the polymerisation of molecules due to radiation causes darkening of the film [48–50]. The Fricke dosimeter can be imaged using Magnetic Resonance Imaging (MRI) or Computed Tomography (CT), the conversion of Fe ions quantified and related back to dose. Radiochromic film can use a flatbed scanner to determine the pixel values at each point on the film and relate this back to dose using a calibration curve for that batch of film. Both these forms of dosimetry have excellent spatial resolution, limited only by the performance of the readout device. Film can measure film in two dimensions, the Fricke dosimeter three dimensions, allowing for information of both the amount and the distribution of dose. The downside of these approaches includes the long processing and readout procedure, with radiochromic film most accurate after it had had 24 hours to develop [50], and Fricke dosimeters requiring MRI or CT access. This means the dose measured can remain unknown until the next day, limiting the clinical usefulness of the measurements in any situation that requires instant feedback of results. The chemical composition can vary between batches also, resulting in film requiring a calibration curve for every film batch produced, for example [50]. These dosimetry systems are single use only, and require careful handling, setup, and processing to produce accurate results, making chemical dosimetry more expensive and less practical than ionometric dosimetry for many applications.

## 2.2 Optical Calorimetry

Optical Calorimetry is a novel dosimetry technique that has the potential to overcome limitations of current dosimetry approaches for non-conventional radiation beams, such as those in ultra-high dose rate FLASH therapy [36]. OC uses two interfering light waves to measure the radiation induced phase change in a volume of water. This phase change can then be directly related back to absorbed dose, allowing for calculation of absorbed dose to water. Optical calorimetry is built upon the holographic interferometry dosimetric techniques of Hussmann [51,52] and Miller [53,54] in the 1970’s, before technological and computational advances lead to the development of a prototype Digital Holographic Interferometry (DHI) dosimeter by Cavan & Meyer in 2014 [36,55]. This prototype has since undergone refinement by Hubley [37], and Roberts [56–59], to form the current OC prototype dosimeter which is the focus of this study.

OC dosimetry has several advantages over traditional dosimetry techniques such as ionisation chambers, diodes, and film:

1. Direct measurement of absorbed dose to water, rather than measuring dose to a non-water medium such as air, removing the need for correction factors to convert the measured reading back to dose to water.
2. Minimal perturbation of the radiation field by the detector, as all the measurement system sits externally to the radiation beam, removing the need for correction factors to compensate for changes to the beam fluence during the measurement process.

The correction factors involved with traditional dosimetry techniques, such as for converting dose to air to dose to water or to account for the perturbation of the radiation field by the detector, are well understood and characterized for conventional dosimetry. These correction factors are less understood for FLASH therapy treatment techniques, so the corresponding uncertainties when measuring these ultra-high dose rate fields with traditional detectors are higher [60]. By measuring dose to water and not perturbing the radiation beam, optical calorimetry avoids the need for the same correction factors, presenting a potential dosimetry option with less measurement uncertainty.

3. Dose is measured with a high spatial resolution, decreasing the volume averaging effects inherent with radiation detector of a finite size such as an ionisation chamber or diode.
4. Detector response is independent of dose rate, an important characteristic for the measurement of FLASH beams [59].
5. The output of the OC dosimeter is a 2D map of integrated dose, allowing for the simultaneous acquisition of the dose variation across the entire radiation field.

These advantages position optical calorimetry as a promising tool for FLASH dosimetry. The fundamental principles underlying the function of the prototype OC dosimeter, and the development and refinement the prototype dosimeter has undergone are detailed in the following sections.

### 2.2.1 Optical Interferometry

Interferometry is a field of measurement where the interference between two light waves is used to measure a perturbation to a system, such as a change in refractive index or a microscopic displacement, where this change results in the alteration to the path length of one of the light waves [61]. The basics of interferometry can be explained through the principles of light.

Light is a transverse electromagnetic wave, with separate electric and magnetic field components oscillating orthogonally to the direction of travel. A laser light source can be plane polarized, meaning the electric and magnetic field components each oscillate within a single plane, and coherent, meaning the frequency of the wave is stable both spatially and temporally. A plane polarized wave at position $\vec{r}$ at a time $t$ can be described by the harmonic wave equation:

$$\vec{E}(\vec{r},t) = \overrightarrow{E_0}\cos\left(\vec{k}\vec{r} - \omega t + \phi\right), \tag{2.1}$$

where $\overrightarrow{E_0}$ is the real amplitude of the wave, $\phi$ the phase of the wave, $\vec{k}$ the wave number and $\omega$ the angular frequency of the wave. The wave number is related to the wavelength $\lambda$ of the wave by the relation:

$$\vec{k} = \frac{2\pi}{\lambda}, \tag{2.2}$$

while the angular frequency is related to the wavelength by:

$$\omega = \frac{2\pi c}{\lambda}, \tag{2.3}$$

where $c$ refers to the propagation speed of the wave in a medium, or the phase velocity. The intensity $I$ of a light wave is the parameter of the wave that a sensor can directly detect, and is proportional to the square of the electric field strength averaged over time:

$$I \sim \left|\overrightarrow{E_0}\right|^2. \tag{2.4}$$

The refractive index is a property that describes the optical density of a medium. For a given wavelength of light, it is defined as the ratio of the phase velocity of the light in a vacuum $c$ to the phase velocity in the medium $v$:

$$n = \frac{c}{v}. \tag{2.5}$$

The higher the refractive index, the more optically dense that medium is, and the slower light will travel through that medium. For a light wave propagating through a medium, the Optical Path Length (OPL) is defined as the product of the refractive index of that medium and the geometric distance $d$ the light travels in that medium:

$$OPL = nd\,. \tag{2.6}$$

Light waves travelling the same geometric distance through two media of different refractive index would each travel a different optical path length. This difference in the optical path lengths travelled by the waves is related to the difference in the phase between the two light waves:

$$\Delta OPL = \frac{\lambda \Delta \phi}{2\pi}. \tag{2.7}$$

By combining equations 2.6 and 2.7, for two light waves travelling the same geometric distance through two mediums of different refractive index, the difference in refractive index between the two mediums can be related to the change in optical path length, and in turn the change in phase between the two light beams:

$$\Delta \phi = \frac{2\pi d \Delta n}{\lambda}. \tag{2.8}$$

Interference is caused by the superposition of two light waves overlapping in space, the two individual waves combining to create a single wave. The combined intensity of two interfering waves, $I_1$ and $I_2$, with the same frequency and polarisation is given by:

$$I = I_1 + I_2 + 2\sqrt{I_1 I_2}\cos\Delta\phi\,, \tag{2.9}$$

where $I_1$ and $I_2$ are the intensities of the two individual incident waves, and $\Delta\phi = \phi_1 - \phi_2$ is the phase difference between the two waves. The third term in equation 2.9 determines the nature of the interference as it varies sinusoidally with the phase difference. Constructive interference occurs when $\cos\Delta\phi$ is at its maximum ($\Delta\phi = 0, 2\pi, 4\pi, \dots$), while destructive interference occurs when $\cos\Delta\phi$ is at its minimum ($\Delta\phi = -\pi, \pi, 3\pi, \dots$). When a plane through the interfering light waves is viewed, the constructive and deconstructive interference processes result in a series of alternating light and dark bands known as interference fringes. The spacing of these fringes is dependent on the rate of variation of the phase difference between the two light waves, with a more rapidly varying phase producing more narrow fringes.

An interferometer uses the interference fringe distribution to determine the phase difference between the two interfering light waves. This phase difference can then be related back to the change in OPL, and then to the change in refractive index. From there, the perturbation to the system causing the change in refractive index can be calculated. For the case of OC dosimetry, this perturbing factor is the radiation absorbed dose.

### 2.2.2 Digital Holographic Interferometry

Holographic interferometry is a form of optical interferometry, allowing for the reconstruction of both the amplitude and phase of the image wave [62]. A simple holographic interferometer can be setup with two interfering waves: the object beam, which probes the object of interest, and the reference beam, which passes only through air. The object of interest has a different refractive index to air, so the object beam travels a different OPL relative to the reference beam as it traverses the object of interest, resulting in a different phase change between the object and reference beams over the same geometric distance. When the two beams recombine the phase difference between them results in the formation of an interference pattern, called an optical interferogram, which is captured on a detector such as film or a digital camera. The recorded interferogram is then re-illuminated by the reference beam, causing an image of the original object beam to form. This reconstructed image is known as a hologram. When two holograms of two different states of the object of interest are captured, the difference between the two states can be used to extract information about the change in the object wave between the two states. For interferograms produced by holographic interferometry, the reconstructed fringe patterns correspond to the phase difference between the object and reference waves. This process is simplified compared to classical interferometry, where the recorded fringe patterns must be analysed for each state of the object, then compared to calculate the phase difference.

Digital holographic interferometry (DHI) is a further advancement of this process, first developed in 1994 by Schnars and Jupner [63,64]. Advances in optical sensor technology and increases in computer processing power allow for the digital recording of interferograms, and for the use of numerical algorithms for hologram reconstruction. The digital technique removes the film development and realignment steps, leading to time savings and reduced positional uncertainties compared to the film technique. Interferograms can be digitally captured in real time at a high frame rate, from which phase information at any point in the image can be obtained for each recorded state of the object. Any of these recorded states can be used as the reference interferogram which changes to the system are compared against. This provides another advantage over film-based methods, where the reference interferogram is generated prior to the object measurements. The reduction in time differences between the reference and object states leads to increased reliability of the results.

### 2.2.3 The Cavan & Meyer DHI Dosimeter

The DHI technique can be applied to radiation dosimetry, creating the technique known as optical calorimetry. DHI is used to calculate the radiation induced phase difference between irradiated and reference states of a volume of water. The absorbed dose to water can then be calculated from the phase difference. The operation of the Cavan & Meyer DHI dosimeter, from which the OC dosimeter of this study was developed are described in this section, while the further refinement of this dosimeter by Hubley and Roberts are described in Section 2.2.4. Further details on this work can be found in [36,37,57].

The first step is to probe a test cell of water with an optical interferometer. A coherent helium-neon (HeNe) laser is split into two beams, the object beam passing through the test cell and the reference beam passing through air. The greater refractive index of water relative to air causes the object beam to travel a larger optical path length compared to the reference beam, resulting in a phase difference between the two beams. The phase difference between the beams causes an interferogram to form, which is recorded digitally on a CMOS camera chip. Interferograms are captured for both the unirradiated reference state and irradiated state of the test cell. The irradiated state corresponds to a certain dose delivered to the test cell with ionising radiation. A schematic diagram and the setup of the original Cavan & Meyer DHI dosimeter is shown in Figure 2.1.

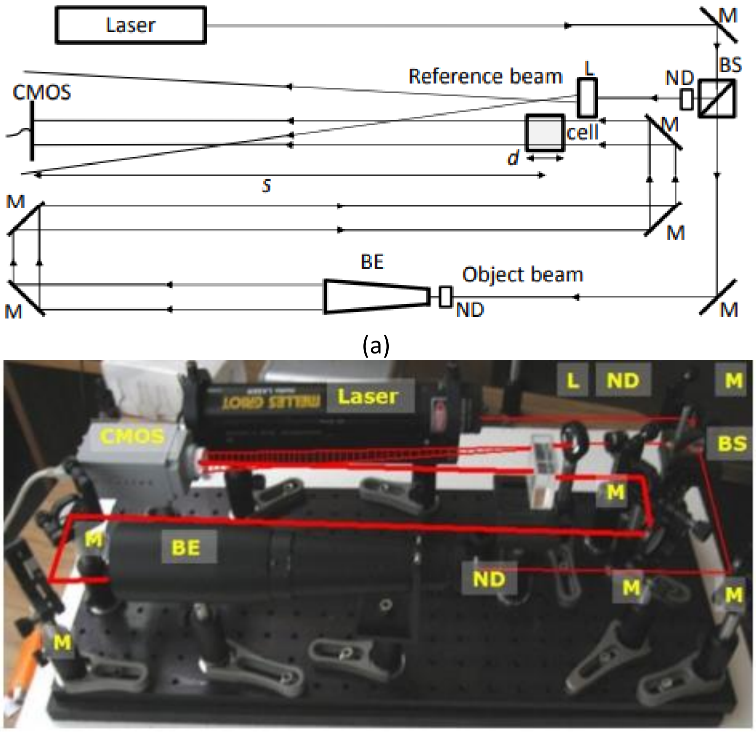

(a)

(b)

*Figure 2.1. Optical setup of Cavan & Meyer DHI dosimeter. Schematic diagram (a) and dosimeter setup with laser path and component labels indicated (b). M, ND, BS, BE and L denote mirror, neutral density filter, beam splitter, beam expander and lens respectively. Reproduced with permission from Cavan & Meyer (2014) [36].*

The interferograms are then reconstructed in MATLAB (The Mathworks, Natik, MA) to extract the phase. The interference patterns of the individual interferograms are digitally re-illuminated by the reference wave, and the Fresnel transform used to extract a 2D map of the phase information of the object wave. This is done for both the irradiated and un-irradiated interferograms, resulting in a 2D map of phase difference between the two states known as the interference phase. This represents the phase change of the object wave integrated across the dimension of the test cell along the laser path.

Once the interference phase is determined, the phase difference $\Delta\phi(X_I, Y_I)$ is related to the dose for each point in the 2D map. The change in optical path length $\Delta OPL(X_I, Y_I)$ is determined from the change in phase using equation 2.7, from which the change in refractive index $\Delta n(X_I, Y_I)$ is calculated using equation 2.8. Using the relationship between $\Delta n$ and $\Delta T$ [65] the temperature increase $\Delta T(X_I, Y_I)$ in the water due to energy absorption of the ionizing radiation is determined from the change in refractive index. Finally, the absorbed dose to the water cell can be determined from the equation

$$D(X_I, Y_I) = c_m \Delta T(X_I, Y_I)\,, \tag{2.10}$$

where $c_m$ is the specific heat of water [66]. $D(X_I, Y_I)$ is a 2D map of the dose, integrated over the width of the test cell in the direction of the object beam, at each point $X$ and $Y$ within the image.

### 2.2.4 The Optical Calorimetry Dosimeter

The development of the Cavan & Meyer DHI dosimeter proved that DHI was a viable technique for radiation dosimetry [36,55]. The current OC dosimeter is a refined and improved version of this original design [37,56,57]. To drive development of the prototype dosimeter design used in previous work, a virtual model of the dosimeter was created in the optical modelling software FRED (Photonics Engineering, Tucson, AZ). The virtual OC dosimeter model in FRED is displayed in Figure 2.2.

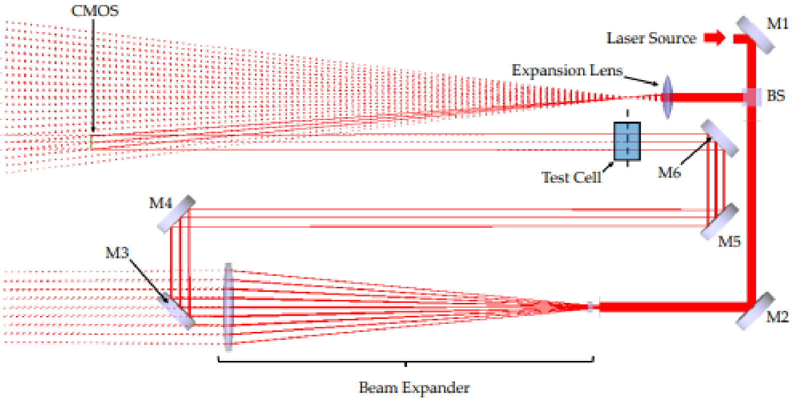

*Figure 2.2. FRED virtual model of the OC dosimeter. Reproduced with permission from Hubley et al (2019)* [37].

Each individual optical component was created within FRED, with the material, geometry and coating parameters set according to manufacturer specifications and adjusted to match experimental findings, until the full DHI dosimeter was virtually reconstructed. The ability of the virtual FRED model to determine simple dose distributions was tested, and comparison of experimental interferograms to simulated interferograms indicate the virtual dosimeter accurately reproduced the output of the experimental dosimeter, validating the use of the virtual dosimeter model as a surrogate for the real-life prototype dosimeter [37,56]. A series of modifications to the OC dosimeter to improve its performance were then developed, including path length equalisation, miniaturisation, external vibration isolation and the addition of temperature-controlled housing. For each change the improvement to the accuracy of the dosimeter was predicted using the virtual FRED model, then verified using experimental measurements [57,58].

The current study will expand on this earlier work, using both manually generated projections and the virtual dosimeter model in FRED to simulate the generation of projection data via the OC dosimeter. A tomographic reconstruction, as described in Section 2.4, will then be performed on these projections, and the ability to reconstruct a 3D dose distribution from the OC dosimeter output investigated. One consideration that must be made when developing any 3D dosimeter based on the current OC dosimeter design is the mechanical complexity of the design. The OC dosimeter is designed to determine temperature changes of a few ten-thousandths of a degree, so is required to be extremely sensitive to detect the corresponding changes in refractive index. As such, this means the dosimeter is also extremely sensitive to any alignment or positioning errors, mechanical vibrations, and atmospheric turbulence [37]. As shown by the dosimeter performance improvements when the setup was miniaturised and the path lengths equalised, the dosimeter is sensitive to the size and layout of the optical component also.  Mechanical complexity is used here as a general term to describe all these factors. For the successful expansion of the OC dosimeter to three dimensions, a solution which results in minimal increase to the mechanical complexity of the dosimeter is strongly desired.

## 2.3 Dosimetric Quantities and Terminology

Several relevant dosimetric quantities are frequently referred to throughout this study, as these are commonly used to characterise clinical radiation beams. These quantities are defined below:

- Depth of Dose Maximum ($D_{max}$) - the depth along the central axis (CAX) of the radiation beam corresponding to the point of maximum dose in that radiation beam.
- Percentage Depth Dose (PDD) - a plot of the central axis absorbed dose at different depths of a radiation beam, as a percentage on the maximum dose [32,67].
- Profiles – a plot of the absorbed dose at different lateral points at a constant depth across a radiation beam, normalised to the dose at the central axis [32,67].
- Bragg Peak – specific to proton radiation, where dose deposited is inversely proportional to the square of the velocity of the particles [68]. This results in an initially low rate of dose deposition, before most of their energy is deposited in a narrow depth range as they come to a stop. This results in the proton PDD having an extended, low dose build-up region followed by a large peak at a specific depth, before rapidly falling off past this point. This peak is known as the Bragg Peak, the depth of which is energy dependent [69].
- Flatness – for photon and electron beams, the ratio of the maximum to minimum dose within the central region of the radiation beam [70]. For proton beams, lateral flatness is defined as the ratio of the difference between the maximum and minimum dose to the sum of the same doses [71,72].
- Symmetry – for photon and electron beams, the maximum value of the ratio of the dose at points an equal distance from the CAX over the central region of a lateral profile [70]. For proton beams, lateral symmetry is defined as the ratio of the difference between the integral dose in each half of the lateral profile to the sum of the same doses [71,72].
- Penumbra – due to the scattering that occurs as radiation interacts with a medium, the edge of a radiation beam is slightly blurred rather than sharp. The extent of this blurring is

quantified with the penumbra, the part of the beam profile that is between 20% and 80% of the CAX dose [70].

- Wedged intensity fields – the radiation field is modified so it is non-uniform in one direction. Commonly used in photon 3D conformal radiation therapy treatments to achieve a uniform dose distribution within the target volume, when correcting for irregular surface contours, oblique beam angle incidence, or tissue inhomogeneities [73].

## 2.4 Tomography

A tomographic reconstruction generates a three-dimensional image from two-dimensional input data. This section will cover the three tomographic reconstruction algorithms investigated in this study, namely the inverse Abel transform, filtered back projection, and the fast Fourier transform. Some advanced reconstruction techniques that were outside the scope of this study to investigate, but could be implemented in any future work, are also mentioned.

### 2.4.1 Abel Transform

To generate the projection of a radially symmetric 3D object onto a 2D surface, the mathematical operation known as the forward Abel transform can be used, for situations where the axis of radial symmetry of the object distribution is parallel to the plane upon which the projection is captured [74]. The inverse Abel transform is the reverse of this process, where the 2D projection is used to reconstruct the original 3D distribution. The Abel transform is commonly used in fields such as flame and plasma flume analysis, plasma spectroscopy, and the imaging of 2D charged particle distributions [75–78].

Mathematically, the forward Abel transform is given by

$$F(y,z) = 2\int_{y}^{\infty} \frac{f(r,z)r}{\sqrt[2]{r^2 - y^2}} dr \,, \tag{2.11}$$

where $y$ and $z$ describe the spatial coordinates of the 2D projection and $r$ and $z$ describe the spatial coordinates of the 3D distribution. $F(y,z)$ is the intensity of the projection in the 2D plane at $(y,z)$, while $f(r,z)$ is the value of the 3D distribution at $(r,z)$. The inverse Abel transform is given by:

$$f(r,z) = -\frac{1}{\pi}\int_{r}^{\infty}\frac{dF(y,z)}{dy}\frac{1}{\sqrt{y^2-r^2}}dy\,. \tag{2.12}$$

In theory, the inverse Abel transform can be applied to measured 2D projection data to recover the original 3D volume. But experimental data is often discrete, such as intensity values captured on the pixels of a digital camera. Therefore, numerical evaluation of these integrals is required. This can generate unreliable results, both with noisy data due to the derivative in the equation, and for the case of $y = r$ where the denominator goes to zero causing the integrand to become infinite.

To overcome these issues, various numerical methods providing an approximate solution to the inverse Abel transform equation have been developed over the years. One of the first methods was proposed by Pretzler in 1991 [74], where the radial distribution at each depth $f(r,z)$ is expressed as a linear sum of cosine functions with unknown amplitudes. By minimising the least squares difference between the measured projection $F(y,z)$ and the projection generated from the sum of cosines, the original radial distribution can be recovered.

Since then, many numerical methods to provide solutions to the Abel transform have been developed [79–82]. Comparisons of the different methods for specific applications can be difficult however, as each of the Abel transform methods was developed independently, often using different mathematical conventions, different input data size and format conventions, and written in different computing languages. The different methods were also created with different goals in mind, such as favouring computational efficiency or robustness to noise. *PyAbel* [83,84] is a numerical package that combines several different Abel transform methods into a single Python (Python Software Foundation, https://www.python.org/) library. They are presented following the same mathematical conventions and using the same data formats, simplifying the comparison between the different Abel transform methods for different applications. The *PyAbel* package was used for the Abel transform section of this work.

The methods available in the *PyAbel* package include:

- *basex* – developed by Dribinski et al. [79]. The original distribution is expanded as a basis set of Gaussian like functions of variable number and width, with expansion coefficients determined through a least-squares fit. These functions have known analytical Abel transforms, so the transform is completed using simple linear algebra.
- *hansenlaw* – Hansen and Law's recursive method [80]. Makes a coordinate transformation to model the Abel transform as a set of linear-differential equations, iterating along each row of the image. All rows in the image can be processed simultaneously, creating a numerically efficient transform.
- *three_point* – the matrix-algebra method developed by Dasch [81]. Projection data is expanded as a quadratic function in the region surrounding each data point, then the derivative estimated using a three-point approximation. This enables the analytical integration of the inverse Abel integral around each radial point as a simple matrix algebra operation.
- *two-point* – a simplified version of the three-point method, also developed by Dasch [81]. Uses matrix algebra operations similar to the three-point method.
- *onion_peeling* – the third method of Dasch implemented in PyAbel. The onion-peeling method approximates the projection as rings of constant property for each radial point, then uses matrix algebra deconvolution [81].
- *onion_bordas* – back-projection method developed by Bordas et al [85]. For a given pixel in a row, calculates the contribution to the signal from that pixel. Signal is subtracted from the experimental projection pixel, and added to the back-projected image pixel. This is repeated from the outside to the image centre, for each row of pixels in the image.

- *direct* – attempts a direct integration of the Abel transform using simple numerical integration. Assumes only that the data has cylindrical symmetry [86].
- *daun* – modified onion-peeling deconvolution method of Daun. The original distribution is approximated with a step function or up to a third-degree polynomial, allowing the forward transform to be approximated by a system of linear equations in matrix form. Inverse transform is performed via onion-peeling with Tikhonov regularization applied [82].

The performance of the *PyAbel* package has been tested by Hickstein in 2019 [83], aside from the Daun method which was a later addition to the *PyAbel* package. Each method of the inverse Abel transform was used to numerically reconstruct a Gaussian function. The analytical Abel transform of a Gaussian function also results in a Gaussian function, allowing for an accurate analytical solution to equation 2.12. Comparing the numerical methods against the analytical solution for a one-dimensional Gaussian distribution gives an indication of the accuracy of that numerical method. While some discrepancy between the reconstructed and analytical results were found, the PyAbel methods were found to agree to within a root mean square error of 0.5% for all the methods except one [83].

The Abel transform was successfully used for radiation dosimetry applications by Ashraf & Rahman in 2021, looking at radioluminescence dosimetry of FLASH dose rate electron beams [87]. A water tank was doped with quinine sulfate solution, resulting in the production of optical photons when the water solution is irradiated. 2D projection images were captured by a camera, orthogonal to the radiation beam. The inverse Abel transform was used to reconstruct the 3D dose image from the 2D projection, with good agreement for measured depth dose characteristics and profile measurements. These results give confidence that the Abel transform can be useful in a dosimetric application.

The use of the inverse Abel transform is limited to radially symmetric beams, however. As many FLASH applications have radial symmetry [88,89] this will not limit the OC dosimeter for its most likely clinical application. But as many current clinical dosimetry methods are based upon the use of square fields [32,33], the ability to reconstruct a square field would be advantageous and increase the utility of the OC dosimeter. Therefore, different reconstruction methods will be required for these fields.

### 2.4.2 Filtered Back Projection

Filtered Back Projection (FBP) has been used for tomographic reconstruction applications such as computed tomography since the 1970s. It is based on the mathematical principles of the Radon transform [90,91], where given projection data acquired from various angles around an object as a linear sum through the object, the aim is to solve for structures internal to the object based on the summed projection values. For each projection, the measured projection values are evenly distributed across the image matrix, before being summed to compute the back-projected image. Simple back-projection results in a characteristic 1/r blurring when many projections are used, due to the radial geometry of the back-projecting leading to an increase in density of data points for small r values. Filtered back projection improves on this by applying a deconvolution kernel to each projection to compensate for the 1/r blurring [92]. The computational process can be sped up using properties of the Fourier transform, which is mathematically equivalent, but computationally faster.

A traditional FPB reconstruction, such the reconstruction of internal anatomy in an abdominal CT scan, utilizes hundreds of individual projections. This work does not benefit from the same approach due to the desire to keep the mechanical complexity minimised. Two orthogonal projections are the minimum number required to observe information on the full radiation beam, while keeping the increase to the mechanical complexity minimised. While a two-projection reconstruction would not be satisfactory to reconstruct a complex anatomical image, homogeneous dose distributions are much simpler compared to this, with only regions of dose or background and no dose gradients in between. As the reduced mechanical complexity from the two-projection approach is highly advantageous, the accuracy it is possible to achieve via this method will be investigated.

### 2.4.3 Fast Fourier Transform

Another potential tomographic reconstruction technique is through the use of Fourier reconstruction methods. The Fourier Transform (FT) is a mathematical operation that decomposes a spatially varying function into a series of functions dependent on the spatial frequency [93]. A Fourier reconstruction is based upon the principles of Fourier Slice Theorem, which states that the 1D FT of a projection through an object and a slice through the 2D FT of the same object are equivalent [94,95].

In practice, this means that for several projections taken through an object distribution at a series of angles, the 1D FT of the projections can be computed. These are then arranged in frequency space, centred upon the origin, at the same angle the projections were taken at. These projections are then interpolated from polar to Cartesian coordinates, before the 2D inverse FT is performed on the frequency domain image, reconstructing the original object distribution in the spatial domain. A Fourier-based reconstruction has been shown to be computationally faster than a FBP reconstruction, though traditional methods suffer from artefacts arising when interpolating the radially distributed projection data in frequency-space onto a Cartesian grid [94].

The Fast Fourier Transform (FFT) is simply a computationally efficient method of performing a FT [95]. A limitation of Fourier-based reconstruction techniques is in the interpolation step between the polar coordinates in frequency space and the Cartesian coordinates of the reconstructed image, leading to the formation of reconstruction artefacts [94]. A two-projection tomographic reconstruction using a FFT reconstruction potentially avoids this limitation, as two orthogonal projections align in both polar and Cartesian coordinates, so no interpolation step would be required. Therefore, the FFT reconstruction has the potential for accurate reconstruction of simple homogeneous fields, so presents another avenue to investigate for the two-projection reconstruction.

### 2.4.4 Advanced Reconstruction Methods

For this work the inverse Abel transform, filtered back projection, and the fast Fourier transform reconstruction algorithms have been selected to investigate, as these algorithms are well established and easy to implement into the tomographic reconstruction framework and characterise. But there also exist more advanced reconstruction methods that would also be suitable for the tomographic reconstruction of the OC dosimeter output.

Iterative reconstruction is a reconstruction algorithm that generates the reconstructed image over multiple iterative steps, rather than a single reconstruction step [96,97]. The same projection data are input into the algorithm, which generates an initial estimate of what the reconstructed image is. Forward projection data is then generated from this reconstruction estimate, and these projections are compared to the known projection data. The difference between the original and the estimate projection data is known as the error matrix. For the next iteration of the reconstruction, a slightly different image estimate is produced, the forward projections generated and compared, and a new error matrix computed. If the new error matrix is an improvement over the original the iteration is accepted, and the process is repeated. If not, that iteration is not accepted and a new iteration generated with a different alteration to the image estimate. This process is repeated until the error matrix is reduced to an acceptable level. This iterative process generates highly accurate reconstructions, but it is computationally expensive and harder to implement compared to a FBP or FFT approach [92].

Tomosynthesis is a reconstruction technique designed for limited angle tomography, developed for medical imaging with the motivation to reduce imaging doses [98–100]. Reconstruction can be based upon the inverse Radon transform or iterative algorithms, but additional approximation algorithms are used to compensate for the partial data sampling due to the low projection numbers. Tomosynthesis is based upon the retrospective reconstruction of arbitrary planes within the image. Projection images are shifted or added to bring structures of different planes into focus, allowing for the focussing of different planes at depth [101]. Much like iterative reconstruction however, tomosynthesis can be hard to implement and computationally expensive relative to FBP and FFT.

Iterative reconstruction and tomosynthesis have the potential for higher accuracy reconstructions from a lower number of projections compared to filtered back projection, making them both potential candidates for tomographic reconstruction of the OC dosimeter output. But implementing and fully characterising these more complex reconstruction algorithms was beyond the scope of this thesis, and these techniques remain an area of future work.

## 2.5 Concluding Remarks

Ultra-high dose rate radiation therapy techniques such as FLASH therapy offer the potential to increase the therapeutic window of radiation treatments. They are capable of delivering large doses with superior healthy tissue sparing relative to conventional treatments. Challenges in the dosimetry of these beams are a significant obstacle to overcome before these beams are widely implemented into clinical use, however. Optical calorimetry has the potential to overcome some of these difficulties, and if a tomographic reconstruction of the 2D output from the OC dosimeter could be performed with a high level of accuracy 3D dose distributions of these beams could be generated, significantly helping the dosimetric characterisation of these beams.

Due to the nature of the alignment of optical components within the dosimeter, there is a strong desire to reduce any additional mechanical complexity of the OC dosimeter as it is modified to perform the tomographic reconstruction. As such, Chapter 4 will investigate the reconstruction accuracy of a single-projection 3D reconstruction using the inverse Abel transform, which can be implemented with no modification to the current OC dosimeter design. The next smallest increase in mechanical complexity would be to take two orthogonal projections simultaneously, so Chapter 5 will investigate what is gained by this increase in complexity using a two-projection FBP or FFT reconstruction. Finally, the constraint of keeping the mechanical complexity low will be relaxed, and the reconstruction accuracy of a many-projection reconstruction will be investigated in chapter 6, to determine the maximum possible 3D reconstruction accuracy with the OC dosimeter output.

In the next chapter the simulation methods used to generate the range of beams used to characterise the performance of the subsequent tomographic reconstructions are detailed, as are the simulation methods used to model the integration of the projection data by the OC dosimeter. The methods and quantities used to determine the accuracy of the tomographic reconstructions, and compare the accuracy between the different methods are also detailed.

# Chapter 3: Simulation Methods

This chapter will detail the simulation methods used in this project, used to test the accuracy of performing a tomographic reconstruction accuracy on the two-dimensional output of the OC dosimeter. This includes the simulation of the radiation beam data that the OC dosimeter will be imaging, and the methods used to model the dose integration that occurs within the OC dosimeter detector system. This chapter will also cover the process used to analyse the reconstruction accuracy of the various tomographic reconstruction methods, and how this was quantified. These simulation methods and accuracy calculations are shared across all the various reconstruction approaches.

## 3.1 Radiation Beam Data Simulation

Two methods of simulating the generation of beam data for the investigation of the inverse Abel Transform in this chapter were used: one using MATLAB (The Mathworks, Natik, MA) to model a clinical 6MV photon beam from a linear accelerator, and one using TOPAS [102] to model a clinical 70MeV proton beam. Both methods were used to produce a 3D dose distribution within a 256x256x256 array. This size was chosen as a compromise between having enough pixels to maintain spatial resolution in the dose distribution, but without having too many pixels and being too computationally expensive to reconstruct. Both beams were created with the same orientation, with the radiation beam entering vertically downwards with the z-axis representing depth, and the x- and y-axes the lateral and longitudinal dimensions of the radiation beam respectively.

In MATLAB, a pseudo-circular region in the centre of a 256x256 array was created, with a nominal dose value of 1.0 to represent the deposition of dose from a radiation source, and the background region given a dose value of 0.0. This array represents an x-y plane of dose, sliced out of the radiation beam. These dose values were arbitrary for the purposes of this work, as it is the relative dose distribution that is of interest. The radiation beam size could be varied from a few pixels to the whole width of the array, though in practice beam sizes ranged from 32 pixels to 192 pixels in diameter, to represent a realistic proportion of the detector array the radiation beam would cover. The detector array on the current OC dosimeter is 1280x1024 with 6.7µm$^2$ pixels, corresponding to a maximum image size of 8.6cm x 6.7cm. Beam expansion and magnification or minification techniques could be used to image smaller and larger dose distributions if required, so the actual beam size modelled is also arbitrary for the purposes of this study. It is the pixel resolution of the output image, or the proportion of the image array the radiation beam occupies that is the real variable of interest. Because of the arbitrary nature of distance in this work, depth, distance, and position measures are mostly presented with units of pixels throughout this work.

A penumbral region was added to the edges of the circular region, modelled with a $tanh(x)$ function. This gave an approximation of the edge of a radiation beam, therefore creating a better approximation of the overall shape of a radiation beam. Figure 3.1 shows this modelled penumbra compared to the measured penumbra from a 10x10cm 6MV photon beam at 10cm deep, delivered using an Elekta Versa HD linear accelerator (Elekta Oncology Systems, Crawley, UK).

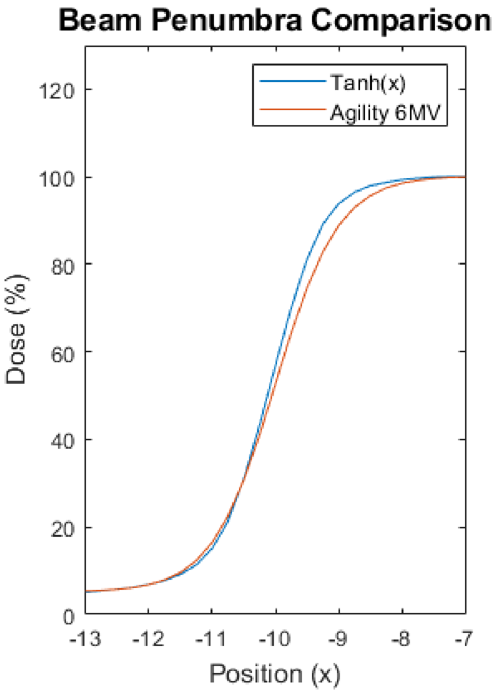

*Figure 3.1. Beam Penumbra comparison. The beam penumbra modelled in the MATLAB beam data simulations using a tanh(x) function and the beam penumbra from an Elekta Agility Versa HD 6MV photon beam are shown, for a 10x10 cm field at a depth of 10 cm.*

A uniformly distributed random noise component was added to the dose distribution, modelled as a percentage of the maximum dose value. This created a more accurate approximation of the inherent non-uniformity of a radiation beam. This 2D array was then repeated and stacked 256 times, to create a 256x256x256 3D array. This was then scaled in the z-dimension using 6X photon beam percentage depth dose (PDD) data from an Elekta Versa HD linear accelerator (Elekta Oncology Systems, Crawley, UK) to characterise the change in dose with depth of a radiation beam. Figure 3.2 shows the modelled photon 3D dose distribution alongside a CAX PDD and $D_{max}$ profile.

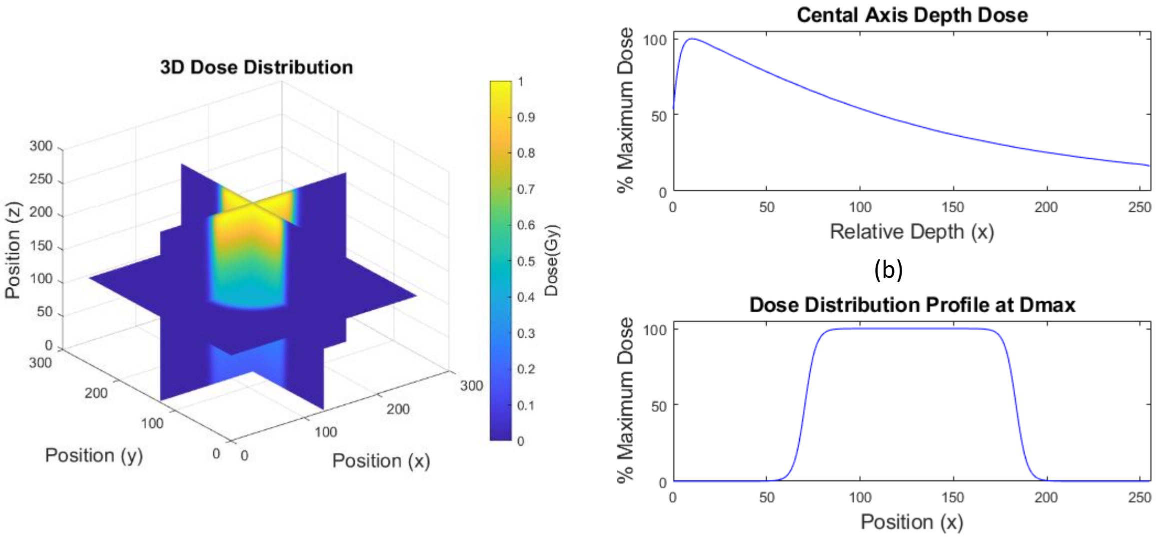

(b)

(a)

(c)

*Figure 3.2. MATLAB simulated 6X photon beam. 3D Dose Distribution (a), central axis PDD (b), and dose profile at the depth of maximum dose (c). The profile and PDD have been normalised to the maximum dose.*

This is a simplified model of a radiation beam and does not include features of a clinical beam such as beam divergence of the radiation beam with depth. But the advantages of this model are that it is very fast to compute, and easy to build in modifications to the model, such as varying the shape and size of the beam, the intensity of the beam, the level of noise modelled and the width of the penumbra. More complex clinical beam features such as a wedged intensity can also be included in the model with little additional computational time.

MATLAB was also used to simulate a simplified model of an Intensity Modulated Radiation Therapy (IMRT) beam. This model consisted of a modified square field, with the beam region split into a 3x3 checkerboard pattern when viewed from the x-y plane perspective. The checkerboard pattern consisted of different dose levels ranging from between 0.3 and 1.0. A Gaussian filter was then applied to the model, as a method of blurring the edges between the dose levels, approximating penumbra. While simple, the different dose levels and the presence of multiple dose gradients in both dimensions of the x-y plane represent some of the complex features of an IMRT radiation beam, and will test the various tomographic reconstruction algorithms ability to reconstruct these more complex fields. A slice through this dose distribution representing an x-y plane of dose is shown in Figure 3.3.

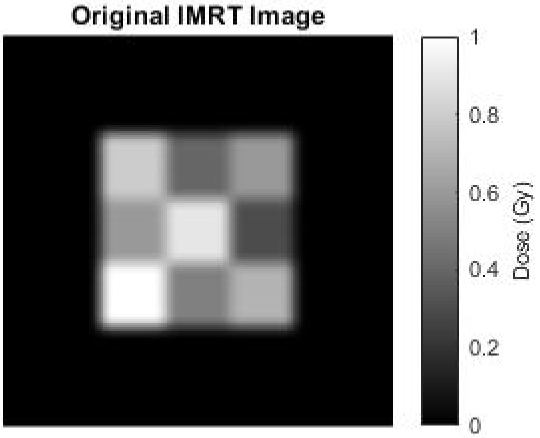

*Figure 3.3* Modelled IMRT radiation beam x-y slice. This beam consists of a 3x3 checkerboard pattern of varying dose levels, creating multiple dose gradients in both dimensions and presenting an increased level of complexity to reconstruct.

Three-dimensional dose distributions were also generated using TOPAS Monte Carlo (MC) software to simulate the dose deposition of a proton beam [102,103]. TOPAS is a Geant4 based particle simulation toolkit, that has been used for numerous radiation dosimetry applications [104–107]. A 70 MeV circular proton beam at an SSD of 4cm was used, with the beam size varying from 5mm to 40mm in steps of 5mm. Each simulation was run for 1 billion histories, resulting in a maximum standard error of the sum of less than 0.26% for all the modelled beams. This low uncertainty allows good confidence that the MC simulation models the dose deposition in a water phantom to an accuracy sufficient for this study. The TOPAS simulation output was scored on a 100x100x100 array, and then interpolated to a 256x256x256 array using a 3D linear interpolation function to reduce the computational time of the simulation and decrease the uncertainty in each individual pixel. Figure 3.4 shows the 3D dose distribution alongside a CAX PDD and $D_{max}$ profile for a TOPAS modelled proton beam.

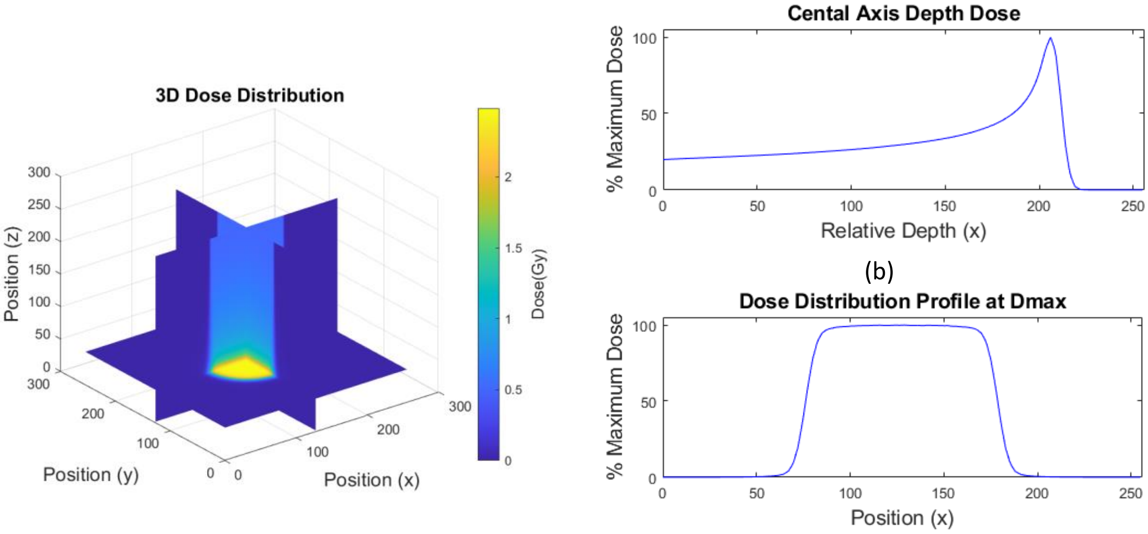

(a) (b) (c)

*Figure 3.4. TOPAS simulated 70keV proton beam. The 3D Dose Distribution (a), central axis PDD (b), and dose profile at the depth of maximum dose (c) are shown. The profile and PDD have been normalised to the maximum dose.*

The radiation beam data simulation methods differ slightly between the photon and the proton beams, with the MATLAB method for the photon beams being quicker but more simplified, while the TOPAS method for the proton beams was much slower, but more accurate [102,103]. This was deemed acceptable for the purposes of this study. The MATLAB approach allows for easy modification of several beam features, and the effect this has on the tomographic reconstruction quality characterized. For the proton beam, clinical modifiers such as passive beam scanning or dynamic spot scanning [108] are much more complex to model, and outside the scope of this initial investigation into the tomographic reconstruction of these beams. As FLASH proton beams are a potential clinical application of the OC dosimeter, a higher accuracy in this beam model was desired. As such, the MC simulation was chosen for its superior accuracy, and with only small number of different sized beams to model the long computational times were not detrimental to the timeframe of this study.

## 3.2 Detector System Simulation

The prototype OC dosimeter captures the integrated phase change across the water cell before and after irradiation, then this phase change is converted into dose. This differs slightly to the process used in this study, as the beam data is modelled as dose directly. However, these two variables can be directly related to one another via the change in refractive index due to the absorbed dose induced temperature increase [37,56]. This allows for the assumption that integrated phase is equivalent to integrated dose and for these variables to be used interchangeably.

Once the beam data has been produced, it needs to be integrated in one dimension to simulate the image acquired by the dosimeter. The integration was performed either by a manual sum in MATLAB or Python, or by using the virtual model of the OC dosimeter in FRED Optical Modelling software. The manual sum method is the theoretical best-case scenario, where no information has been lost to additional noise introduced by the dosimeter system. The virtual OC dosimeter model in FRED has had significant effort put in so that its output matches real-world measurements, including modelling the inherent noise characteristics. For the FRED integration method either a photon beam generated in MATLAB (Figure 3.5), or a proton beam generated in TOPAS (Figure 3.6) was loaded into FRED as a volume of water containing the 3D dose distribution.

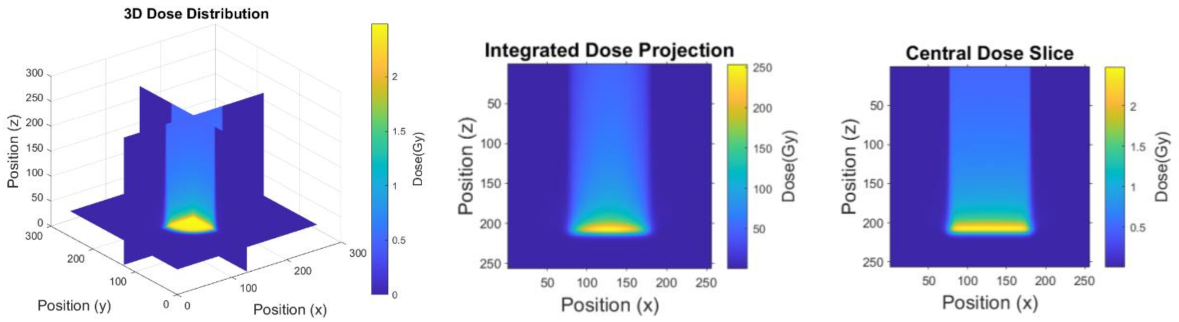

(a) (b) (c)

*Figure 3.5. TOPAS modelled 20mm proton beam distribution. The 3D dose distribution is shown in (a), and the resulting 2D central slice (b) and 2D integrated dose projection (c). The slice is generated by taking the central 2D z-x plane from the 3D distribution, while the projection is generated by summing the entire 3D distribution in the y-dimension. The difference between the two images is highlighted in the dose values, with the slice having a maximum of around 2 Gy while the projection has a maximum of closer to 250 Gy. Due to the cylindrical symmetry of the dose distribution the intensity varies across the x-axis in the projection also, while it is much more consistent in the slice image.*

The dose distribution in FRED was modelled as a relative refractive index change between pixels. As FRED has been independently verified that the absolute refractive index change gives the absolute temperature change, and therefore the absolute dose change [37,56,57], the relative refractive index change rather than the absolute change could be modelled to speed up the simulation process. This relative refractive index change was then scaled appropriately to give the equivalent amount of dose of interest. The geometry of this integration was kept constant in both methods, for both sets of data. The radiation beam is assumed vertically downwards, in the z-dimension. The object beam of the prototype dosimeter is orthogonal to this, and here is defined as being the +y direction. So, for each integration method the 3D image was integrated in the y-dimension, producing a 2D x-z array representing the integrated dose image that is the final output of the OC dosimeter.

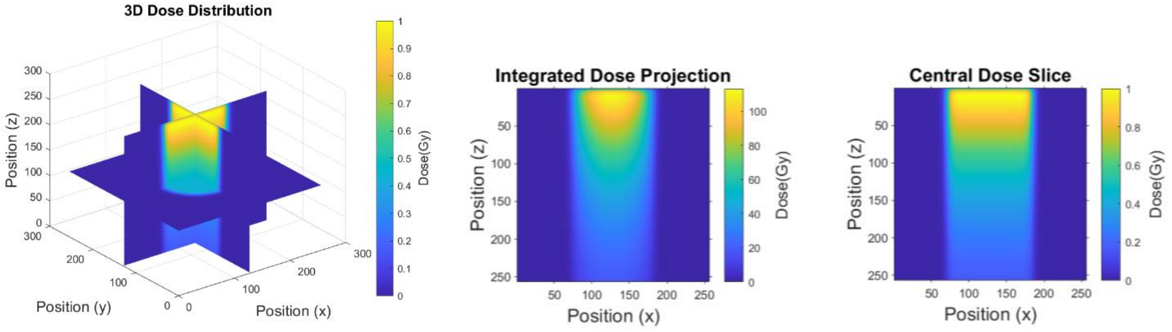

(a) (b) (c)

*Figure 3.6. MATLAB modelled 160-pixel photon beam distribution. The 3D dose distribution is shown in (a), and the resulting 2D central slice (b) and 2D integrated dose projection (c). The slice is generated by taking the central 2D z-x plane from the 3D distribution, while the projection is generated by summing the entire 3D distribution in the y-dimension. The difference between the two images is highlighted in the dose values, with the slice having a maximum of 1 Gy while the projection has a maximum of closer to 110 Gy. Due to the cylindrical symmetry of the dose distribution the intensity varies across the x-axis in the projection also, while it is much more consistent in the slice image.*

## 3.3 Quantifying Reconstruction Accuracy

An important step is determining what constitutes an acceptable reconstruction of a 3D dose distribution, and how the reconstructed 3D distribution compares to the original 3D distribution. This involves quantifying the difference between the two dose distributions and determining whether this are within an acceptable limit. For this study, the Root Mean Square Error (RMSE) and maximum error were chosen to quantify the accuracy. The RMSE is between the true value $x$ and the estimated value $\hat{x}$ is given by the equation:

$$RMSE = \sqrt{\frac{\sum_{n=1}^{N}(x - \hat{x})^2}{N}}. \tag{3.1}$$

The RMSE is a useful tool for determining the error for noisy data, where the mean value of a comparison would average out to zero, giving a potentially falsely accurate result. The maximum error simply describes the maximum difference between the reconstructed distribution and the original, presented as a percentage of the maximum dose value in the distribution. For this dosimetric technique to be clinically relevant, it needs to be able to determine dose to an uncertainty level that is equal to or better than current dosimetric methods described in Section 2.1.

The exact method of determining the RMSE is slightly different between the different reconstruction techniques, depending on the orientation of the reconstruction algorithm output. The details for each method are described in detail in the following sections.

### 3.3.1 1D Gaussian Reconstruction

This is the simplest case, with only a single one-dimensional (1D) array for both the original and reconstructed distributions. The RMSE between the two distributions is calculated directly.

### 3.3.2 Inverse Abel Transform Reconstruction

The output of the inverse Abel Transform is a 2D image, representing a vertical slice through the centre of the original 3D distribution. In the coordinate system of this study, this is a z-x image, where the z-axis represents the axis of radial symmetry in the radiation beam, and the x-axis being lateral through the beam. Rotational interpolation of the 2D slice can then generate the full 3D distribution. This interpolation step becomes time-consuming when computing a number of reconstructions, and is unnecessary as a 2D slice through the centre of a radially symmetric object contains the same amount of information as the full 3D distribution. Therefore, the reconstructed 2D image was compared to the central slice of the original 3D distribution to determine the reconstruction accuracy.

When comparing the reconstructed image to the 2D central slice of the original distribution, profiles are taken along both the z- and x- dimensions to quantify the reconstruction. This is shown in Figure 3.7. Firstly, along the z-axis at the centre of the radiation beam, then secondly along the x-axis at the depth of dose maximum. This allows the profiles to represent central axis PDDs and lateral profiles at the depth of dose maximum ($D_{max}$) respectively, two dosimetric quantities that can be used to characterise a clinical radiation beam [109].

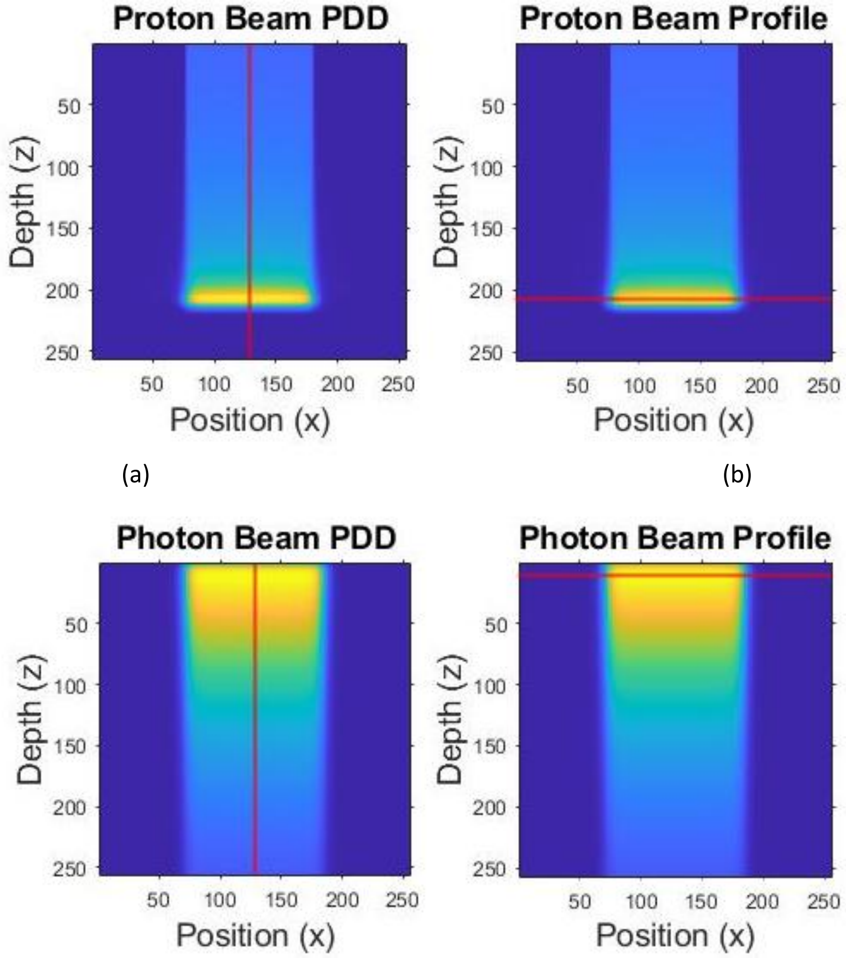

(a) (b)

(c) (d)

*Figure 3.7. PDD and $D_{max}$ Profile measurement locations. 2D central slice images are taken from the centre of the 3D dose distribution, for the TOPAS simulated 20mm proton beam and the MATLAB modelled 160-pixel photon beam. Marked in red are the location of the profiles used to characterise the dosimetric accuracy on the reconstruction, with the CAX PDD on the left (a,c), and the $D_{max}$ profile on the right (b,d).*

In addition, to provide an indication of the reconstruction accuracy for the clinical dosimetrically relevant parts of a radiation beam, the RMSE for the central 21 pixels and central 81 pixels for the profiles were also calculated. The central 21 pixels represent the central axis of a radiation beam and is the part of the reconstruction where high accuracy is the most desired, as the majority of clinical dosimetric quantities are defined on the central axis [32,33]. The central 81 pixels were chosen as they represent the region of the distribution containing the pixels with significant amounts of dose deposited within them. The actual proportion of the distribution within the beam region will vary as the overall size of the beam is varied, but the value of 81 pixels was chosen as a compromise between the largest and smallest field sizes investigated in this study, to keep the analysis consistent. These regions within a profile are the same for both photon and proton beams, and are shown in Figure 3.8.

For proton radiation, the dose deposited is inversely proportional to the square of their velocity [110]. The initial dose deposition is low, with the rate of dose deposition slowly increasing as they interact with a medium, before the majority of their energy is deposited as they come to a complete stop. This results in the proton PDD having an extended, low dose build-up region followed by a large peak at a specific depth, before rapidly falling off past this point. This peak is known as the Bragg Peak, the depth of which is energy dependent. The location of the Bragg Peak is an important quantity in proton dosimetry [111], so high reconstruction accuracy in this region is desired. For the PDDs of proton beams the RMSE was also calculated for the Bragg Peak region, defined here as a 21-pixel region centred on the depth of dose maximum, as this is the region of the PDD containing the Bragg Peak. This is shown in Figure 3.9 below.

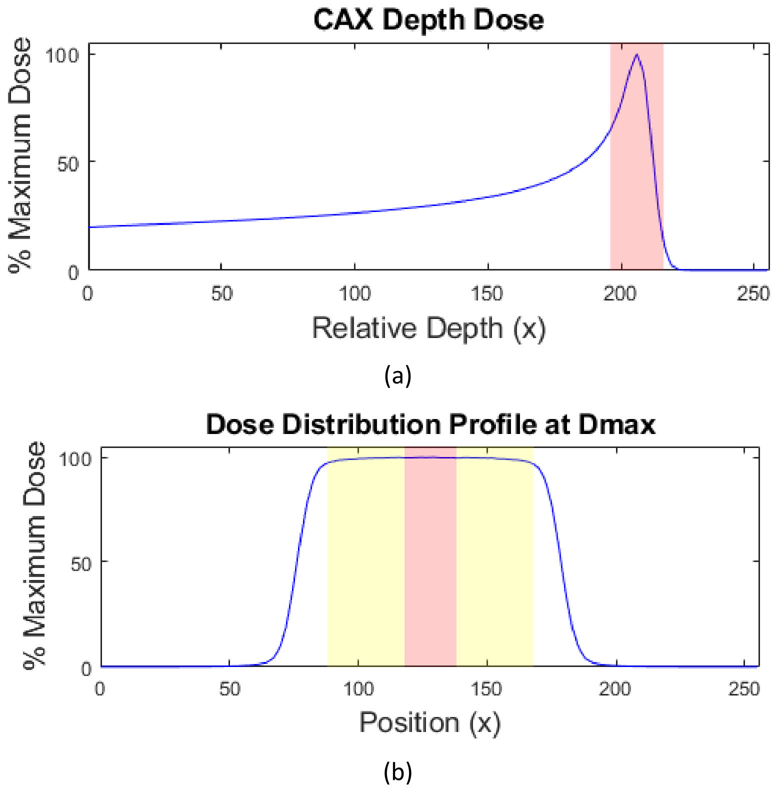

(a)

(b)

*Figure 3.8. Dosimetrically relevant area of accuracy analysis. Shown is a TOPAS 20mm proton beam PDD and profile, with the PDD (a) showing the Bragg Peak region highlighted in red. In the profile (b) the central axis region is highlighted in red, while the beam region is highlighted in yellow.*

### 3.3.3 Filtered Back Projection & Fast Fourier Transform Reconstructions

The output of the FBP and FFT algorithms is a 2D array, representing a horizontal slice through the 3D distribution at some depth. In the coordinate system of this work this represents a x-y image, with the x-axis and y-axis being lateral and longitudinal through a radiation beam, where depth is the z-axis. The original 3D distribution can be reconstructed by performing the reconstruction at each depth z, then stacking the slices upon each other to form the full dose volume.

Profiles were used to quantify the reconstruction quality of these methods. The definitions for the CAX and beam regions and their associated RMSE from Section 3.3.2 apply. As the reconstructed image is an x-y plane of dose at a single depth, the profile is taken through the centre of the radiation beam along the x-axis. For the analysis of FBP and FFT reconstructed fields, often only a single slice at the depth of dose maximum was reconstructed. As the dose distributions for these reconstructions were created by creating multiple x-y slices, then scaling the slice with a PDD and stacking them upon each other to form the 3D distribution, the reconstructions other depths are simply scaled copies of this slice. The analysis of all the slices provides no additional information compared to the $D_{max}$ slice, with the same relative errors occurring on each slice. To save time in the analysis process, only the single $D_{max}$ slice was reconstructed and analysed. For the same reason, PDD analysis was not performed on these dose distributions, as all the information on the reconstruction quality is contained in a single x-y slice for these beams.

# Chapter 4: Single Projection Reconstruction

This chapter investigates the limitations on reconstruction accuracy for a single projection system. A single projection reconstruction is highly desirable as it would require no modification to the current prototype optical calorimeter dosimeter. The likely application of the OC dosimeter lies in FLASH dosimetry, which are often produced circularly with radial symmetry [22,112]. This makes the investigation of the single-projection reconstruction of these beams using the inverse Abel transform a priority for this work. The findings of this chapter will therefore be indicative of what level of 3D dose reconstruction accuracy is possible to achieve with the current OC dosimeter.

The focus of this chapter will be on using the inverse Abel transform to reconstruct the 3D dose distribution, using the *PyAbel* software package in Python [84]. This provides access to a number of different methods to perform the inverse Abel transform, so finding the best performing method for our purposes was investigated initially. As the Abel transform is only relevant for use on radially symmetric objects, circular photon beams were modelled in MATLAB and Monte Carlo simulated proton beams were generated using TOPAS. The reconstruction accuracy of these beams was initially investigated using a manual sum to model the integration due to the dosimeter, before then being compared to the reconstruction resulting from using FRED to integrate the beam, better representing the real-world performance of the dosimeter.

Finally, the limits of the inverse Abel transform were tested by attempting to reconstruct non-radially symmetric beams such as a square beam. This would confirm that the single projection approach using the inverse Abel transform is only applicable to radiation fields that are radially symmetric, and no information about any asymmetries in the beam is sought.

## 4.1 *PyAbel* Functionality Tests

The inverse Abel transform uses a 2D projection taken through a radially symmetric object and reconstructs the central 2D slice of that object. As the 3D object distribution is radially symmetric, this reconstructed 2D central slice contains all the information of the 3D array, and a full 3D array can be obtained via interpolation.

Here, the inverse Abel transform is used to reconstruct the original dose distribution from the modelled integrated dose image of the OC dosimeter. This was implemented using the *PyAbel* package in Python. This package contains eight transformation methods, each a different approximation of the Abel transform solution for a cylindrically symmetric object. To determine the best method for the reconstruction of OC dose images, the performance of the individual methods was tested initially on a Gaussian distribution to check the accuracy of the *PyAbel* package was as expected. Next, the methods were tested on more clinically relevant models of a proton beam and a photon beam. The best performing method could then be characterized fully to estimate the maximum reconstruction accuracy possible using the inverse Abel transform reconstruction method.

### 4.1.1 Gaussian Distribution Reconstruction

Initially, methods investigating the performance of the *PyAbel* package presented in Hickstein et. al 2019 [83] were repeated, to check the implementation of the *PyAbel* package. Results that were not comparable to their findings would indicate an error in the procedure. A 1D non-symmetric Gaussian distribution, 70 pixels in length was generated, with the first pixel corresponding to the centre of the radially symmetric distribution. The Abel transform of a Gaussian distribution is itself a Gaussian distribution, allowing for an easy comparison between the analytical result and the reconstructed distribution for the case of a 1D Gaussian [83]. Hickstein et. al found that none of the methods provide a perfect solution, so a slight discrepancy in the reconstructed distribution is expected, with this error becoming more pronounced at points close to the centre of radial symmetry. A comparison of the reconstructed distribution to the analytical distribution for each method will determine the size of this discrepancy and indicate the best performing methods available.

The first step was to repeat the investigation using the exact distributions as used by Hickstein et. al. Both the Gaussian distribution and the integrated projection data corresponding to the Gaussian were generated using the *abel.tools.analytical.GaussianAnalytical* module of *PyAbel* [84]. The projection data were reconstructed using each inverse Abel transform method, then the reconstructed distribution compared to the original distribution, as shown in Figure 4.1 for the direct method.

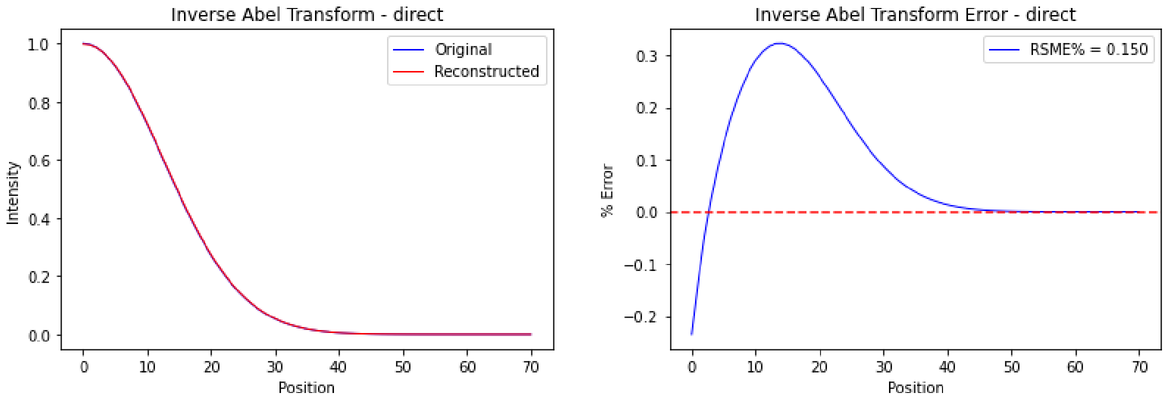

(a) (b)

*Figure 4.1. Inverse Abel transform asymmetric Gaussian reconstruction. The inverse Abel transform (direct method) reconstructed Gaussian distribution and original distribution are shown in (a). The Gaussian distribution is asymmetric and 70 pixels in length, following the methodology of Hickstein et. al 2019. The percentage error (b) between the original and reconstructed distribution, highlighting the maximum discrepancy occurring closer to the axis of radial symmetry.*

To compare to the results of Hickstein et. al [83] the RMSE between the two distributions was calculated as a percentage of the maximum value. The maximum percentage error for the reconstruction was recorded also. These were calculated for each of the seven reconstruction methods, as shown in Table 4.1.

*Table 4.1. Inverse Abel transform asymmetric Gaussian reconstruction accuracy. The MRSE was calculated for inverse Abel transform reconstructed non-symmetric Gaussian distributions of length 70, for the entire distribution, beam region and central axis region, and the maximum error for the different inverse Abel transform methods in PyAbel.*

| METHOD | HICKSTEIN RMSE (%) | RMSE (%) | MAX ERROR (%) |
|---|---|---|---|
| **DIRECT** | 0.15 | 0.15 | 0.32 |
| **BASEX** | 0.04 | 0.04 | 0.07 |
| **HANSEN-LAW** | 0.23 | 0.33 | 1.64 |
| **TWO POINT** | 0.32 | 0.32 | 1.76 |
| **THREE POINT** | 0.06 | 0.06 | 0.17 |
| **ONION PEELING** | 0.07 | 0.07 | 0.32 |
| **ONION BORDAS** | 12.03 | 0.80 | 4.06 |

The calculated results match very well to the expected results, showing the implementation of the Abel transform was correct. A slightly larger RMSE for the Hansen-Law method than what was expected was found, as was greatly reduced reconstruction error for the Onion Bordas method. This can likely be attributed to different versions of the *PyAbel* code being used in the Hickstein et al. 2019 paper, compared to the most current 0.8.5 version used here. But as the performance of the Hansen-Law method is only 0.1% worse, while the other methods perform exactly as expected or better, this allows the use of the *PyAbel* package confident it is working as intended.

To test the transform methods using a slightly more representative sample of the data to be investigated in this study, the reconstruction of a fully symmetric 1D Gaussian distribution of length 255 was also investigated. This better approximates the resolution of the radiation beam distributions, and a symmetric Gaussian better approximates the profile of a radiation beam. An odd number of pixels was chosen so the centre of the distribution was located on a single pixel, to avoid any pixel averaging or asymmetry effects. An example of the reconstructed distributions is shown in Figure 4.2 for the Basex inverse Abel transform method.

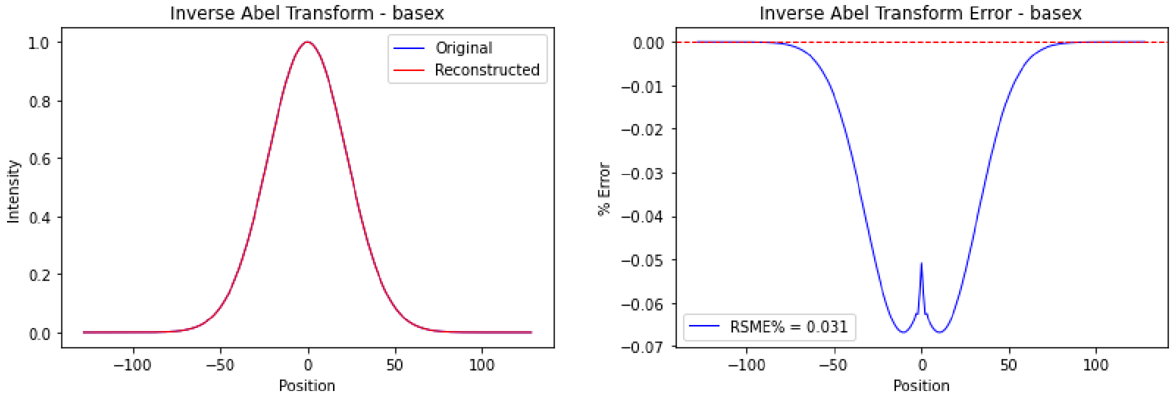

(a) (b)

*Figure 4.2. Inverse Abel transform reconstruction of a symmetric Gaussian. The inverse Abel transform (Basex method) reconstructed Gaussian distribution and original distribution are shown in (a). The Gaussian distribution is symmetric and 255 pixels in length, representative of the radiation beams modelled in this study. The percentage error (b) between the original and reconstructed distribution, highlighting the maximum discrepancy occurring close to the centre of the distribution.*

As for the asymmetric Gaussian, the RMSE and maximum error are calculated for each reconstruction. In addition, to provide an indication on the reconstruction accuracy for dosimetrically relevant parts of a radiation beam, the RMSE for the CAX and beam regions, as defined in Section 3.3.2, were also calculated. This was done for the entire range of transform methods in *PyAbel*, including the additional Daun method which was added to the PyAbel package since the publication of the 2019 paper. Results are shown in Table 4.2.

*Table 4.2. Inverse Abel transform symmetric Gaussian reconstruction accuracy. The RMSE is calculated for the inverse Abel transform reconstructed symmetric Gaussian distributions of length 255, for the entire distribution, beam region and central axis region, and the maximum error for different inverse Abel transform methods.*

| METHOD | RMSE (%) | BEAM RMSE (%) | CAX RMSE (%) | MAX ERROR (%) |
|---|---|---|---|---|
| **DIRECT** | 0.12 | 0.21 | 0.14 | 0.27 |
| **BASEX** | 0.03 | 0.06 | 0.06 | 0.07 |
| **HANSEN-LAW** | 0.14 | 0.24 | 0.43 | 0.88 |
| **TWO POINT** | 0.15 | 0.26 | 0.50 | 1.00 |
| **THREE POINT** | 0.02 | 0.03 | 0.05 | 0.05 |
| **ONION PEELING** | 0.03 | 0.04 | 0.08 | 0.13 |
| **ONION BORDAS** | 0.41 | 0.73 | 1.41 | 2.71 |
| **DAUN (D=3)** | 1.54E-06 | 9.75E-07 | 1.50E-06 | 1.55E-05 |

These results show that all the transform methods produce an accurate reconstruction of the Gaussian distribution, with the RMSE being less than 0.5% in all cases. The greatest accuracy was found with the BASEX, Three Point, Onion Peeling and Daun methods, while the least accurate result came from the Onion Bordas method. These results for these methods show increased accuracy compared to what was seen in Hickstein et al. This is expected, as one of their findings was the reconstruction accuracy improved as the number of pixels in the distribution increased. Therefore a 255-pixel distribution should be easier to reconstruct than a 70-pixel distribution, as is shown in the results here. This provides further confidence that the inverse Abel Transform is working as expected.

Of the Abel Transform methods the Daun method appears superior, with a reconstruction error several order of magnitudes smaller than the other methods. The next best was the BASEX, Three Point and Onion Peeling methods, all producing a RMSE of less than 0.05%, and a maximum error of less than 0.15%. While these methods are strong candidates for use reconstructing the prototype OC dosimeter output, it is important to also consider that a simple 1D Gaussian distribution is shaped differently and contains none of the noise characteristics of a radiation beam. While the Gaussian tests confirm the inverse Abel Transform methods perform accurately and as expected, these methods need to be tested on a more realistic radiation beam dose profile to truly determine the best method for the purposes of this study.

### 4.1.2 Proton Beam Reconstruction

The next step was to repeat the Gaussian distribution investigation using a TOPAS proton beam distribution, allowing the comparison of the inverse Abel Transform methods on representative radiation beam data. Projection data were generated via integrating the 3D distribution in one dimension, as described in Section 3.2. The inverse Abel transform was then performed on this 2D projection data for each of the different methods. A 20mm proton beam was chosen as the test beam for this investigation, as it is in the middle of the size range of simulated beams. Examples of this reconstruction for several methods are shown in Figure 4.10, with the Basex, Hansen-Law and three-point methods showing good profile matching at $D_{max}$, with only a slight discrepancy on the CAX present.

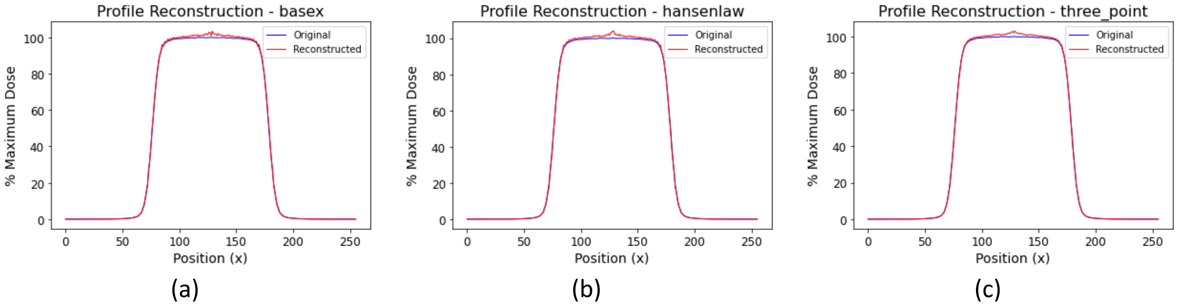

*Figure 4.3. Inverse Abel transform TOPAS modelled proton beam reconstruction accuracy. Using manually summed projection data, the inverse Abel transform reconstructed proton beam $D_{max}$ profiles are compared to the original $D_{max}$ profile for the Basex (a), Hansen-Law (b) and three-point (c) methods of PyAbel.*

Reconstruction accuracy was quantified by comparing $D_{max}$ profiles and PDDs for the original and reconstructed distributions, with the RMSE and maximum error being calculated for each. For the profiles the RMSE is calculated for the entire distribution, the beam region and the CAX region, as shown in the Table 4.3. These results for the profile reconstruction all show a RMSE of less than 1%, a beam RMSE of less than 1.5%, a central axis RMSE of less than 2.5%, and a maximum error of less than 4%. Of the eight methods tested, the Onion Bordas method appears superior, with a RMSE of 0.5%, beam RMSE of 0.8%, central axis RMSE of 0.9%, and a maximum error of 1.4%. Of particular importance to this study is that the central axis reconstruction error is less than 1% for the Onion Bordas method, half the size or less compared to the other methods.

*Table 4.3. Inverse Abel transform proton beam profile reconstruction accuracy. Using manually summed projection data, the RMSE was calculated for the inverse Abel transform reconstruction of a 20mm TOPAS proton beam profile for the entire distribution and the beam and central axis regions. The maximum reconstruction error was calculated also. This was repeated for all the inverse Abel transform methods in PyAbel.*

| METHOD | RMSE (%) | BEAM RMSE (%) | CAX RMSE (%) | MAX ERROR (%) |
|---|---|---|---|---|
| **DIRECT** | 0.79 | 1.33 | 1.90 | 2.80 |
| **BASEX** | 0.72 | 1.19 | 1.81 | 3.26 |
| **HANSEN-LAW** | 0.78 | 1.32 | 2.01 | 3.82 |
| **TWO POINT** | 0.81 | 1.37 | 2.06 | 3.80 |
| **THREE POINT** | 0.69 | 1.20 | 1.83 | 2.90 |
| **ONION PEELING** | 0.75 | 1.25 | 1.88 | 3.52 |
| **ONION BORDAS** | 0.51 | 0.80 | 0.89 | 1.43 |
| **DAUN (D=3)** | 0.73 | 1.22 | 1.84 | 3.23 |

Figure 4.4a shows a comparison of the original and reconstructed profiles at $D_{max}$, for the Onion Bordas inverse Abel transform method. Figure 4.4b shows the percentage error between the two profiles as a function of lateral position.

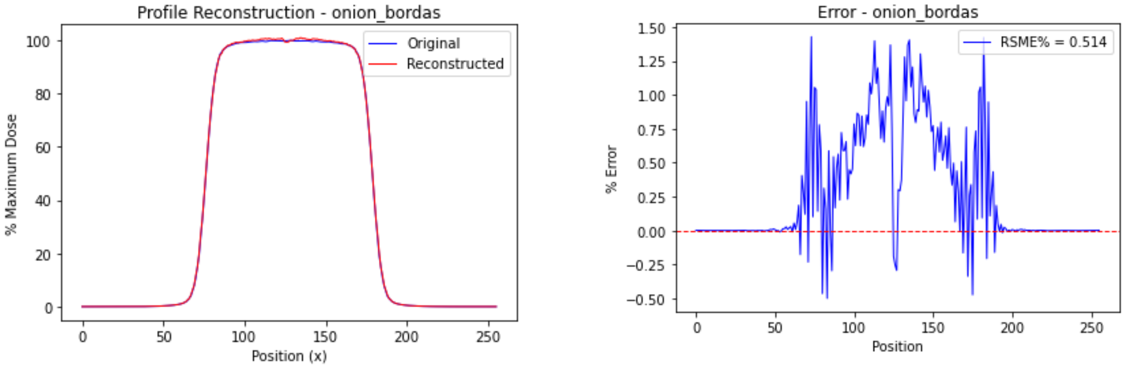

(a) (b)

*Figure 4.4. Onion Bordas inverse Abel transform profile reconstruction accuracy. The inverse Abel transform reconstructed proton beam $D_{max}$ profile is compared to the original $D_{max}$ profile for the Onion Bordas reconstruction method (a). The percentage error between the original and reconstructed profiles is shown in (b).*

For the PDD's the RMSE was calculated for the entire distribution and the Bragg Peak region. However, it became apparent that the level of noise in the reconstructed profiles could cause misleading results for these PDDs. When taking the PDD down a single central column of pixels, very different results could be obtained when using the 127th, 128th or 129th pixel, for example, due to the high frequency oscillations of the reconstruction between these pixels. To remove this potential error the PDDs were calculated as the mean of the central five profiles, averaging out any outlying results when the PDD was located within a high or low part of the reconstruction noise. The mean PDD results are shown in Table 4.4 for each of the inverse Abel transform method.

*Table 4.4. Inverse Abel transform proton beam PDD reconstruction accuracy. The RMSE is calculated for the inverse Abel Transform reconstruction of a 20mm TOPAS proton beam PDD, for the entire distribution and the Bragg Peak region, averaged over the central five PDDs, and the maximum error of the reconstruction for the different inverse Abel transform methods in PyAbel.*

| METHOD | RMSE% | BRAGG PEAK RMSE (%) | MAX ERROR (%) |
|---|---|---|---|
| **DIRECT** | 0.91 | 1.95 | 2.80 |
| **BASEX** | 0.83 | 1.77 | 3.26 |
| **HANSEN-LAW** | 1.09 | 2.33 | 3.82 |
| **TWO POINT** | 0.99 | 2.12 | 3.80 |
| **THREE POINT** | 0.88 | 1.88 | 2.90 |
| **ONION PEELING** | 0.86 | 1.85 | 3.52 |
| **ONION BORDAS** | 0.05 | 0.28 | 0.15 |
| **DAUN (D=3)** | 0.86 | 1.83 | 3.23 |

These results show a similar trend to the profile results. All methods produced a RMSE of less than 1%, except for the Hansen-Law method at 1.1%. The Bragg Peak RSME was less than 2.5% and the maximum error was less then 4% for all methods. Again, the Onion Bordas method performs the best of all the tested methods, with a RMSE of 0.05%, a Bragg Peak RMSE of 0.3%, and a maximum error of 0.15%. This can be seen in Figure 4.5, showing the plot of the original and reconstructed central axis PDDs and the percentage error between the two.

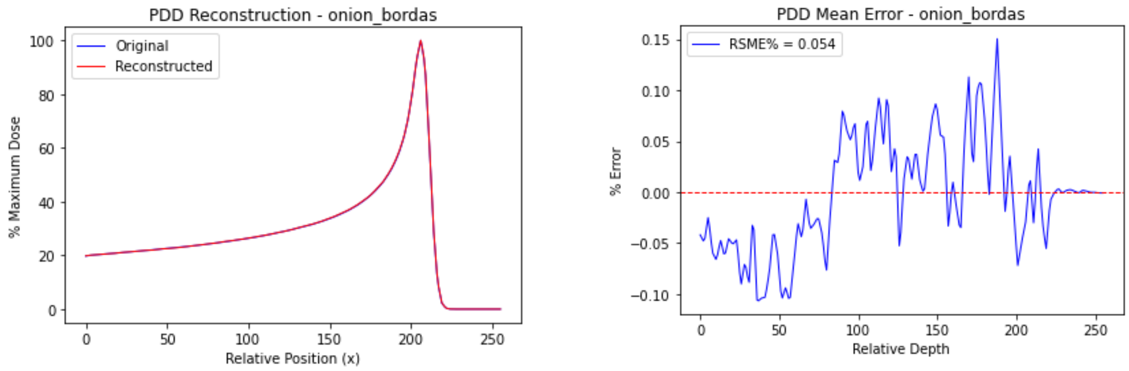

(a) (b)

*Figure 4.5. Onion Bordas inverse Abel transform PDD reconstruction accuracy. The inverse Abel transform reconstructed proton beam PDD is compared to the original distribution PDD for the Onion Bordas reconstruction method in (a). The percentage error between the original and reconstructed PDDs is shown in (b).*

The results from the proton beam reconstruction were quite different to the results from the Gaussian distribution reconstruction, which is worth noting. Based off the Gaussian results, the Daun method should have provided superior results, with the BASEX, Three Point and Onion Peeling methods being the next best. Instead, the Onion Bordas method was the best performing of the transform methods, and the rest all performed on a similar level. This is the opposite to what was found for the Gaussian reconstruction, where the Onion Bordas was the worst performing method. However, it is stated in the *PyAbel* documentation that different methods may perform better than others depending on the type and level of noise found in the image to be reconstructed [83]. This would suggest that for the noise characteristics found in the modelled proton beam dose distributions, integrated using the manual sum method, the Onion Bordas method is the best suited for reconstruction.

From these initial results it was concluded that of the eight transform methods in the *PyAbel* package tested, the Onion Bordas reconstruction method appears the most appropriate for reconstructing the proton beams modelled in this study.

### 4.1.3 Photon Beam Reconstruction

The final step of the *PyAbel* functionality tests was to test the reconstruction methods on a radially symmetric photon beam, allowing another comparison of the methods on another model of radiation beam data. This followed the same process as used for the proton beam reconstruction in section 4.1.2. Projection data was generated by integrating the 3D distribution in one dimension, then the inverse Abel transform was performed on this using each of the individual methods. The reconstructed 2D image was then compared to the central 2D slice of the original 3D distribution, using profiles at $D_{max}$ and PDDs to quantify the reconstruction accuracy.

A photon beam of 128 pixels in width, generated as described in Section 3.1, was chosen for this initial test as it is the middle of the size range of the modelled photon beams. This beam was simulated with noise and penumbra added to make the model more representative of a clinical radiation beam.

As described in Section 3.3, the RMSE for the entire profile, beam region and CAX region, along with the maximum error were used to quantify the accuracy of the profile reconstruction. For the PDDs, the RMSE for the entire PDD and the maximum error were used. As a photon PDD does not have a Bragg Peak, and the distribution varies slowly with depth relative to a proton PDD, extra RMSE regions were not used for the analysis of the PDD reconstruction accuracy. The reconstruction accuracy metrics are shown in Table 4.5 below.

*Table 4.5. Inverse Abel transform photon beam profile reconstruction accuracy. Using manually summed projection data, the RMSE was calculated for the inverse Abel transform reconstruction of a MATLAB modelled 192-pixel width photon beam profile for the entire distribution and the beam and central axis regions. The maximum reconstruction error was calculated also. This was repeated for all the inverse Abel transform methods in PyAbel.*

| METHOD | RMSE (%) | BEAM RMSE (%) | CAX RMSE (%) | MAX ERROR (%) |
|---|---|---|---|---|
| **DIRECT** | 3.72 | 6.29 | 12.0 | 30.9 |
| **BASEX** | 11.7 | 20.7 | 40.3 | 183 |
| **HANSEN-LAW** | 2.37 | 3.92 | 5.93 | 10.1 |
| **TWO POINT** | 7.82 | 13.8 | 26.6 | 119 |
| **THREE POINT** | 6.49 | 11.4 | 22.1 | 96.8 |
| **ONION PEELING** | 12.2 | 21.6 | 42.2 | 191 |
| **ONION BORDAS** | 2.88 | 4.74 | 8.55 | 14.6 |
| **DAUN (D=3)** | 10.2 | 18.1 | 35.2 | 158 |

It is immediately apparent from Table 4.5 that the reconstructions for the modelled photon beams are not of the same quality as the proton beams, with errors of 40% for the CAX RMSE, 20% for the beam RMSE, and 12% for the entire distribution RMSE. A maximum error of 190% was found for the Onion Peeling method. The best performing method was the Hansen-Law method, with a RMSE of 2.4%, beam RMSE of 3.9%, CAX RMSE of 6%, and a maximum error of 10%. Interestingly, this is the opposite of what was found in the Gaussian and proton beam reconstructions, where the Hansen-Law method was among the worst performing. This highlights the variability between the methods for different datasets with different noise characteristics, and the importance of testing the methods for each type of distribution. The cause of the large reconstruction errors can be easily seen in the $D_{max}$ profiles, shown in Figure 4.6 for the three-point and Hansen-Law methods as examples. All the transform methods have large, oscillatory artefacts on the central axis. For most methods this results in a large spike right on the central pixel, as show above for the three-point method. The Hansen-Law and Onion Bordas methods perform better relative to the other methods as this large central spike is not present, as shown for the Hansen-Law above. But this still results in maximum construction errors of greater than 10%, and CAX errors of greater than 5%. The presence of this artefact on the central axis is highly undesirable for the purposes of this study, as this is the region where the reconstruction accuracy is most critical.

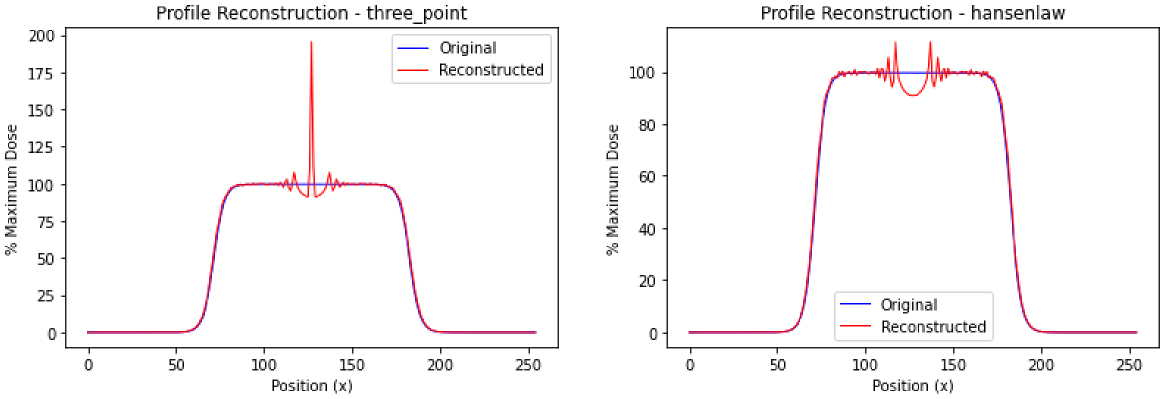

(a) (b)

*Figure 4.6. Inverse Abel transform photon beam profile reconstruction accuracy. The inverse Abel transform reconstructed proton beam profile is compared to the original distribution PDD for the three-point reconstruction method in (a), and the Hansen-Law method in (b). Both figures highlight the large reconstruction artefact found on the central axis, with the three-point method demonstrating a large spike, while the Hansel-Law method demonstrates a large trough.*

These CAX artefacts result in large errors for the PDDs also, as this artefact is largest in the pixels where the PDD is taken. Averaging the central five columns to generate the PDD improves the result slightly, but as shown in Table 4.6, the PDD reconstruction errors in the photon beam reconstructions remain large for all methods.

*Table 4.6. Inverse Abel transform photon beam PDD reconstruction accuracy. The RMSE is calculated for the inverse Abel Transform reconstruction of a MATLAB modelled 192-pixel width photon beam PDD, for the entire distribution and the Bragg Peak region, averaged over the central five PDDs, and the maximum error of the reconstruction for the different inverse Abel transform methods in PyAbel.*

| METHOD | RMSE% | MAX ERROR (%) |
|---|---|---|
| **DIRECT** | 7.52 | 13.5 |
| **BASEX** | 20.5 | 36.8 |
| **HANSEN-LAW** | 4.26 | 7.65 |
| **TWO POINT** | 9.98 | 17.9 |
| **THREE POINT** | 12.1 | 21.7 |
| **ONION PEELING** | 18.1 | 32.4 |
| **ONION BORDAS** | 7.3 | 13.1 |
| **DAUN (D=3)** | 18.2 | 32.9 |

As observed in the profile analysis none of the reconstructed PDD curves compare well with the original, for any of the reconstruction methods. The Hansen-Law and Onion Bordas methods were the best performing, but still resulted in an RMSE of at least 4%, and a maximum error of at least 7.5%. The BASEX method was the worst performing, with a RMSE of 20%, and a maximum error of 37%.

These results show that for the reconstruction of MATLAB simulated photon beams, integrated using the manual sum method, of the available transform methods in PyAbel the best performing was the Hansen-Law method. Despite the reconstruction showing very accurate matching of profiles in the penumbra region, the presence of large artefacts in the CAX region resulted in the Hansen-Law method having a RMSE of 2.4% for the entire profile or 6% for the CAX, and a PDD RMSE of 4%.

### 4.1.4 Concluding Remarks

The initial functionality testing showed that for a single projection reconstruction using the inverse Abel transform, using manually summed projection data, the reconstruction of the TOPAS generated proton beams using the Onion Bordas method resulted in a very accurate reconstruction, while the reconstruction accuracy of MATLAB generated photon beams was reduced by the presence of artefacts on the central axis. As the proton beams were the more accurate beam model, and the reconstruction of FLASH proton beams is a likely application of the OC dosimeter, it was decided to focus on the characterisation and determining the level of accuracy achievable with this method. The photon beam reconstruction could potentially be just as accurate if the prominent CAX artefact could be removed, but solving that particular problem fell outside of the timeframe of this study, so remains an area of potential future work.

## 4.2 Proton Beam Reconstruction Characterisation

From the initial PyAbel functionality testing, it was determined that the Onion Bordas inverse Abel Transform method was the most accurate for the purpose of reconstructing the proton beams in this study. The next step was to optimise and fully characterise this reconstruction on a series of different sized proton beams and determine how robust the reconstruction is. Optimising the reconstruction will look at the effects of pre- and post- reconstruction filtering, to reduce the noise and produce the best quality reconstruction without compromising the spatial integrity. Any effect of beam size on reconstruction accuracy has implications for the prototype 3D OC dosimeter design. If the proportion of the image occupied by the radiation beam affects the reconstruction accuracy, then this would indicate on the maximum and minimum sized radiation beam the dosimeter can measure as it is currently designed, indicate a requirement to investigate into minification or magnification techniques if this beam size range is not desirable, or determine size requirements for the detector array.

### 4.2.1 Filtering

Due to the stochastic nature of a radiation beam, there will always be small fluctuations in the dose throughout a Monte Carlo modelled 3D dose distribution. This can be clearly seen in Figure 4.7 for a zoomed in $D_{max}$ profile of a 20mm TOPAS simulated proton beam, and the reconstructed profile. These fluctuations appear detrimental to the performance of the inverse Abel Transform reconstruction, so pre-reconstruction filtering of the dose distribution to smooth these fluctuations out could be beneficial for the reconstruction accuracy. The reconstructed image also contains a noise component, that could be reduced with post-reconstruction filtering.

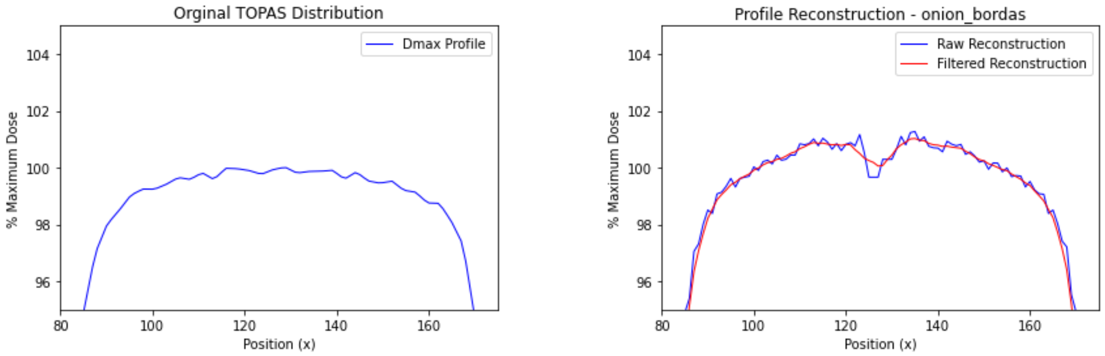

(a) (b)

*Figure 4.7. Filtering of TOPAS proton beam profiles. Zoomed in images of 20mm TOPAS proton beam $D_{max}$ profiles, highlighting the variation within the distribution. (a) Original $D_{max}$ profile. (b) raw and filtered Onion Bordas inverse Abel transform reconstructed profiles, with a 7-point rolling average filter applied to reduce the noise in the reconstructed image.*

The impact of pre- and post-reconstruction filtering was investigated, using a 20mm TOPAS simulated proton beam, and the Onion Bordas inverse Abel Transform method. The RMSE, CAX RMSE and maximum error was calculated for the reconstructed distribution $D_{max}$ profile, with different types and level of filtering applied. Both a uniform filter and a Gaussian filter were investigated. The uniform filter replaces the pixel value with the mean value of a range of neighbouring pixels, with the number of pixels being averaged specified [113]. The Gaussian filter is similar but weighs the pixels in the centre of the specified range more heavily, with the standard deviation of the Gaussian filter being specified [114]. These two filtering options were chosen for their smoothing ability, ease of implementation within the Python environment and high computational speed. Uniform filter widths of 3, 5, 7 and 9 were tested, while standard deviations of 0.5, 1.0, 1.5 and 2.0 were investigated for the Gaussian filter. Figure 4.8 shows how the filtering effected the reconstruction accuracy.

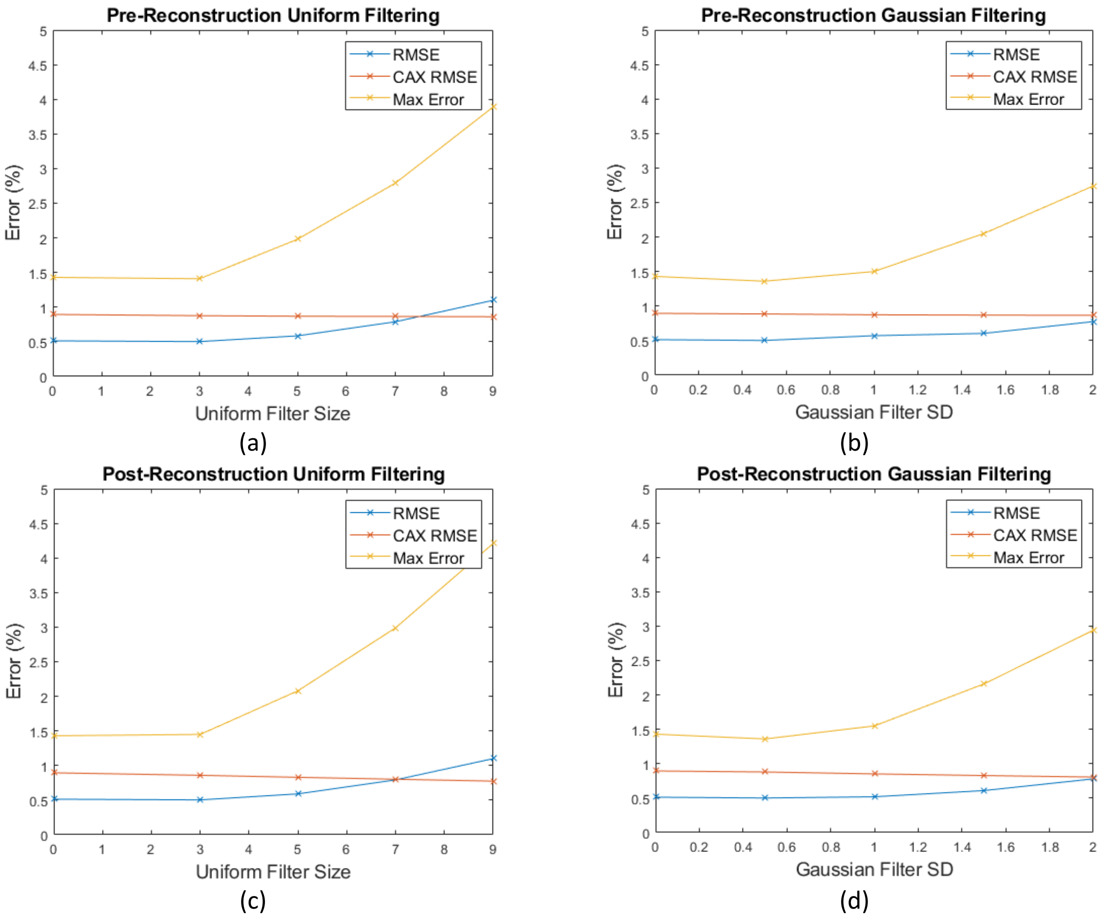

*Figure 4.8. Reconstruction error with different levels of filtering. An Onion Bordas inverse Abel transform reconstruction of a 20mm TOPAS proton beam was used, with different filter specifications for (a) pre-reconstruction uniform filtering, (b) pre-reconstruction Gaussian filtering, (c) post reconstruction uniform filtering and (d) post reconstruction Gaussian filtering.*

The pre-reconstruction filter was applied to the projection data before the inverse Abel Transform was performed on it, while the post-reconstruction filter was applied to the dose distribution after the inverse Abel Transform reconstruction had been performed. A one-dimensional filter was used for each filter type, with the filter being applied in the lateral dimension for each row of pixels. This prevented any loss of spatial resolution in the z-dimension, crucial for maintaining accuracy when determining the Bragg Peak. The additional filtration did not significantly improve the reconstruction quality, however. While the error in the central axis region increases slightly with the increased filtration, this is offset by a large increase in error in the total distribution and the maximum error. The reason for this is apparent when comparing an error plot for reconstruction $D_{max}$ profiles for a filtered versus a non-filtered reconstruction, as shown in Figure 4.9.

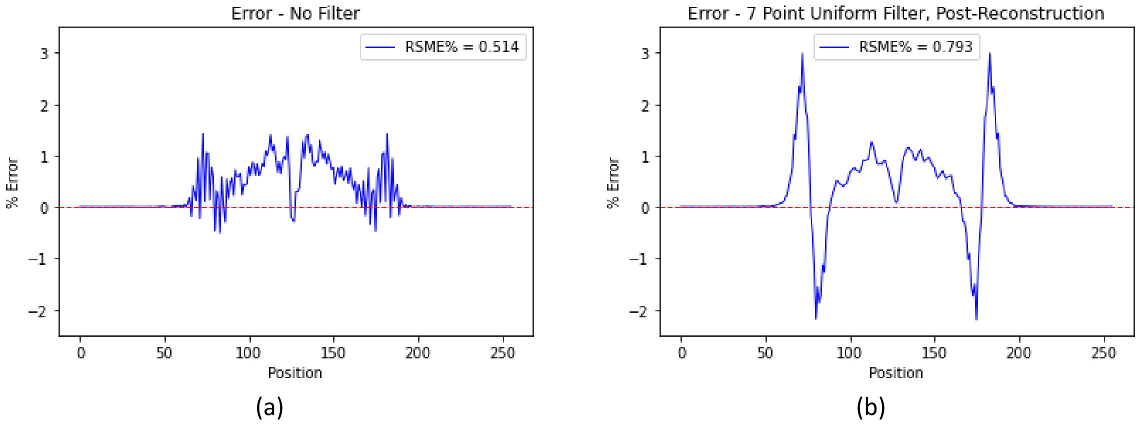

*Figure 4.9. Effects of filtration on reconstruction error. Plots show the reconstruction error for an Onion Bordas inverse Abel transform reconstruction of a 20mm TOPAS proton beam, for an unfiltered beam (a) and the reconstruction with a 7-point uniform filter applied (b).*

Clearly, while the filtering slightly improves the noise characteristics in the central axis region, it also increases the error at the edge of the beam. This is due to the filter smoothing out the sharp definition of the beam edge, as the lower intensity penumbra region gets averaged out with the high intensity beam region. This is not a desirable result, so filtering of the entire distribution is not beneficial to the reconstruction quality. It would be possible to filter only the central region of the beam, reducing the noise in this region while avoiding any beam edge blurring effects. But as the improvement to the CAX RMSE is only very slight with this filtering applied, the benefits of filtering the manually integrated TOPAS images do not seem worthwhile at this time.

### 4.2.2 Beam Size

To investigate the effects of the beam size on reconstruction accuracy TOPAS simulated proton beams were used, of sizes ranging from 5mm to 40mm in 5mm increments. The manual sum method was used to generate the projection data, as described in Section 3.2, then the inverse Abel Transform is used on this projection data to reconstruct the original distribution. Following the findings of Section 4.1.2, only the Onion Bordas method was used. For each of the 8 beam sizes the reconstructed 2D image is compared to the central 2D slice of the original distribution. The RMSE, beam RMSE, CAX RMSE and maximum error for profiles at the depth of dose maximum, and the RMSE, Bragg Peak RMSE and maximum error for PDDs are calculated to quantify the reconstruction accuracy. For the PDDs the average over the centre 5 pixels is taken, to reduce the impact an outlying high or low reconstruction point has on this calculation. The measures of error in the profile and PDD comparisons are shown in Figure 4.10 below, as the error is plotted as a function of the beam size.

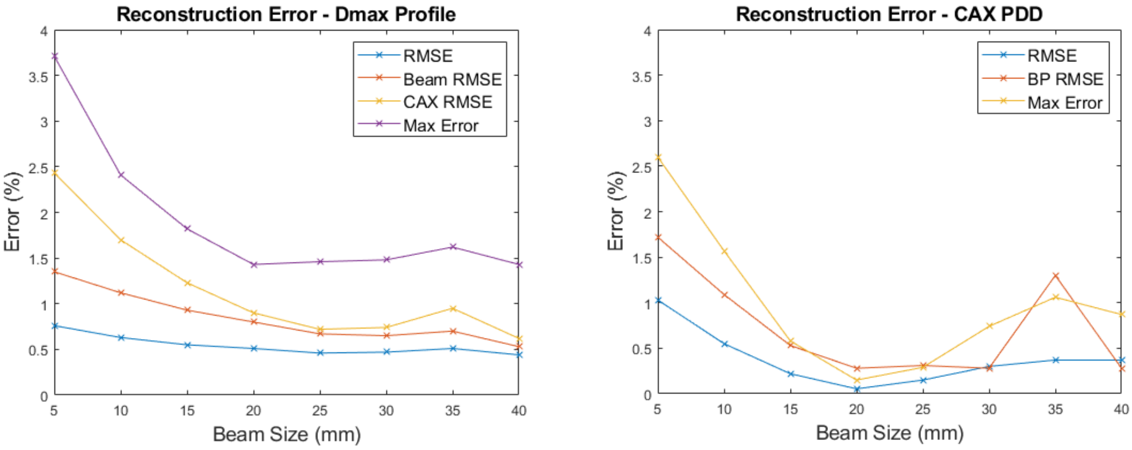

(a)

(b)

*Figure 4.10. Reconstruction error as a function of beam size. $D_{max}$ profiles (a) and PDDs (b) were compared, for TOPAS modelled proton beams ranging from 5mm to 40mm in size, for the Onion Bordas inverse Abel transform reconstruction method.*

These results show a general increase in reconstruction accuracy as the beam size is increased. For the profiles all measures of error decrease as the beam size increases from 5mm to 20mm, then remain relatively consistent between 20mm and 40mm in size, except for a small increase in the measured errors for the 35mm beam. For the PDDs the error also decreases as the beam size increases from 5mm to 20mm, but the error then increases again with beam size, particularly for the calculated max error. The BP RMSE has a large spike for the 35mm reconstruction, but this remains consistent for all beam sizes greater than the 20mm beam.

The source of the increased error for the smaller beam sizes can be seen in the $D_{max}$ profile comparisons, shown in Figure 4.11 for the 5mm and 15mm beams. Particularly for the 5mm beam, the reconstruction overestimates the dose at the central axis, peaking at around 3.5% larger than the original dose. A check of the other transform methods confirmed the Onion Bordas method is still the best performing for these smaller beams, with the other transform methods all resulting in maximum errors of around 10%. This error is much less pronounced in the 15mm beam reconstruction, with the CAX RMSE and maximum error falling to half the size than for the 5mm beam.

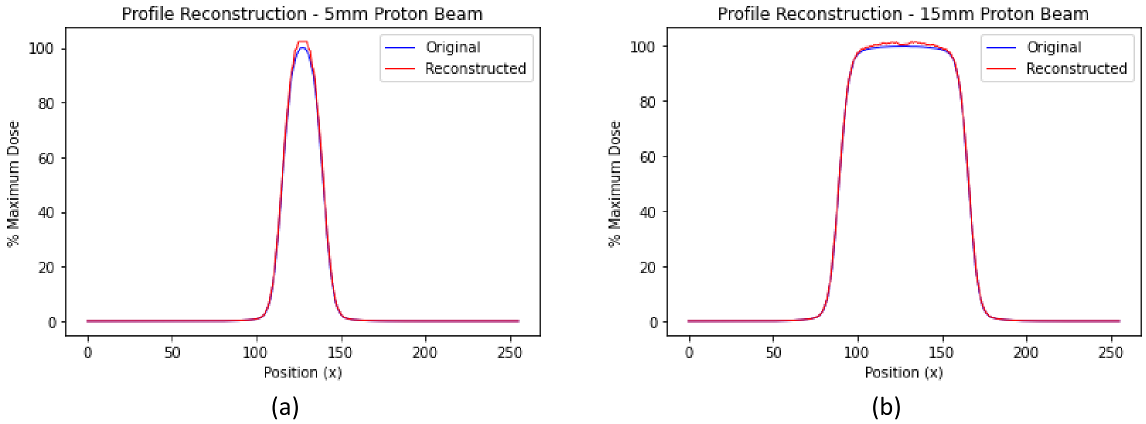

(a) (b)

*Figure 4.11. Narrow beam inverse Abel transform reconstruction. Comparisons of $D_{max}$ profiles for original and inverse Abel Transform reconstructed dose distributions, for a 5mm (a) and 25mm (b) TOPAS proton beam.*

The larger beams in general all perform better than the smaller beams, with the exception of the maximum error increasing slightly and a large jump in the Bragg Peak RMSE for the 35mm beam. Closer examination of the $D_{max}$ profile comparisons indicates the cause of this as a trough in the reconstructed profile, located on the central pixels where the PDD is calculated. The exact cause of this reconstruction artefact was not determined, but this can be seen in Figure 4.12, showing the 35 mm proton beam original and reconstructed profiles, alongside the percentage error between the two profiles as a function of the beam position.

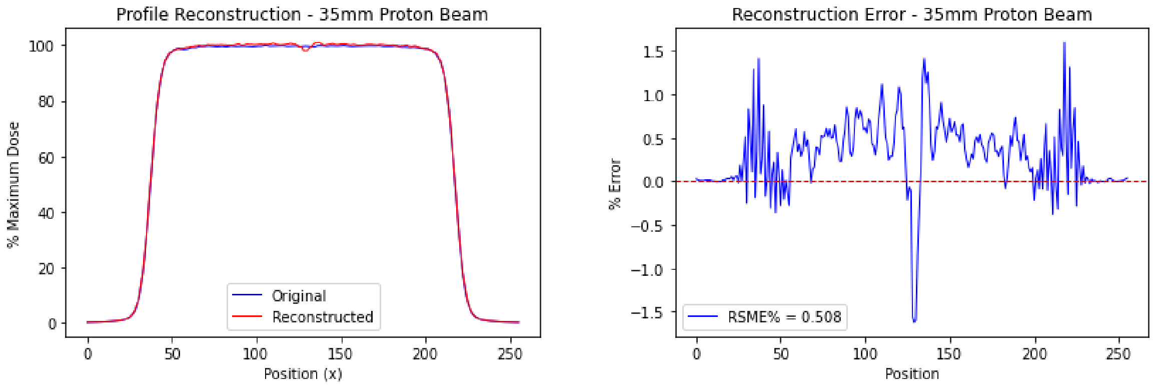

(a) (b)

*Figure 4.12. TOPAS 35mm proton beam inverse Abel transform reconstruction. Comparisons of the $D_{max}$ profile for the original and inverse Abel Transform reconstructed dose distribution (a), and the calculated percentage error between the distributions (b), for a 35mm TOPAS proton beam.*

### 4.2.3 Proton Beam Characterisation Conclusions

This section investigated factors effecting the accuracy of the Onion Bordas inverse Abel transform, performed on TOPAS simulated proton beam data using the manual sum integration method. Filtering of the data did not result in any accuracy improvements, for both pre-reconstruction and post-reconstruction filtering. The filtering resulted in increased errors due to the blurring of the beam edge before it reduced the error in the central axis region. The size of the radiation beam was found to affect the reconstruction accuracy, with the 5mm and 10mm beams showing an increased reconstruction error relative to the beams 15mm and larger, for which the reconstruction error remained relatively constant.

## 4.3 FRED Projection Reconstruction

From the investigation into single projection reconstruction using the inverse Abel Transform, the results from this study indicate the Onion Bordas method performs the best with the TOPAS generated proton beam data. This reconstruction has been found to perform better for beam sizes 15mm and above. So far, these reconstructions have been performed by manually summing the 3D dose distribution data along the line of observation of the detector to simulate the projection data the OC dosimeter would produce. Due to the simplistic nature of this model, it fails to capture any of the additional noise characteristics that are added by the detector system, so does not represent a true simulation of the OC dosimeter prototype.

To make the integration of the projection data more realistic, the virtual model of the prototype OC dosimeter within FRED optical modelling software was used. Different 3D dose distributions were imported into the FRED model, and the dosimeter output for each beam was simulated. As described in Section 2.2.4 this provides a more accurate representation of the real-life output of the prototype OC dosimeter. The difference between the two methods can be clearly seen by comparing the dose projection images of each. The FRED projection contains a significant increase in noise relative to the manual sum, which can be seen in both the projection images and the $D_{max}$ profile comparison for a 30mm proton beam model in Figure 4.13.

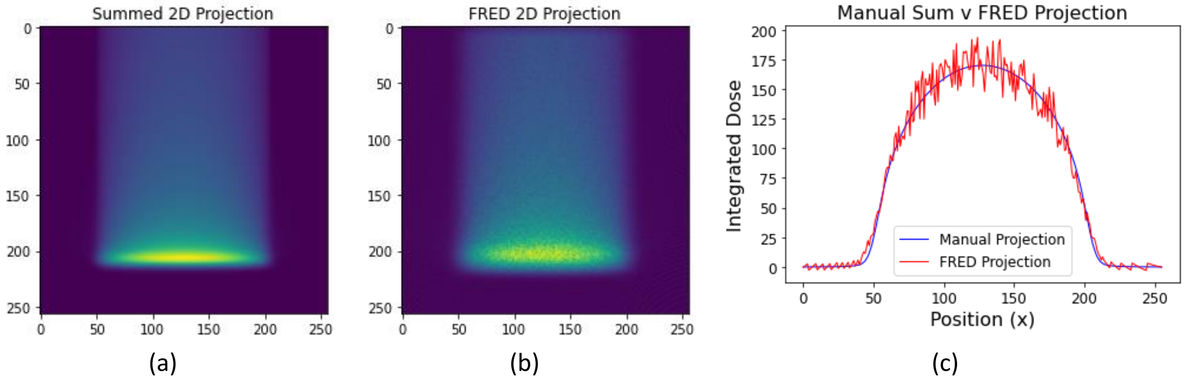

*Figure 4.13. Comparison of integrated projection images of a 30mm TOPAS proton beam. Integration was performed by a manual sum (a), or via the dosimeter model in FRED optical modelling software (b). Comparison of profiles taken through $D_{max}$ for each projection (c).*

A limitation in the virtual OC dosimeter model became apparent, as the integration performed by FRED appeared to saturate at a maximum dose value. This is shown in Figure 4.14. This effect was apparent in the smaller beams, where the dose was concentrated over fewer pixels resulting in a greater dose per pixel. For the beams 25mm and smaller, the FRED projections did not follow the expected curved shape obtained when integrating a cylindrical object, rather appearing cropped in the central region of the beam. Unfortunately, the cause for this could not be determined, and it was beyond the scope of this project to investigate why this model was breaking down for these smaller beams. As such, the FRED reconstructions focused on the 30mm, 35mm and 40mm beam sizes. As found in section 4.2.2 these larger beams were more accurate to reconstruct than the smaller ones, so limiting the study to the larger beams will not compromise the quality of the reconstruction.

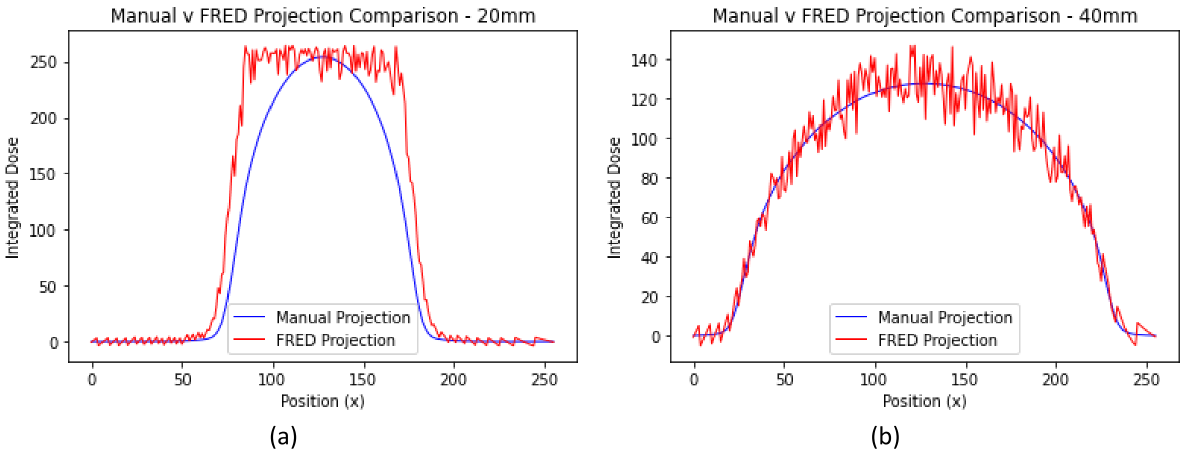

*Figure 4.14. Effects of beam size on the FRED integrated projection data. Comparison of manually integrated and FRED integrated projections, for a 20mm (a) and 40mm (b) TOPAS proton beam. The cropping of the top of the FRED projection is evident in the 20mm projections, while the 40mm beam follows the shape of the manual projection, albeit noisily.*

The noise in the raw FRED projections was too large to achieve a sensible reconstruction with the inverse Abel Transform, with the resulting image showing little resemblance to the original dose distribution. It is evident pre-reconstruction filtering the FRED projection would be required to generate a usable reconstruction. An example of the effects of filtering on this projection can be seen in Figure 4.15, for Gaussian filters of sigma = 3, 6 and 9, compared to the non-filtered projection in Figure 4.14 above. The agreement between the manually summed projection data and the FRED generated projection data improves as more filtering is applied, with the sigma = 9 filtering showing a much better agreement in the centre of the projection compared to the sigma = 3 filter. The compromise for this filtering comes at the expense of the edge of the projection, with the sigma = 9 projection showing poor agreement at the edge of the projection data. The filtering spreads out the edge of the projection, creating a filtered projection that is wider than the original. To investigate the impact filtering had on the inverse Abel transform reconstruction of FRED projection data, the methods of section 4.2.1 were repeated with varying levels of uniform and Gaussian filtering applied to the projected image prior to reconstruction.

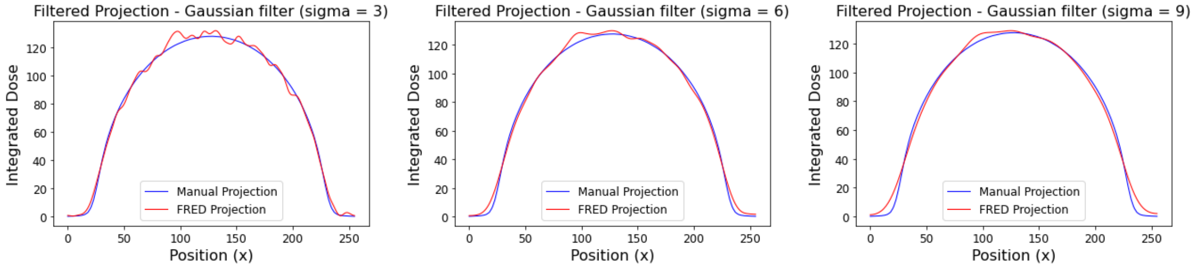

(a) (b) (c)

*Figure 4.15. The effects of filtering on the FRED generated projection data. The FRED projection from the 30mm TOPAS modelled proton beam was filtered with a Gaussian filter of sigma = 3 (a), 6 (b) and 9 (c).*

The 30mm beam was chosen to investigate, as the results of 4.2.2 found this to be the most accurate of the 3 largest beams to reconstruct. Figure 4.16 shows for various levels of uniform filter and Gaussian filter the corresponding RMSE, CAX RMSE and maximum error for the $D_{max}$ profile comparisons, and the RMSE, Bragg Peak RMSE and maximum error for the PDD comparisons.

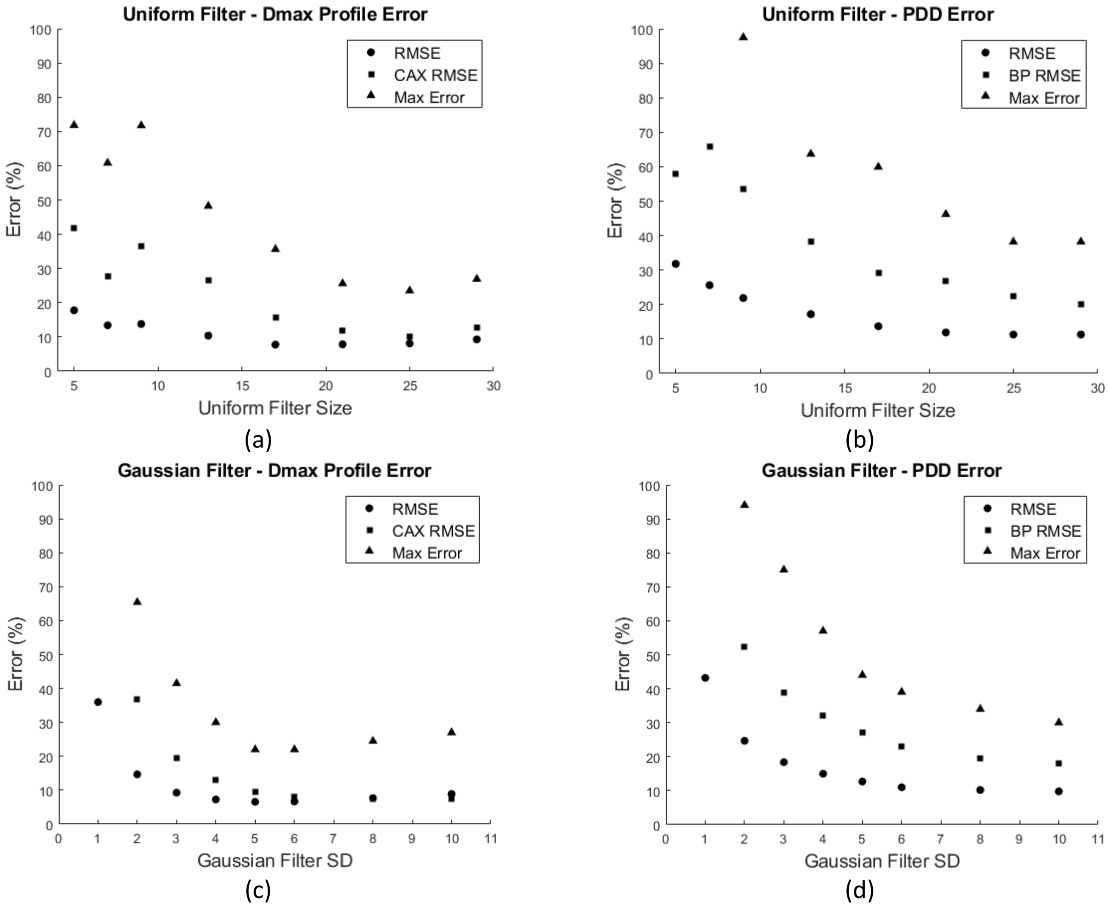

*Figure 4.16. Reconstruction error for levels of filtering of FRED projection data. Filtering was applied prior to reconstruction, using: (a) Uniform filter $D_{max}$ profile error. (b) Uniform filter PDD error. (c) Gaussian filter $D_{max}$ profile error. (d) Gaussian filter PDD error.*

These results show that a high level of filtering is required to achieve improvements in reconstruction accuracy, much greater than what was attempted in section 4.2.1. The best profile reconstruction performance occurs for the Gaussian filter with a sigma of 5 or 6. But even with this filtering, the reconstruction error remains around 8-10%, above the level of accuracy that would be deemed acceptable for dosimetric purposes. The noise in the FRED projection was too great to be filtered out to improve the central axis accuracy without excessive blurring of the beam edge and the increased error associated with this, as shown in the profile comparisons for reconstructions with different levels of Gaussian filtering applied in Figure 4.17.

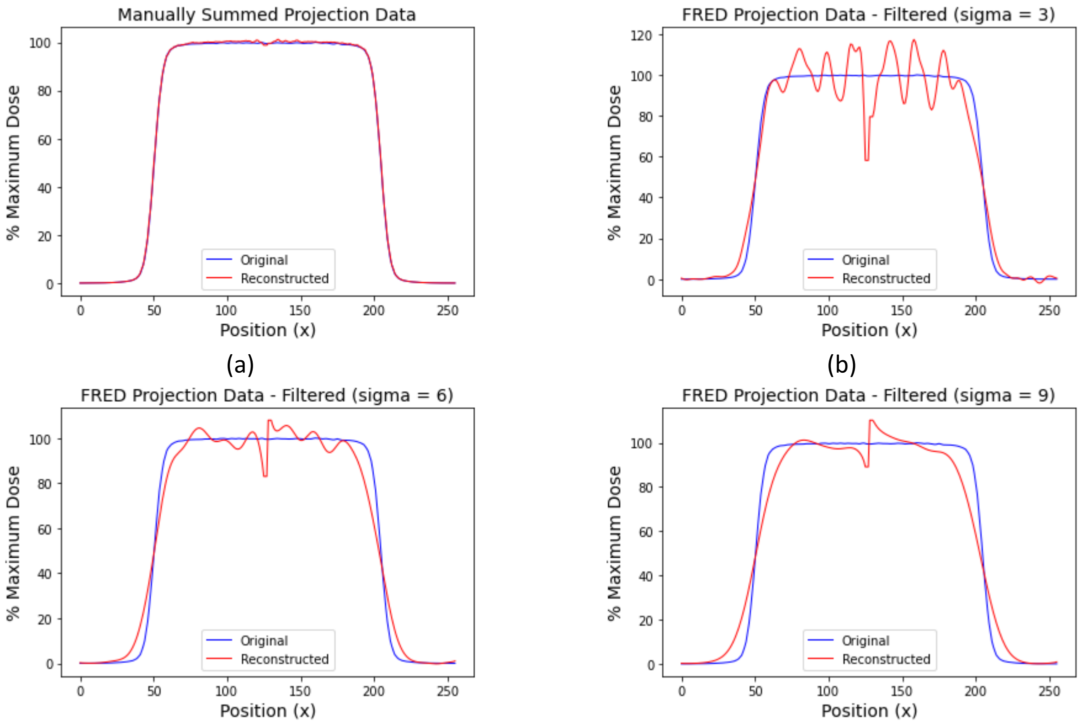

(a) (b) (c) (d)

*Figure 4.17. Effects of filtration on FRED projection reconstruction accuracy. This is shown through a comparison of* $D_{max}$ *profiles for a 30mm TOPAS proton beam reconstructed using the Onion Bordas inverse Abel Transform method. The unfiltered reconstruction for the manually summed projection data is shown in (a). The reconstruction using projection data integrated using FRED with different levels of Gaussian filter applied, specified by a standard deviation of (b) 3, (c) 6 and (d) 9.*

In the lighter filtered reconstruction (4.17b), there is still a large level of noise in the reconstructed image, with the reconstructed profile fluctuation between 20% above and below the original profile. Increasing the filtration reduces this fluctuation, resulting in a better agreement between the reconstructed and original profiles, shown here for the medium (4.17c) and heavily filtered (4.17d) reconstructions. But as the filtration increases the gradient of the beam edge reduces also. The error introduced by this blurring of the beam edge begins to outweigh any reduction in error in the central axis region as the filtering increases. As shown in the heaviest filtered reconstruction, an artefact in the centre of the reconstructed distribution remains, while the edges of the distribution have been blurred significantly. None of the filtered reconstructions reaches the accuracy of the manually summed projection data reconstruction (4.17a).

Due to the different noise profiles in the FRED projections compared to the manually summed projections, the range of inverse Abel transform methods were re-tested on the FRED projection, to determine if any of the other methods performed better than the Onion Bordas method. A 40mm TOPAS proton beam was used, with a Gaussian filter (sigma = 5) applied to the FRED projection before reconstruction. The results for the reconstruction accuracy of the different inverse Abel transform methods are shown in Table 4.7.

*Table 4.7. FRED data reconstruction accuracy for different inverse Abel transform methods. A 40mm TOPAS simulated proton beam distribution was used, with a Gaussian filter (sigma = 5) used to smooth to the projection before reconstruction. This reconstruction was repeated for all available methods in PyAbel.*

| | **PROFILE** | | | | **PDD** | | |
|---|---|---|---|---|---|---|---|
| **METHOD** | **RMSE (%)** | **Beam RMSE (%)** | **CAX RMSE (%)** | **Max Error (%)** | **RMSE (%)** | **RMSE (%)** | **Max Error (%)** |
| **ONION BORDAS** | 9.68 | 13.1 | 16.1 | 26.6 | 12.8 | 30.8 | 60.9 |
| **DIRECT** | 9.89 | 13.5 | 16.9 | 27.4 | 14.5 | 41.7 | 69.4 |
| **BASEX** | 9.94 | 13.5 | 17.0 | 27.6 | 15.1 | 29.2 | 72.4 |
| **HANSEN-LAW** | 10.1 | 13.8 | 17.4 | 28.2 | 14.8 | 38.7 | 70.8 |
| **TWO POINT** | 10.0 | 13.7 | 17.3 | 28.2 | 15.0 | 51.5 | 72.3 |
| **THREE POINT** | 9.91 | 13.4 | 16.9 | 27.5 | 14.6 | 47.9 | 70.1 |
| **ONION PEELING** | 9.97 | 13.6 | 17.1 | 27.8 | 15.2 | 61.3 | 73.0 |
| **DAUN (D=3)** | 9.94 | 13.5 | 17.0 | 27.6 | 15.0 | 55.8 | 71.9 |

The different methods all resulted in a near identical reconstruction, with the calculated accuracy metrics very similar for all reconstructions. The Onion Bordas method is still the most accurate performing out of the range of methods, but there is not a significant difference between them. Figure 4.18 compares the reconstructed $D_{max}$ profiles for the Onion Bordas, Daun and Hansen-Law methods, and shows a very similar reconstructed profile for each method. The fact the different methods all produce a very similar reconstructed profile suggests the limitation of using the inverse Abel transform to reconstruct the FRED projection data lies in the noise within the projection data, rather than the performance of the inverse Abel transform itself.

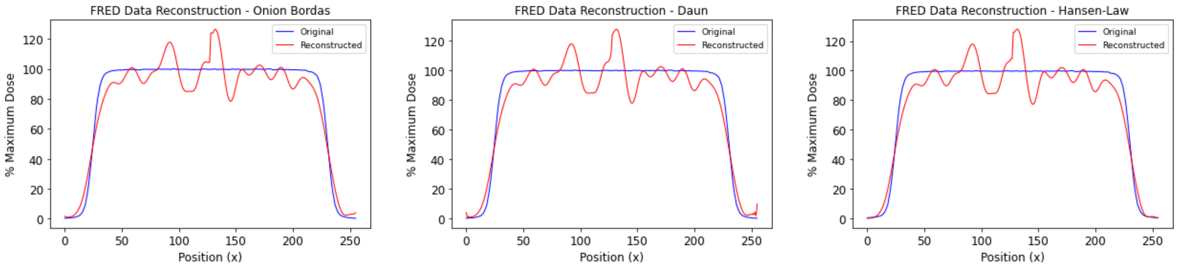

(a) (b) (c)

*Figure 4.18. $D_{max}$ profile comparison for FRED integrated projection data. The Onion Bordas (a), Daun (b) and Hansen-Law (c) methods of inverse Abel transform were used for the reconstruction of a 40mm TOPAS simulated proton beam distribution, with a Gaussian filter (sigma = 5) used to smooth to the projections before reconstruction.*

The individual methods are reconstructing the data they are given, but there is too much noise within that data for that reconstruction to resemble the original distribution. From these results, a 3D reconstruction based on the current performance of the prototype OC dosimeter does not appear to be feasible. To achieve a reconstruction with a clinically relevant level of reconstruction error, which would be in the order of 2% or less, the noise in the FRED projection data needs to be reduced. This concept is explored in the next section, with the reduction in noise in the FRED projections required to achieve an acceptable reconstruction investigated.

## 4.4 FRED Dosimeter Noise Investigation

The noise in the OC dosimeter system that is modelled in FRED comes from a number of different sources [37,56]. Ongoing refinements of the OC dosimeter are aimed at reducing the noise in the measurement system to improve performance [56–59]. The levels of noise modelled in FRED can be adjusted to replicate these improvements. By modelling a number of incremental dosimeter performance increases, the reduction in noise required to produce an accurate 3D reconstruction from a single projection using the inverse Abel Transform can be estimated.

To do this, the 30mm, 35mm and 40mm proton beams were used in the FRED model of the prototype dosimeter. The FRED model was modified for each case, generating projection images with the full modelled noise, then 1/2, 1/4, 1/8 and 1/16 of the full noise levels. For each noise level the individual components contributing to the noise were modified so the overall noise in the projection output contained the desired increment of the full noise level. While the improvements to the OC dosimeter performance are unlikely to result in such a uniform change to the noise level as modelled here, this analysis is simply to indicate the magnitude of performance increase that will be required. A projection image with no modelled noise in the OC dosimeter system was generated also. The difference the noise level has on the projection can be clearly observed, with projections for the 40mm proton beam with no noise, a quarter of full noise, and the full modelled noise shown in Figure 4.19.

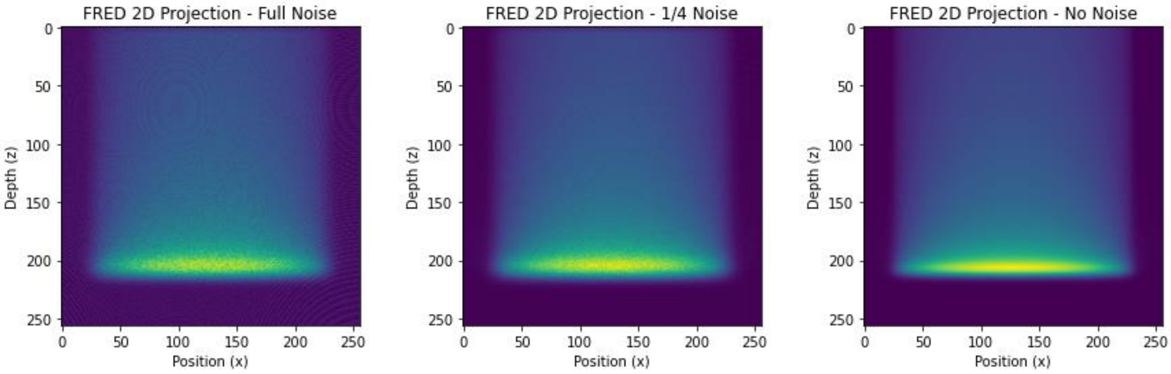

(a) (b) (c)

*Figure 4.19. FRED projections with different levels of modelled noise. A 40mm TOPAS proton beam was run through the FRED virtual dosimeter model, at multiple levels of noise modelled within the dosimeter system. The difference in the sharpness of the projection between the full noise (a), quarter noise (b), and no noise (c) projections is apparent, especially in the Bragg Peak region.*

The Onion Bordas inverse Abel Transform was then performed on each of the FRED projections for each beam size, for each level of noise that was modelled. A Gaussian filter (sigma = 5) was applied to each projection before reconstruction. The reconstruction accuracy was quantified using comparisons of the $D_{max}$ profiles and PDDs between the reconstructed image and original image, with the RMSE, beam RMSE, CAX RMSE, and maximum error calculated for the profiles, and the RMSE, Bragg Peak RMSE, and maximum error calculated for the PDDs. The results for the 35mm and 40mm beam reconstructions are displayed in Figure 4.20, as a plot of the reconstruction error versus the level of modelled noise.

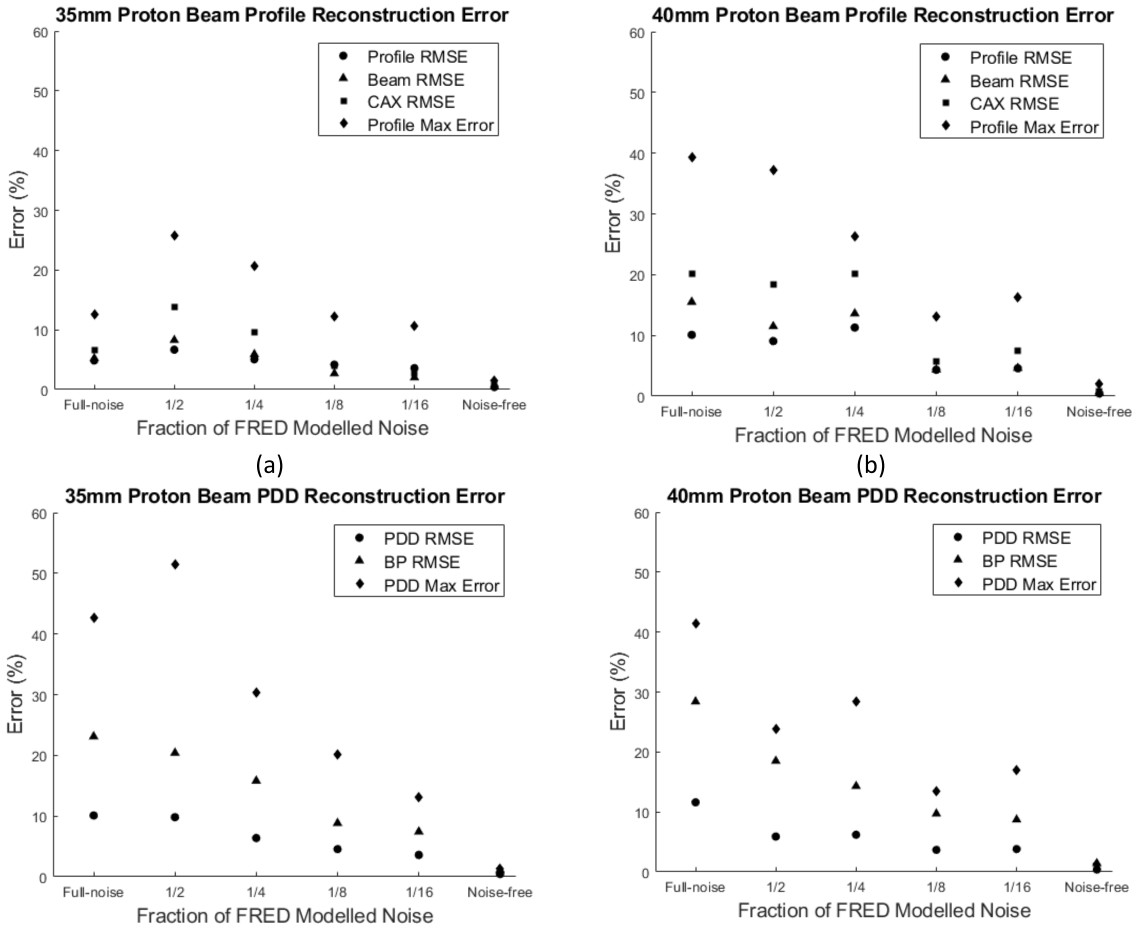

(a) (b)

(c) (d)

*Figure 4.20. Reconstruction error for FRED projections with varying noise. The FRED virtual dosimeter was modelled with increments of the full noise within the detector system. The error in the profile reconstructions for a 35mm (a) and 40mm (b) TOPAS proton beam, and the error in the PDD reconstructions for a 35mm (c) and 40mm (d) proton beam are shown.*

The reconstruction error is plotted against the fraction of FRED modelled noise, ranging from full noise to 1/16th of the full modelled noise. The reconstruction for the FRED projection with no-noise modelled in the dosimeter system is shown also, as the theoretical maximum performance scenario. For both beam sizes, and for both the profile and PDDs, the reconstruction steadily decreases as the modelled noise in the OC dosimeter decreases. The no-noise reconstruction results in errors of 1%, a result that is comparable to the manually summed projection reconstructions in section 4.2. For the 1/8th and 1/16th of the full-noise model, the reconstruction error is around 4%.

This suggests that the noise in the OC dosimeter is the biggest limitation on the accuracy of the 3D dose distribution reconstruction from a single projection. The accuracy of the no-noise reconstruction and the improving performance as the level of noise is reduced suggest the 3D dose reconstruction accuracy would be improved if the noise in the OC dosimeter is reduced substantially.

## 4.5 Square Field Reconstruction

To confirm the limitations of a single projection reconstruction using the inverse Abel transform, the reconstruction of a non-radially symmetric radiation beam was attempted. A MATLAB modelled square photon field of 128 pixels in size was used. The Hansen-Law method was used, as this was found to be the best performing for the circular photon beams. The original 2D central slice, the reconstructed image, and the comparison of $D_{max}$ profiles are shown in Figure 4.21 below.

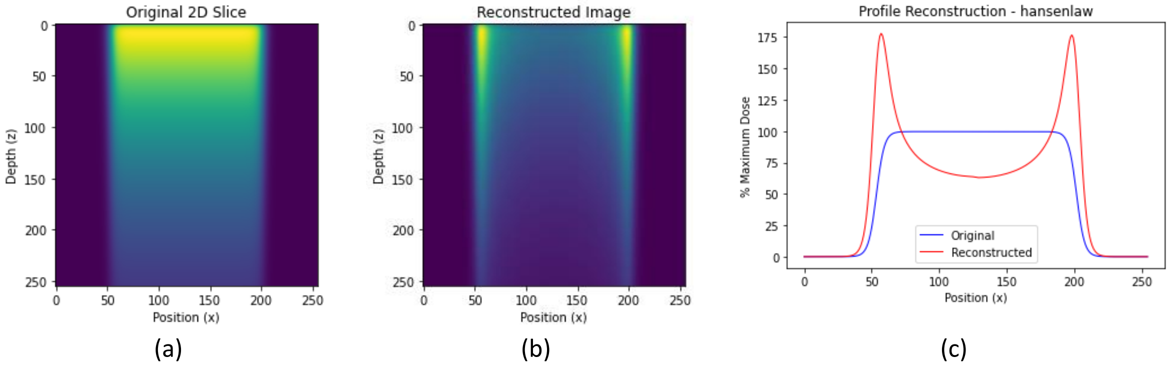

(a) (b) (c)

*Figure 4.21. Single projection reconstruction of a MATLAB modelled square field. The Hansen-Law method of the inverse Abel transform was used to perform the reconstruction. A slice through the centre of the 3D distribution is shown in (a), and the attempted reconstruction of this slice is shown in (b). A comparison of the profiles at $D_{max}$ for each is shown in (c).*

As expected, the reconstruction of a non-radially symmetric field using the inverse Abel transform did not produce an accurate reconstruction. This confirms the expected result, and it can be concluded that the inverse Abel transform is only relevant for radially symmetric fields.

## 4.6 Concluding Remarks

In this chapter the accuracy of using the inverse Abel Transform to reconstruct a 3D dose distribution from a single projection was investigated. The *PyAbel* package was used to implement the inverse Abel transform, and the various methods available in *PyAbel* were tested on a Gaussian distribution, then both proton and photon beam models. The Daun method was the most accurate on the Gaussian, the Onion Bordas method the most accurate on the proton beam, while the Hansen-

Law method was the most accurate for the photon beams. As the best photon beam reconstruction still resulted in errors of greater than 2% with prominent CAX artefacts present, and the more likely application of the OC dosimeter lies in FLASH therapy and proton beams, which are often produced circularly with radial symmetry, the decision was made to focus henceforth on proton beam reconstruction using the Onion Bordas method.

The accuracy of an Onion Bordas inverse Abel Transform was determined for a range of proton beam sizes, finding that in general the reconstruction error increased for the smaller 5mm and 10mm beam sizes but remained relatively consistent for sizes 15mm and larger. FRED optical modelling software was then used to provide a more accurate model of the prototype dosimeter system, with an accurate representation of the noise in the detector system. This decreased the reconstruction performance significantly, with the error in the reconstruction being unable to be reduced below 8%. While this indicates the current dosimeter system is unable to perform a 3D reconstruction from a single projection to an acceptable accuracy with the current levels of noise in the OC dosimeter system, future improvements to the dosimeter system can be modelled as noise reductions in FRED. From this, it was determined that the noise would have to be reduced substantially to achieve results within the range of the desired reconstruction accuracy.

This determines that 3D dose reconstruction from a single projection is possible, albeit with improvements to the dosimeter required. But there are limitations of the single projection reconstruction technique. For one, this would restrict the application of the OC dosimeter to only radially symmetric beams. While these are used in clinical radiation therapy, particularly in the emerging field of FLASH therapy where the OC dosimeter is most likely to be utilised, historical and current clinical MV photon and MeV electron dosimetry protocols commonly specify reference dosimetry in terms of square fields [32,33]. For this dosimeter to be viable across all aspects of clinical dosimetry the ability to handle square fields is desirable. Another limitation is that the single projection approach will not reconstruct any information about any asymmetries in the radially symmetric beam. While this is acceptable for absolute dose measurements on the central axis, or averaged profiles through the beam, any details on the flatness and symmetry of the beam will not be determined from a one projection reconstruction.

As such, then next chapter will investigate the reconstruction accuracy achievable with a two-projection reconstruction technique. This is the least possible increase to the mechanical complexity of a 3D OC dosimeter that has the potential to reconstruct square fields and determine the flatness and symmetry of radiation beams.

# Chapter 5: Two Projection Reconstruction

Chapter 4 showed that the inverse Abel transform could perform an accurate tomographic reconstruction from a single projection, provided the 3D distribution of interest had radial symmetry and low noise. But the inverse Abel transform is limited to only radially symmetric distributions, with it unable to reconstruct, for example, a square field. This chapter will investigate the use of two orthogonal projections for the reconstruction of simple square radiation fields. The modifications to the prototype OC dosimeter required to capture two orthogonal projections simultaneously are relatively minor, involving a second object beam split from the original and directed towards a second camera, so only a small increase to the mechanical complexity of the OC dosimeter. While this is less desirable than a single projection reconstruction, where no modification to the prototype dosimeter was required, the potential benefits of a two-projection reconstruction lie in the ability to move beyond being limited to radially symmetric radiation fields. Being able to reconstruct the square fields commonly used in clinical radiation dosimetry or determine any asymmetries in the radiation beam such as the flatness and symmetry would increase the clinical utility of the OC dosimeter, so is worthy of investigation.

The focus of this chapter will be on investigating the performance of various tomographic reconstruction algorithms to reconstruct simple square, rectangular and circular fields, using only two projections. Circular fields will allow a comparison back to the single projection reconstruction using the inverse Abel Transform and determine any differences in reconstruction accuracy between the two techniques. Reconstruction of any complex beam features is likely outside the capabilities of a two-projection reconstruction, but it is hoped that for basic fields a two-projection tomographic reconstruction will be able to provide useful information. These simple fields are still clinically relevant, representing the radiation beams delivered during reference dosimetry measurements.

Initially the Filtered Back Projection (FBP) algorithm will be used, before investigating the use of a Fast Fourier Transform (FFT) reconstruction. For the reasons discussed in Section 2.4.4, only these two approaches will be considered for the two-projection reconstruction investigation. For this MATLAB modelled photon beam data was used, the generation of which is described in Section 3.1. The TOPAS modelled proton beams were not investigated in this chapter, as the previously modelled beams had radial symmetry, so the inverse Abel transform was used. TOPAS modelled square beams were not generated, as it was desirable to test a wide range of beam parameters to characterise the effect each had on the reconstruction accuracy. The long duration of the TOPAS simulations would have limited the number of beams that could be simulated in the timeframe of this study, so the MATLAB reconstructions were considered more desirable for their speed of modelling and ease of modification of beam features.

The reconstruction accuracy for the different reconstruction algorithms was determined as per the methods described in Section 3.3, and was tested for a variety of size, shape, and intensity of radiation beams, and for different levels of modelled noise within both the radiation beam and the background region. To increase the complexity and better model clinical radiation beams, additional features such as beam penumbra and a wedged intensity field were also modelled. The projection data was generated using MATLABs *radon* function [115] for the FBP reconstructions, and a manual sum for the FFT reconstructions. If the two-projection reconstruction with either technique proves accurate enough, the investigation will be repeated using FRED to simulate the projections, allowing for a more realistic model of the output of the OC dosimeter.

## 5.1 Filtered Back Projection Reconstruction

Filtered back projection was chosen as the initial tomographic reconstruction algorithm to test as it is a well-established and well understood algorithm and is easy to implement in MATLAB using the *iradon* function [116]. It is also quick to compute, saving computational time when simulating a large variety of beam features. In general, most reconstructions using a FBP algorithm would require many more than two projections to accurately determine any features within the reconstructed image. However, as this current application relies only on very basic shapes with homogenous levels of dose within them, it is hoped a two-projection reconstruction may contain enough information for the purposes of this study.

Initial reconstruction attempts were performed on square and circular beams 128 pixels in size, while the rectangular beam was defined as 160 x 80 pixels, each centred within a 256x256 background array. These fields are shown in Figure 5.1 (a-c).

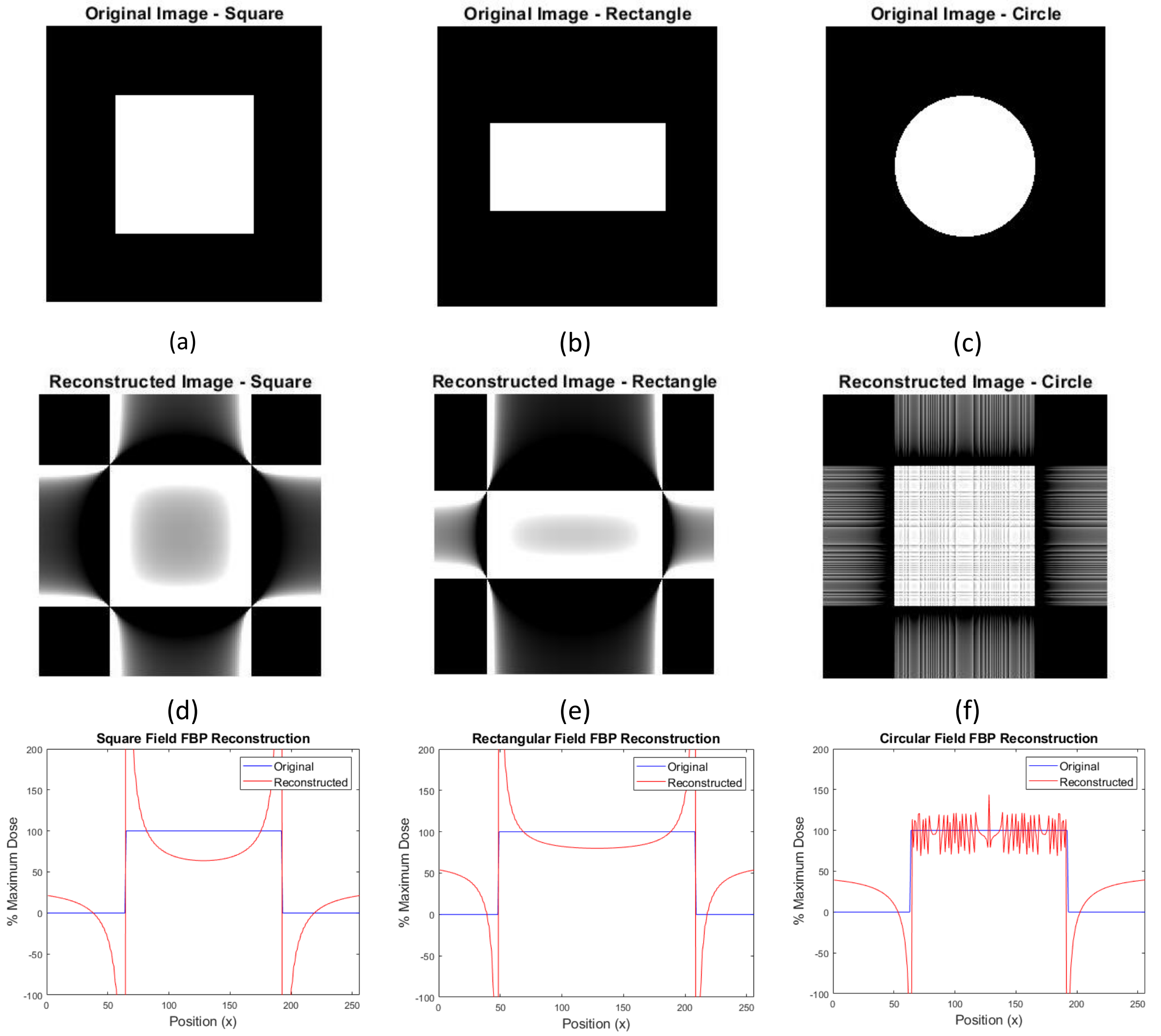

(a) (b) (c)

(d) (e) (f)

(g) (h) (i)

*Figure 5.1. Initial two-projection FPB reconstruction attempts. Two orthogonal projections were taken of a square (a), rectangular (b) and circular (c) radiation field. These projections were reconstructed using a Filtered Back Projection reconstruction algorithm with the default Ram-Lak filter (d), (e) & (f). Profiles along the x-axis through the centre of the radiation beam (g), (h) & (i) compare the reconstructed profile to the profile through the original radiation beam.*

The beams were given a nominal dimensionless dose value of 1.0, while the background was set at 0.0. No noise or penumbra was added to keep the fields simple initially. Projection data was generated using MATLABs *radon* function, summing the data along the X-axis and Y-axis. MATLABs *iradon* function was then used on the projections to perform the FBP reconstruction, using the default Ram-Lak filter. The reconstructed images are shown in Figure 5.1 (d-f). Reconstruction accuracy was evaluated using profiles taken through the centre of the original and reconstructed images, along the X-axis, as shown in Figure 5.1 (g-i). From these profiles the RMSE, Beam RMSE and CAX RMSE were calculated to quantify the reconstruction accuracy. It is immediately clear that a two-projection FBP reconstruction of these basic shapes results in several large reconstruction artefacts. The square and rectangle reconstructions feature very large regions of over- and under- response at the beam edge, while the centre of the radiation beam reconstructs around 30% low for the square and 20% low for the rectangle. Interestingly, the circular field does a better job of reconstructing as a square than the square field does, with a very noisy but on average accurate reconstruction of the profile through the centre of the beam, and an accurate reconstruction of the dose at the central axis. However, these profiles are only accurately matching for orthogonal angles through the centre of the beam. One area where the reconstruction does perform well is determining the beam edge of the square and rectangular beams, as evidenced in the profiles in Figure 5.1.

The large reconstruction artefacts at the beam edge for the square and rectangular FBP reconstructions make it unlikely that an accurate full reconstruction can be performed using only two projections through the direct application of the Radon transform. However, the circular beam reconstruction suggests a reconstruction of the CAX dose is possible with two projections. Other useful information could still be obtained from the reconstructions, such as the position of the beam edge, or the way that the reconstruction accuracy is related to beam parameters such as size and intensity, and beam features such as noise and penumbra. The focus for the rest of the FBP investigation will be to see if this CAX dose can be accurately determined, as this could be considered the most clinically important feature to characterise accurately. The beam and CAX RMSE will be the primary quantifiers of reconstruction accuracy for this section.

### 5.1.1 FBP Filter Choice

The *iradon* function in MATLAB contains five filter options: the default Ram-Lak filter, and the Shepp-Logan, Cosine, Hamming and Hann filters. Each of the latter four filters modifies the Ram-Lak filter to reduce the contribution of high frequency components to the reconstruction. The reconstructions for the square, rectangle and circle field were repeated with each of the filter types to investigate the effect the choice of filter had on reconstruction accuracy, as shown in Table 5.1.

*Table 5.1. Two-projection FBP reconstruction accuracy with filter. The range of filters available in MATLABs iradon function were tested, for square, rectangular, and circular MATLAB modelled photon beams.*

| FILTER | SQUARE | | RECTANGLE | | CIRCLE | |
|---|---|---|---|---|---|---|
| | **Beam RMSE (%)** | **CAX RMSE (%)** | **Beam RMSE (%)** | **CAX RMSE (%)** | **Beam RMSE (%)** | **CAX RMSE (%)** |
| **RAM-LAK** | 31.1 | 36.0 | 18.5 | 19.9 | 17.4 | 13.0 |
| **SHEPP-LOGAN** | 31.1 | 36.0 | 18.4 | 19.9 | 14.5 | 11.1 |
| **COSINE** | 31.1 | 36.0 | 18.4 | 19.9 | 9.91 | 8.57 |
| **HAMMING** | 31.1 | 36.0 | 18.4 | 19.9 | 7.96 | 7.43 |
| **HANN** | 31.1 | 36.0 | 18.4 | 19.9 | 7.44 | 7.21 |

From this, it is clear the choice of filter has no significant effect on the central reconstruction accuracy for either the square or the rectangular field. The circular field reconstruction showed good improvement with the filter choice, with the Hann filter reducing the CAX RMSE to 7%. These results are expected when looking at the nature of the reconstruction artefacts between the square and circular fields, with the square field dominated by a large smooth underestimation of the dose, while the circular field is dominated by high frequency oscillations. The different FBP filters reduce the contribution of the high frequency components to the reconstruction, which is shown in these results as a reduction in the CAX RMSE for the circular field. As the Hann filter is the best performing out of the filter options available in *iradon*, it will be used exclusively for the rest of the FBP investigation.

### 5.1.2 Beam Size

The next step in the two-projection FBP reconstruction investigation was to look at the effect of the beam size on the reconstruction accuracy. The radiation beams were all modelled within a 256x256 array, with the radiation beam centred within this. Beams of 32, 64, 96, 128, 160 and 192 pixels in size were used for the square and circle beams, while the rectangular field used the same sizes for the x-dimension and 80 pixels for the y dimension. As described in Section 3.1, the use of beam expansion and magnification or minification techniques makes the actual width of the modelled radiation beam arbitrary, rather it is the proportion of the 256-pixel image array the radiation beam occupies that is of interest. The beam RMSE was not calculated for any 32- or 64-pixel fields, as the 81 pixels this is defined as is larger than the radiation beam itself for these. The CAX RMSE was also reduced to the central 11 pixels for the 32-pixel fields for the same reason. The results for these reconstructions are shown in Table 5.2 below.

*Table 5.2. Two-projection FBP reconstruction accuracy with field size. Various sized square, rectangle, and circular MATLAB modelled photon beams were investigated.*

| **BEAM SIZE (PIXELS)** | **SQUARE** | | **RECTANGLE** | | **CIRCLE** | |
|---|---|---|---|---|---|---|
| | **Beam RMSE (%)** | **CAX RMSE (%)** | **Beam RMSE (%)** | **CAX RMSE (%)** | **Beam RMSE (%)** | **CAX RMSE (%)** |
| **32** | n/a | 33.4 | n/a | 5.12 | n/a | 7.51 |
| **64** | n/a | 34.8 | n/a | 33.0 | n/a | 8.30 |
| **96** | 28.2 | 35.7 | 27.4 | 34.6 | 6.62 | 7.71 |
| **128** | 31.1 | 36.0 | 25.5 | 28.6 | 7.44 | 7.21 |
| **160** | 33.2 | 36.1 | 18.4 | 19.9 | 6.43 | 6.33 |
| **192** | 34.2 | 36.2 | 8.97 | 9.76 | 6.91 | 6.21 |

Increasing the beam size steadily decreases the accuracy of the square field reconstruction, with the CAX RMSE increasing from 33% to 36% as the beam size increases from 32 to 192 pixels. The rectangle field reconstruction showed a different trend, with a reduced error for the smallest beam (5%), jumping up to above 30% for the middle-sized beams. The reconstruction error then steadily reduced as the beam size increased, finishing with a CAX RMSE of 10% for the largest field. The circle beam steadily improved from 8% to 6% as the beam size increased.

### 5.1.3 Beam Intensity

All the beams modelled in MATLAB so far have had a background intensity of 0.0, representing the assumption of a background subtraction being performed during the processing of the prototype OC dosimeter output. Based on FRED simulations of the dosimeter output for un-irradiated water, this background should have a value of 0.02. The same FRED simulations were run for different levels of dose, to determine the pixel value relative to the background level for each dose level, as shown in Table 5.3. Setting the background to 0.02 and varying the intensity of the beam relative to this investigates the contrast sensitivity of a two-projection reconstruction and could determine a minimum level of dose required to achieve an accurate reconstruction.

*Table 5.3. Relationship between dose and pixel value for FRED modelled radiation beams.*

| DOSE (GY) | PIXEL VALUE | RELATIVE TO BACKGROUND |
|---|---|---|
| **0** | 0.02 | 1.0 |
| **0.5** | 0.034 | 1.7 |
| **1.0** | 0.05 | 2.5 |
| **2.0** | 0.10 | 5.0 |
| **4.0** | 0.25 | 12.5 |
| **8.0** | 0.45 | 22.5 |
| **16.0** | 0.80 | 40.0 |

Square, circle, and rectangular radiation beams 128 and 160x80 pixels in size respectively were modelled in MATLAB, with beam intensity values matching the dose values in Table 5.3 and the background intensity set to 0.02. The beam and CAX RMSE were calculated for each reconstruction, for each of the beam shapes. The relationship between beam intensity and reconstruction accuracy is shown in Figure 5.2.

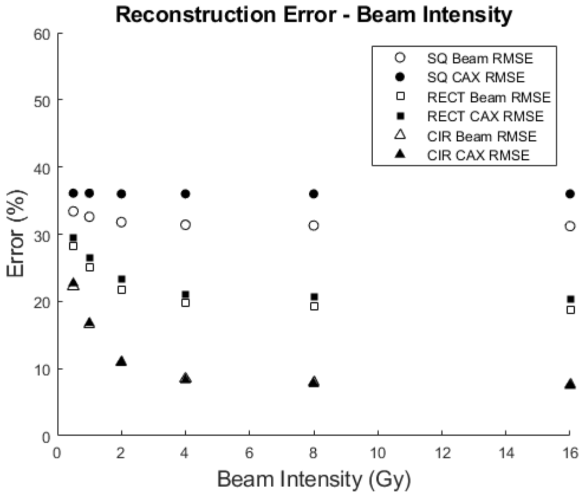

*Figure 5.2. Relationship between the reconstruction error and dose. A two-projection filtered back projection reconstruction was performed, for varying levels of dose in a MATLAB modelled square, rectangular, and circular photon beams.*

For all measures of error for each of the beam shapes, the calculated reconstruction error was consistent with delivered dose for doses above 4 Gy but increases as the intensity is reduced below this. Based on this result, to avoid adding additional error the dose measured with the prototype OC Dosimeter using a two-projection reconstruction should be limited to use in applications where doses of 4 Gy or more are delivered.

### 5.1.4 Beam Noise

Due to the stochastic nature of a radiation beam, small fluctuations in the measured dose within the beam are expected [67,70]. A simple model of this feature can be added to the MATLAB beam model by adding random noise to each pixel of the image, as a percentage of the maximum dose value. The dose reconstruction was repeated for the standard square, circle and rectangular radiation fields used above, but with various levels of additional noise added to the beam model. The effect this noise has on the reconstruction accuracy can then be quantified, as shown in Table 5.4.

*Table 5.4. Two-projection FBP reconstruction error for various levels of added noise. Square, rectangular, and circular MATLAB modelled photon beams were used in the reconstruction.*

| **ADDED NOISE (%)** | **SQUARE** | | **RECTANGLE** | | **CIRCLE** | |
|---|---|---|---|---|---|---|
| | **Beam RMSE (%)** | **CAX RMSE (%)** | **Beam RMSE (%)** | **CAX RMSE (%)** | **Beam RMSE (%)** | **CAX RMSE (%)** |
| **0** | 31.1 | 36.0 | 18.4 | 19.9 | 7.44 | 7.21 |
| **0.5** | 31.2 | 36.0 | 18.5 | 19.9 | 7.38 | 7.20 |
| **1.0** | 30.9 | 35.7 | 18.6 | 20.1 | 7.44 | 7.31 |
| **2.0** | 30.9 | 35.6 | 18.5 | 20.3 | 7.75 | 7.04 |
| **5.0** | 32.8 | 37.0 | 18.9 | 20.7 | 8.94 | 9.02 |

The additional noise has little impact on the reconstruction error for either the square, rectangle, or circular radiation beam, with the beam and CAX RMSE remaining constant with as the added noise increases. Only when the additional noise reached 5% did the calculated reconstruction error increase. This suggests the two-projection approach using filtered back projection is relatively insensitive to noise.

### 5.1.5 Beam Penumbra

One way to make the MATLAB modelled radiation beams more representative of a clinical radiation beam is to approximate the penumbra at the beam edge. For these models, this was done using a *tanh(x)* function for a region of the dose distribution at the beam edge, the size of which was defined as the penumbra width. The width of the penumbra could be varied, and the resulting effect this has on the reconstruction accuracy investigated. These results can be found in Table 5.5.

*Table 5.5. Two-projection FBP reconstruction accuracy with penumbra width. Square, rectangular, and circular MATLAB modelled photon beams were investigated.*

| **PENUMBRA WIDTH** | **SQUARE** | | **RECTANGLE** | | **CIRCLE** | |
|---|---|---|---|---|---|---|
| | **Beam RMSE (%)** | **CAX RMSE (%)** | **Beam RMSE (%)** | **CAX RMSE (%)** | **Beam RMSE (%)** | **CAX RMSE (%)** |
| **0** | 31.1 | 36.0 | 18.4 | 19.9 | 7.44 | 7.21 |
| **8** | 30.2 | 35.9 | 15.5 | 17.0 | 5.47 | 7.00 |
| **16** | 29.2 | 35.8 | 11.6 | 13.2 | 5.29 | 7.18 |
| **24** | 28.2 | 35.8 | 6.37 | 7.94 | 4.97 | 7.00 |
| **32** | 29.6 | 35.6 | 3.04 | 0.12 | 5.34 | 7.18 |
| **40** | 35.8 | 35.5 | 16.5 | 14.1 | 9.11 | 7.18 |
| **48** | 31.8 | 35.3 | 41.0 | 38.7 | 13.0 | 6.94 |

The beam RMSE and CAX RMSE was calculated for each shape of radiation field, for a penumbra width ranging from 8 pixels to 48 pixels on all edges of the radiation beam. The results show that for the square fields the reconstruction error remained constant with increasing penumbra width, with a beam RMSE of around 30% and CAX RMSE of around 35%. The rectangular and circular fields showed more variation, with both rectangle error measures and the circle beam RMSE decreasing as the penumbra width increased to 32 pixels. As it increased above 32 pixels the error increased again. The circle CAX RMSE remained constant over all beam sizes.

The cause of this variation in the rectangular field reconstruction beam RMSE is due to the large beam edge artefact moving towards the centre of the beam as the penumbra width is increased, so the beam region begins to include this in the RMSE calculations for the largest widths. The rectangle CAX RMSE error is variation is notable, as it reaches a minimum value of 0.1% for the 32-pixel penumbra with, which would indicate an accurate reconstruction. This reconstruction is examined more closely in Figure 5.3. Looking at the rectangle beam reconstructed and original profile comparisons for the 24-, 32- and 40-pixel penumbra widths, it is evident that the reconstruction still contains the large beam edge artefact. But as the penumbra width is increased and the edge of the dose distribution becomes more curved, this artefact flattens and spreads out, increasing the reconstructed dose in the centre of the reconstruction.

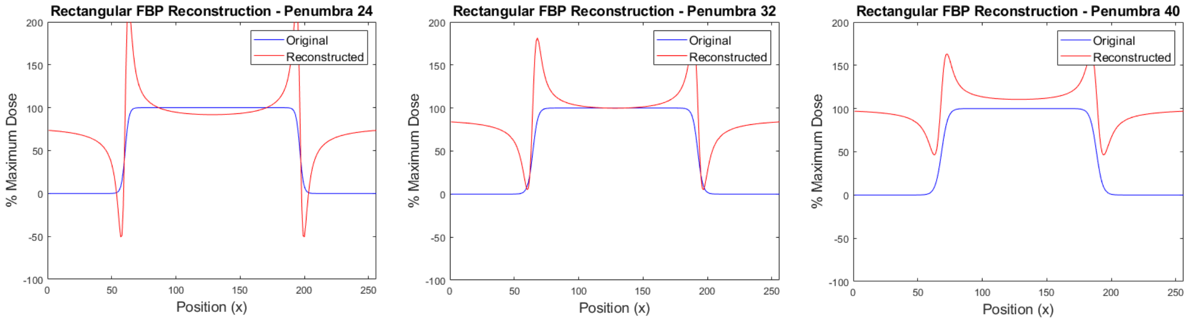

(a) (b) (c)

*Figure 5.3. Effects of penumbra on two-projection FBP rectangular field reconstruction.* $D_{max}$ *profiles are compared for the original MATLAB modelled rectangular photon beam distribution and the reconstructed distribution, for 24-pixel (a), 32-pixel (b), and 40 (c) width of modelled penumbra.*

For the 32-pixel penumbra, this causes a close agreement between the reconstructed and original dose in the centre of the distribution. Unfortunately, this low reconstruction error appears to be a coincidence caused by the beam edge artefact, rather than a sign of an accurate reconstruction. As the reconstruction still contains large reconstruction artefacts at the beam edge, and the CAX dose reconstruction is not accurate for other widths of modelled penumbra, this reconstruction is not deemed to be reliable.

### 5.1.6 Wedged Intensity Beam

An additional complexity that can be added to the MATLAB modelled radiation beams is a wedged intensity across the dose distribution. Wedged fields are a treatment technique used to compensate for patient contour or tissue inhomogeneity variations [117]. Provided that one of the orthogonal projections used in the two-projection reconstruction technique is parallel to the wedge angle, a wedged intensity field represents another complexity of a clinical radiation beam that can be incorporated into the MATLAB beam model.

Here, the wedge angle is defined as the magnitude of the variation of the dose intensity across the width of the distribution. For example, the 40° wedge will result in a dose variation of 1.2 to 0.8 across the 128-pixel beam width. Wedge angle was varied from 0 to 60° in 10° increments, for each of the square, rectangle, and circle radiation beams. Beam RMSE and CAX RMSE were calculated for each reconstruction. The variation of reconstruction accuracy with wedge angle can be found in Table 5.6.

*Table 5.6. Two-projection FBP reconstruction accuracy for a variety of wedge angles. Square, rectangular, and circular MATLAB modelled photon beams were investigated.*

| **WEDGE ANGLE (°)** | **SQUARE** | | **RECTANGLE** | | **CIRCLE** | |
|---|---|---|---|---|---|---|
| | **Beam RMSE (%)** | **CAX RMSE (%)** | **Beam RMSE (%)** | **CAX RMSE (%)** | **Beam RMSE (%)** | **CAX RMSE (%)** |
| **0** | 31.1 | 36.0 | 18.4 | 19.9 | 7.44 | 7.21 |
| **10** | 31.1 | 36.0 | 18.5 | 19.9 | 7.44 | 7.21 |
| **20** | 31.1 | 36.0 | 18.6 | 19.9 | 7.45 | 7.22 |
| **30** | 31.2 | 36.0 | 18.7 | 20.0 | 7.46 | 7.22 |
| **40** | 31.2 | 36.1 | 18.9 | 20.0 | 7.48 | 7.23 |
| **50** | 31.2 | 36.1 | 19.1 | 20.1 | 7.49 | 7.24 |
| **60** | 31.2 | 36.1 | 19.4 | 20.1 | 7.51 | 7.24 |

These results show that the wedge angle had very little effect on the error in the reconstruction, for both the beam RMSE and CAX RMSE, for the square, rectangle, and circle beam reconstructions. This can be confirmed through an examination of profiles comparing the original dose distribution to the reconstructed one, such as the one in Figure 5.4 for the reconstruction of circular and square beams with a 60° wedge applied.

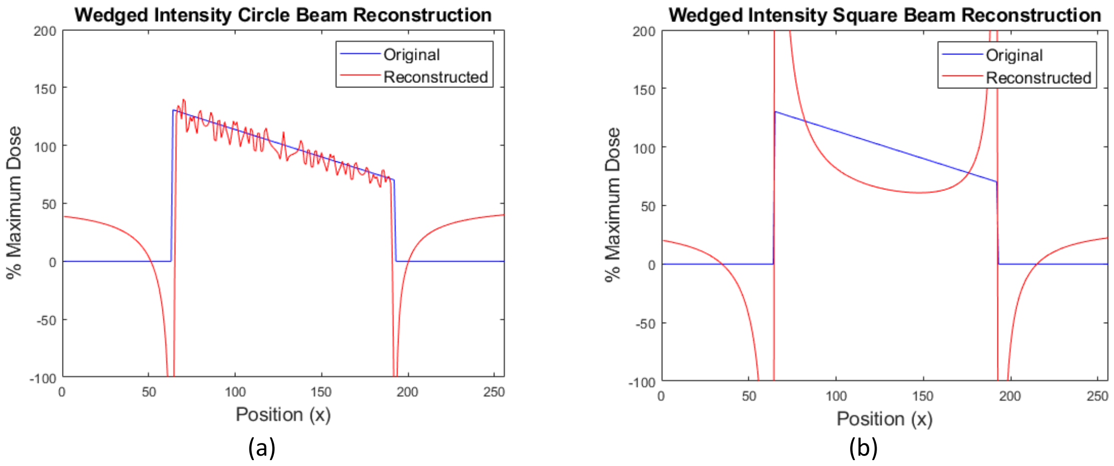

(a) (b)

*Figure 5.4. Wedged intensity beam two-projection FBP reconstruction profile comparison. The $D_{max}$ profiles for original MATLAB modelled circular (a) and square (b) photon beam distributions, and the reconstructed distributions are displayed, for beams with a 60° wedged intensity modelled.*

These profiles show that for the circular beam the wedge angle is reconstructed almost perfectly. The beam edge artefact and noise in the beam region are still present, unchanged from the unwedged beam, but the gradient of the reconstructed dose matches the original dose well. For the square field the large artefacts in the reconstruction make it hard to make a conclusive judgement on any changes to the reconstruction accuracy with wedge angle.

## 5.2 Fast Fourier Transform Reconstruction

The second tomographic reconstruction algorithm to investigate for the two-projection reconstruction portion of this study is the Fast Fourier Transform (FFT). This follows a similar structure to the FBP reconstruction, with initial reconstruction attempts performed on 256x256 MATLAB generated beam models representing an x-y slice of dose at depth, as shown in Figure 5.5 (a-c).

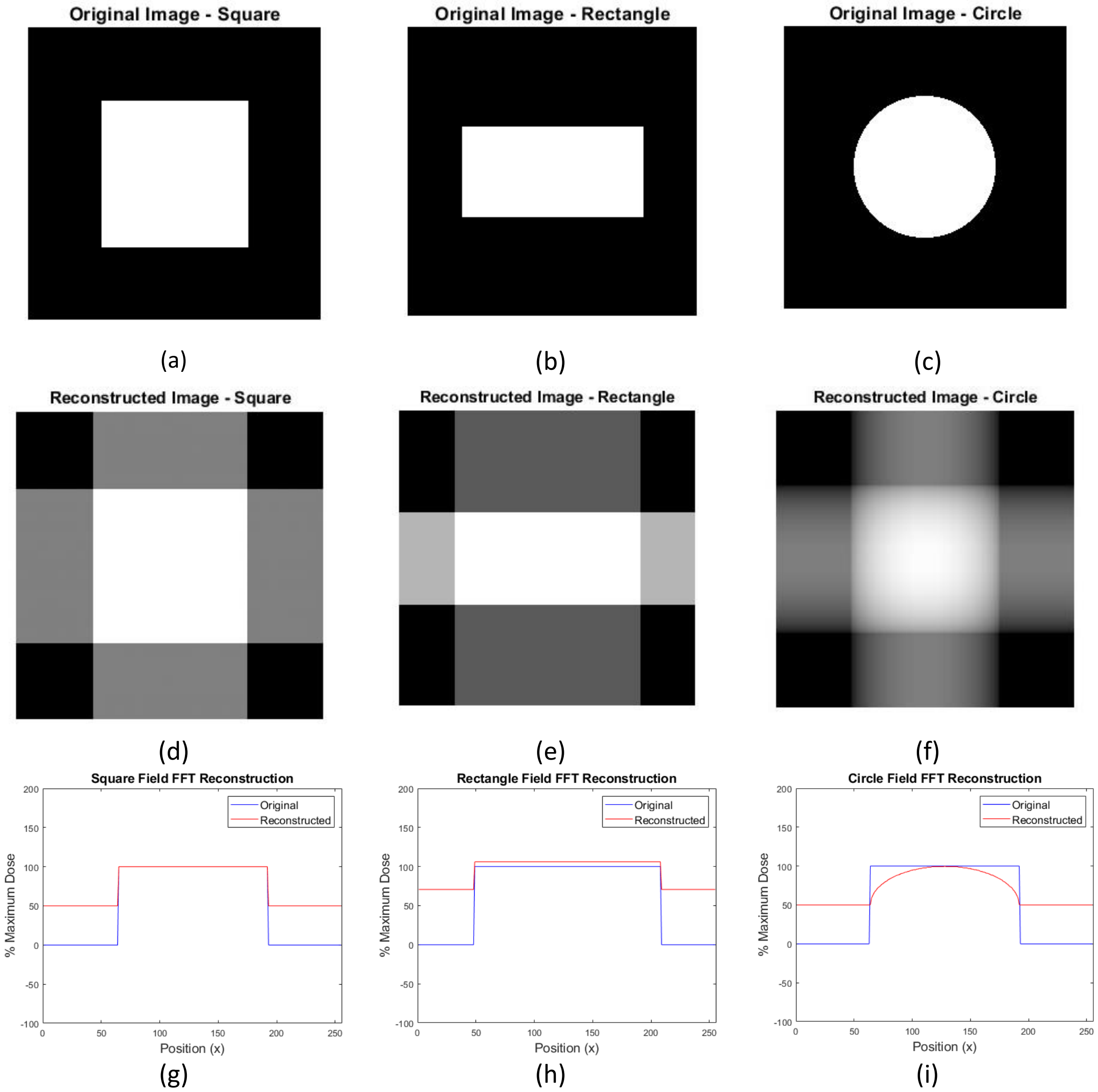

*Figure 5.5. Initial two-projection FFT reconstruction attempts. Two orthogonal projections were taken of a square (a), rectangular (b) and circular (c) radiation field. These projections were reconstructed using a FFT reconstruction algorithm (d), (e) & (f). Profiles along the x-axis through the centre of the radiation beam (g), (h) & (i) compare the reconstructed profile to the profile through the original radiation beam.*

The modelled beams consisted of a 128x128 pixel square radiation beam, a 128-pixel diameter circular beam, and a 160x80 pixel rectangular beam. The beams had a dose value of 1.0 and the background 0.0. Projection data was generated by summing through the dose distribution at orthogonal angles, along the x and y axis. A simple Fourier reconstruction algorithm was developed, with the FFT of the projections taken and summed in k-space, then the inverse FFT taken to produce the reconstructed image. The reconstructed image was then scaled proportional to the width of the radiation beam in each projection to reconstruct the dose. The reconstruction accuracy was evaluated using profiles taken through the centre of the original and reconstructed images, along the X-axis. From these profiles the RMSE, beam RMSE and CAX RMSE were calculated to quantify the reconstruction accuracy, as defined in Section 3.3. The initial attempts at a FFT reconstruction of a square, rectangular, and circular field are shown in Figure 5.5 (d-f). These initial reconstructions resulted in more accurate reconstructions compared to the FBP two projection reconstructions, with no sign of the large reconstruction artefacts that were prevalent in the FBP technique, as displayed in Figure 5.5 (g-i). The square field results in a near perfect reconstruction in the beam region, with an overestimation of the dose outside of this. The rectangular field results in a slight overestimation of the dose, while the circle field is accurate in the very centre of the beam but underestimates the dose towards the edge of the beam.

This square field result is particularly promising, capable of a very accurate reconstruction of a square field from two orthogonal projections. The next step was to characterise the FFT reconstruction for a range of beam sizes and intensities, and then investigate the effect adding features more representative of a clinical radiation beam has on the reconstruction accuracy, such as noise, penumbra, and wedged intensity.

### 5.2.1 Beam Size

Similar to Section 5.1.2 for the FBP reconstruction, the effect the size of the radiation beam, and hence the width of the beam within the image array, has on the reconstruction quality is investigated.

Beams of 32, 64, 96, 128, 160 and 192 pixels in size were modelled for the square and circle beams, while the rectangular field used these same sizes for the x-dimension and 80 pixels for the y-dimension. The beam RMSE was not calculated for any 32- or 64-pixel fields, as the 81 pixels this is defined as is larger than the radiation beam for these fields. The CAX RMSE was also reduced to the central 11 pixels for the 32-pixel fields for the same reason. The results for these reconstruction attempts are displayed in Table 5.7.

*Table 5.7. Two-projection FFT reconstruction accuracy for a variety of beam sizes. MATLAB modelled square, rectangular, and circular photon beams were investigated.*

| **BEAM SIZE (PIXELS)** | **SQUARE** | | **RECTANGLE** | | **CIRCLE** | |
|---|---|---|---|---|---|---|
| | **Beam RMSE (%)** | **CAX RMSE (%)** | **Beam RMSE (%)** | **CAX RMSE (%)** | **Beam RMSE (%)** | **CAX RMSE (%)** |
| **32** | n/a | 0.0 | n/a | 10.7 | n/a | 2.89 |
| **64** | n/a | 0.0 | n/a | 0.62 | n/a | 1.47 |
| **96** | 0.0 | 0.0 | 0.42 | 0.42 | 9.84 | 0.98 |
| **128** | 0.0 | 0.0 | 2.77 | 2.77 | 5.16 | 0.74 |
| **160** | 0.0 | 0.0 | 6.07 | 6.07 | 3.28 | 0.59 |
| **192** | 0.0 | 0.0 | 9.73 | 9.73 | 2.26 | 0.49 |

The two-projection FFT reconstruction generated no error for the square field reconstruction, with the original and reconstructed dose distributions agreeing perfectly for all beam sizes. The rectangular field reconstruction was best for the 96-pixel beam with a 0.4% error for both the beam and CAX RMSE, before the error increased as the field sized increased or decreased. The circle beam steadily improved in accuracy as the beam size increased, with the largest beam size resulting in a 2.2% beam RMSE and a 0.5% CAX RMSE.

### 5.2.2 Beam Intensity

Following the procedure of 5.1.3, the background pixels were set to a value of 0.02 to represent un-irradiated water, and the beam pixels set to various values corresponding to various levels of deposited dose, to investigate the effects of beam intensity of the reconstruction accuracy. The results for this investigation can be found in Table 5.8.

*Table 5.8. Two-projection FFT reconstruction accuracy with beam intensity. MATLAB modelled square, rectangular, and circular photon beams were investigated.*

| BEAM INTENSITY (GY) | SQUARE | | RECTANGLE | | CIRCLE | |
|---|---|---|---|---|---|---|
| | Beam RMSE (%) | CAX RMSE (%) | Beam RMSE (%) | CAX RMSE (%) | Beam RMSE (%) | CAX RMSE (%) |
| **0.5** | 20.3 | 20.3 | 21.6 | 21.6 | 21.0 | 20.3 |
| **1.0** | 29.7 | 29.7 | 31.6 | 31.6 | 30.7 | 29.7 |
| **2.0** | 39.8 | 39.8 | 39.8 | 39.8 | 41.1 | 39.7 |
| **4.0** | 45.8 | 45.8 | 45.8 | 45.8 | 47.3 | 45.8 |
| **8.0** | 47.6 | 47.6 | 47.6 | 47.6 | 49.1 | 47.5 |
| **16.0** | 48.5 | 48.5 | 48.5 | 48.5 | 50.2 | 48.5 |

Interestingly, the FFT reconstruction error showed the opposite relationship to beam intensity compared to the FBP reconstruction, with the largest errors found for the high dose beams, and the error decreasing as the dose increased. The large error is likely a result of the background pixels having a non-zero intensity value, so when these are included in the integration of the projections it creates a scaling error in the final reconstruction. The error decreasing with dose, and therefore the relative difference between the background and beam pixels, is unexpected. From this result it is recommended that a background correction be performed prior to the FFT reconstruction to avoid this error.

### 5.2.3 Beam Noise

To create a more accurate model of a clinical radiation beam, random noise was added to each of the beam models to represent the fluctuations found throughout a dose distribution due to the stochastic nature of radiation. The reconstruction accuracy for each beam shape was determined for several noise levels, ranging from 0.5% to 5%, as show in Table 5.9.

*Table 5.9. Two-projection FFT reconstruction accuracy with modelled noise levels. MATLAB modelled square, rectangular, and circular photon beams were investigated.*

| ADDED NOISE (%) | SQUARE | | RECTANGLE | | CIRCLE | |
|---|---|---|---|---|---|---|
| | Beam RMSE (%) | CAX RMSE (%) | Beam RMSE (%) | CAX RMSE (%) | Beam RMSE (%) | CAX RMSE (%) |
| **0** | 0.0 | 0.0 | 6.07 | 6.07 | 5.16 | 0.74 |
| **0.5** | 0.29 | 0.29 | 6.05 | 6.05 | 5.16 | 0.71 |
| **1.0** | 0.56 | 0.64 | 6.10 | 6.34 | 5.14 | 1.17 |
| **2.0** | 1.15 | 1.08 | 6.18 | 6.03 | 5.36 | 0.99 |
| **5.0** | 2.7 | 2.67 | 6.43 | 7.46 | 5.81 | 2.46 |

Despite the beam and RMSE error steadily increasing as the noise increased for the square reconstruction, this error remains at around half the amount of noise added to the radiation beam. A comparison of the original and reconstructed profiles for the square field with 1% and 5% noise added is shown in Figure 5.6, with the reconstructed dose proving a good estimate of the average of the original dose distribution.

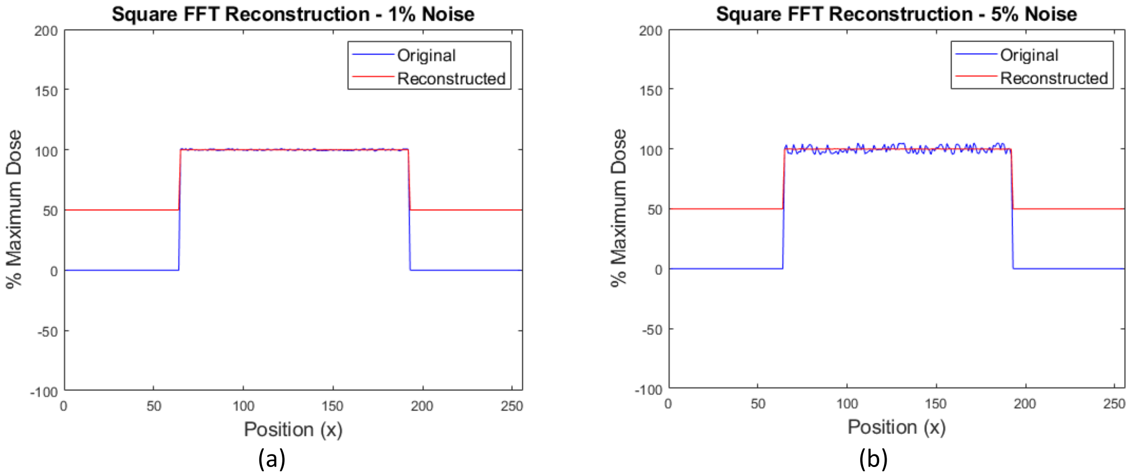

*Figure 5.6. Effects of noise on the two-projection FFT reconstruction. The $D_{max}$ profiles for a MATLAB modelled square photon beam distributions and the reconstructed distributions is shown, with 1% (a) and 5% (b) noise within the beam modelled.*

For the rectangle and circular beams, the reconstruction error remained at a level similar to the zero-noise reconstruction for up until 2% noise added. A larger increase in reconstruction error for the 5% added noise was observed, but the magnitude of this increase in error remained smaller than the level of noise added. These results suggesting the two projection FFT reconstruction is relatively insensitive to noise, for square, rectangular, and circular field reconstruction.

### 5.2.4 Beam Penumbra

Adding penumbra to the beam model is another way of making the making the MATLAB beam model a closer approximation of a clinical radiation beam. Penumbra were added to the beam edge by the same method as described in Section 3.1, for each of the square, rectangle, and circular fields. The resulting reconstruction error calculated as the penumbra width is increased is displayed in Table 5.10.

*Table 5.10. Two-projection FFT reconstruction accuracy with different penumbra width. MATLAB modelled square, rectangular, and circular photon beams were investigated.*

| **PENUMBRA WIDTH** | **SQUARE** | | **RECTANGLE** | | **CIRCLE** | |
|---|---|---|---|---|---|---|
| | **Beam RMSE (%)** | **CAX RMSE (%)** | **Beam RMSE (%)** | **CAX RMSE (%)** | **Beam RMSE (%)** | **CAX RMSE (%)** |
| **0** | 0.0 | 0.0 | 6.07 | 6.07 | 5.16 | 0.74 |
| **8** | 3.23 | 3.23 | 1.53 | 1.53 | 7.12 | 2.38 |
| **16** | 8.20 | 8.20 | 2.58 | 2.58 | 12.2 | 7.37 |
| **24** | 13.3 | 13.3 | 7.62 | 7.62 | 17.8 | 12.5 |
| **32** | 18.6 | 18.6 | 13.5 | 13.5 | 23.6 | 17.9 |
| **40** | 22.0 | 22.8 | 19.1 | 19.1 | 28.1 | 23.4 |
| **48** | 25.9 | 28.6 | 24.7 | 24.7 | 30.7 | 29.1 |

For the square and circle fields investigated, adding penumbra to the beam model resulted in a significant increase in the reconstruction error, with this error increasing as the penumbral width is increased. For the rectangular field, the 8- and 16-pixel penumbra width beams resulted in a reduction in the calculated reconstruction error, before the error began to increase as the penumbra width was increased beyond this. Much like the case for the rectangular field and penumbra width for the FBP reconstruction, this was a result of the error introduced into the reconstruction by the penumbra counteracting the natural overestimation of the dose for the rectangular beam, rather than a removal of the individual sources of error themselves. This can be seen in the profile comparisons of the rectangle beam with 0-, 16- and 32-pixel penumbra width in Figure 5.7 below.

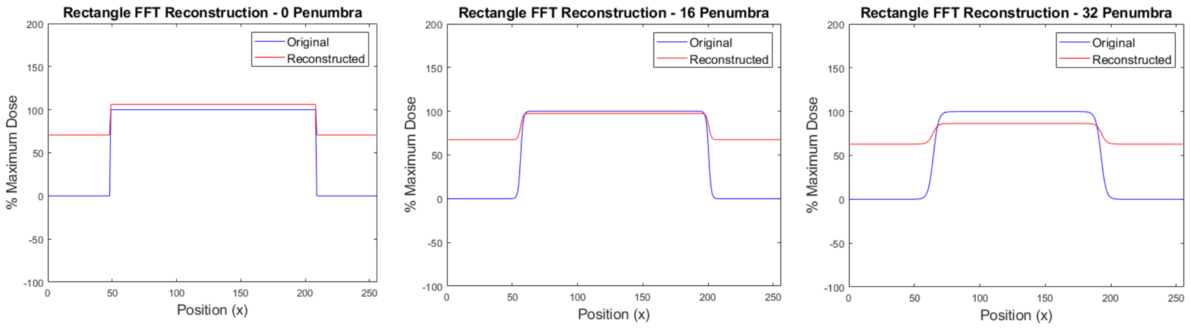

(a) (b) (c)

*Figure 5.7. Effects of penumbra on two-projection FFT rectangular field reconstruction. $D_{max}$ profiles for the original dose distribution and the reconstructed dose distribution are compared, for a MATLAB modelled rectangular photon beam with modelled penumbra of 0 (a), 16 (b) and 32 (c) pixels in width.*

## 5.2.5 Wedged Intensity Beam

The final beam complexity investigated for the two-projection FFT reconstruction was the addition of a wedged intensity to the radiation beam model. With the wedge angle aligned parallel to one of the orthogonal projections, the reconstruction was repeated for the square, rectangle, and circular fields, for a variety of wedge angles defined as in 5.1.6. The results from this investigation are shown in Table 5.11.

*Table 5.11. Two-projection FFT reconstruction accuracy with wedge angle. MATLAB modelled square, rectangular, and circular photon beams were investigated.*

| **WEDGE ANGLE (°)** | **SQUARE** | | **RECTANGLE** | | **CIRCLE** | |
|---|---|---|---|---|---|---|
| | **Beam RMSE (%)** | **CAX RMSE (%)** | **Beam RMSE (%)** | **CAX RMSE (%)** | **Beam RMSE (%)** | **CAX RMSE (%)** |
| **0** | 0.0 | 0.0 | 6.07 | 6.07 | 5.16 | 0.74 |
| **10** | 0.92 | 0.13 | 6.12 | 6.05 | 5.27 | 0.75 |
| **20** | 1.84 | 0.25 | 6.32 | 6.03 | 5.57 | 0.78 |
| **30** | 2.76 | 0.38 | 6.65 | 6.02 | 6.05 | 0.83 |
| **40** | 3.68 | 0.50 | 7.10 | 6.01 | 6.66 | 0.90 |
| **50** | 4.60 | 0.63 | 7.63 | 6.01 | 7.37 | 0.97 |
| **60** | 5.52 | 0.76 | 8.25 | 6.01 | 8.15 | 1.06 |

The reconstruction error steadily increases as the wedge angle increases, for all measures of error apart from the rectangle CAX RMSE, which remained constant at 6% for all wedge angles. This increase in error was particularly prominent for the square field beam RMSE, increasing from zero error for the unwedged beam to 5.5% error for the 60° wedged beam. This can be illustrated from looking at the reconstructed profiles shown in Figure 5.8 for the square fields with a 0°, 30° and 60° wedge.

(a) (b) (c)

*Figure 5.8. Two-projection FFT reconstruction accuracy for wedged intensity square fields. $D_{max}$ profiles for the original dose distribution and the reconstructed dose distribution are compared, for a MATLAB modelled square photon beam with a 0° (a), 30° (b) and 60° (c) wedge modelled.*

The profile comparisons show that the FFT reconstruction is unable to reconstruct a wedged angle correctly, with the magnitude of the angle being underestimated. This results in a reconstruction error that increases in magnitude further from the central axis of the beam and increases as the wedge angle increases.

## 5.3 IMRT Field Reconstruction

The final step in the two-projection reconstruction investigation is to look at what happens when the FBP and FFT reconstructions attempt to reconstruct a square field with a more complex, inhomogeneous dose distribution within it. This approximates an Intensity Modulated Radiation Therapy (IMRT) radiation field, containing different dose levels and multiple dose gradients in both dimensions within the radiation beam. It must be acknowledged that as the two-projection reconstruction of simple fields did not perform a tomographic reconstruction accurately, it is expected that the reconstruction of a more complex field will also not result in an accurate reconstruction. The purpose of this section is to establish a baseline for the IMRT beam reconstruction accuracy, for comparison to the multi-projection technique in Chapter 6. The IMRT beam was modelled as described in Section 3.1.

A two-projection reconstruction was performed for both the FBP and FFT reconstruction algorithms. The reconstruction accuracy was assessed through the comparison of profiles through the original and reconstructed dose distribution, with the RMSE, Beam RMSE and CAX RMSE calculated as detailed in 3.3. The results of the IMRT beam reconstruction are shown in Table 5.12 below.

*Table 5.12. Two-projection IMRT field reconstruction accuracy. A two-projection FBP and FFT reconstruction of a MATLAB modelled IMRT photon field was investigated.*

| **METHOD** | **IMRT** | | |
|---|---|---|---|
| | **RMSE (%)** | **CAX RMSE (%)** | **Beam RMSE (%)** |
| **FBP** | 46.4 | 45.5 | 62.3 |
| **FFT** | 24.6 | 26.0 | 36.8 |

Both the FBP and FFT two-projection reconstruction methods fail to reconstruct the IMRT distribution accurately. The calculated RMSE for the reconstructions was 46% and and 26% for the central axis region and 37% and 62% for the beam region, for the FBP and FFT recontructions respectively. Both a comparsion of the reconstructed distributions to the original image and a comparison of the profiles show the FBP projection suffers from large artefacts occuring at each individual dose gradient, while the FFT reconstruction flattens the dose gradients out, causing the regions of differing dose to become almost indistinguishable. Examples of the reconstructed distributions, and the respective profile comparisons are displayed in Figure 5.9.

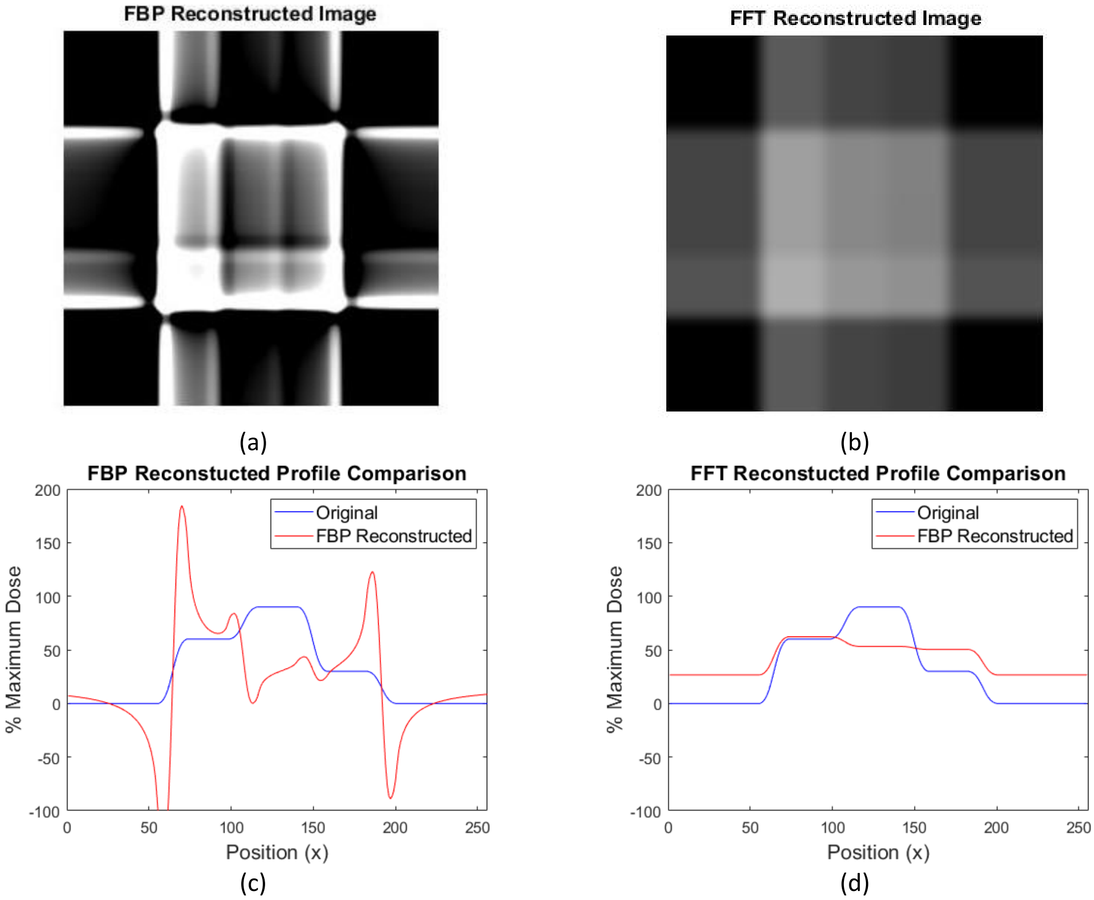

*Figure 5.9.* Two-projection reconstruction of an IMRT dose distribution. The reconstructed images are for a FBP (a) and FFT (b) reconstruction algorithm. Profiles through the centre of the original and reconstructed distributions are shown for the FBP (c) and FFT (d) reconstructions.

From these results, it is concluded that the modelled IMRT distribution is unable to be reconstructed accurately with the two-projection reconstruction method.

## 5.4 Two-Projection Reconstruction Concluding Remarks

### 5.4.1 Filtered Back Projection

Two-projection reconstruction using a filtered back projection algorithm for square and rectangular fields produced large artefacts at the beam edges and an underestimation of the dose at the centre, resulting in CAX reconstruction errors in the magnitude of 20 – 30%. Varying the FBP filter, beam size, beam intensity produced little improvement in the reconstruction quality, but the intensity investigation suggests that the reconstruction error increases for doses below 4 Gy. The reconstruction of circular fields performed better than the square fields for the two-projection reconstruction, but still recorded a reconstruction error of around 6-8%. This is a decrease in performance compared to the single projection reconstructions using the inverse Abel Transform. While the circular field results suggest that a two-projection reconstruction would be able to reconstruct beam features such as penumbra and wedged intensities with no loss of accuracy, the overall reconstruction error is still too high for two-projection FBP reconstruction to be a viable option for the reconstruction of circle fields using the prototype OC dosimeter either.

With this level of accuracy for the two-projection filtered back projection reconstruction for the manually summed data, it was decided not to investigate the reconstruction of the FRED integrated data. As seen in Section 4.3, the projections modelled through FRED contain a high level of noise, representative of the performance of the OC dosimeter, but detrimental to the accuracy of any reconstruction. With high levels of reconstruction error present already, and any improvement with the FRED data fundamentally unlikely, FRED projection reconstructions were not attempted for the two-projection FBP reconstruction technique.

### 5.4.2 Fast Fourier Transform

Two-projection reconstruction using a fast Fourier transform algorithm resulted in an accurate reconstruction for the simple square fields, provided that no additional beam complexities were added. The reconstruction error proved independent of the beam size and noise added, while the error increased significantly when there was any detectable background intensity, indicating that a background correction would be necessary. The reconstruction also did not perform well when any beam penumbra or wedged intensity was added, with large increases in reconstruction error observed. While the reconstruction works well for a perfectly square beam, the reconstruction fails when features of a clinical radiation beam are added. As such, a two-projection reconstruction also does not appear to be a viable option for the 3D reconstruction of square fields using the output of the prototype OC dosimeter. The reconstruction of rectangular and circular fields resulted in persistent levels of reconstruction error, with these fields performing worse than the square field reconstruction for almost all the beam parameters investigated. The two-projection FFT reconstruction of the circle fields resulted in a worse reconstruction than the single projection reconstruction using the inverse Abel Transform, suggesting the single projection technique is the superior option.

With this level of accuracy for the two-projection fast Fourier transform reconstruction for the manually summed data when features of a clinical radiation beam were modelled, it was again decided to not further this investigation with the use of the FRED integrated projection data. Despite the FFT reconstruction appearing relatively insensitive to noise, the high levels of reconstruction error present for the clinical beam models are unlikely to improve using the FRED data. Therefore, FRED projection reconstructions were not attempted for the two-projection FFT reconstruction technique.

### 5.4.3 IMRT Beam Reconstruction

The two-projection reconstruction technique using FBP and FFT algorithms was attempted upon a complex dose distribution with multiple dose levels. As expected, this was beyond the capabilities of a two-projection reconstruction, with reconstruction errors between 25% and 60%. Based on the reconstruction accuracy of simple fields this result was anticipated for a more complex field. But this result allows for the comparison of the multi-projection reconstruction accuracy.

The focus of the next chapter will be to determine what is required to reconstruct the square and IMRT fields to an accurate level. For this, the desire to keep the mechanical complexity of the OC dosimeter design is deemed less crucial, and the number of projections required to achieve a reconstruction to an accuracy of better than 3% will be investigated.

# Chapter 6: Multi-Projection Reconstruction

This chapter focuses on investigating the maximum reconstruction accuracy attainable when the restriction of keeping the mechanical complexity of the prototype 3D dosimeter minimised is relaxed, allowing for the use of many projections. While Chapter 4 has shown that it is possible to reconstruct 3D dose distributions resulting from simple circular radiation fields with low noise, Chapter 5 showed the two-projection FBP and FFT methods failed to reconstruct square fields when complexities representing a clinical radiation field are modelled, or the IMRT field with multiple dose levels. The inverse Abel Transform is unable to reconstruct anything without radial symmetry, making it unsuitable for measuring any of the square fields commonly used in clinical reference dosimetry. This chapter will determine the relationship between the number of projections and the accuracy of the reconstruction of the square, rectangular, circular and IMRT fields.

While the use of many projections is considered undesirable due to the increase in required mechanical complexity of the OC dosimeter design, it is not outside the realms of possibility. The optical components of the dosimeter could be mounted upon a rotating optical platform [118] with the test cell remaining stationary in the centre. As the platform completes a full rotation the object beam would continuously pass through the test cell, allowing projections from any angle to be captured. This would require a cylindrical test cell to be used, to keep the optical path length through the cell the same for each projection, which would require subsequent modification to the reconstruction code to account for the new optical componentry. As the detector would take a finite amount of time to complete a rotation, continuous dose accumulation and/or heat diffusion effects would also need to be considered. The magnitude of the mechanical vibration of the optical components as the platform rotates, and the effect this has on the noise in the dosimeter output would require investigation also. However, while a multi-projection approach would present new technical challenges to overcome (the details of which are outside the scope of this study) it is not an insurmountable challenge.

## 6.1 Projection Number Investigation

The Filtered Back Projection reconstruction algorithm was used for this investigation, due to the ease of utilizing the *radon* [115] and *iradon* [116] functions in MATLAB for different numbers of projections, and the overall better performance as demonstrated in Chapter 5. The performance of a multi-projection reconstruction using the FFT algorithm is a potential area of future work. Code was written so the chosen number of projections were evenly distributed throughout a 180° arc. A 180° arc was chosen as all the projection information can be captured within 180° as the second 180° are just a mirror of the first, so the information density is doubled for the same number of projections. The square, rectangular, circular, and IMRT fields were generated as described in Section 3.1.

Following the findings of the initial FBP investigation in Section 5.5.1, the Hann filter was used as it provided the greatest accuracy. Beams were modelled within a 256x256 array, representing a x-y plane through the 3D dose distribution. Square, circular and the IMRT beams were 128 pixels in size, while the rectangular beam was 160x80 pixels. All beams were given a background value of 0.0 and a nominal dose value of 1.0, while the IMRT beam had a 3x3 checkerboard pattern of varying dose levels. The goal of this multi-projection reconstruction was to determine the number of projections required to reconstruct a clinical beam, so penumbra were added to all beams investigated. The effects that added noise had on the reconstruction accuracy are investigated in section 6.1.2, and wedged intensity fields are investigated in section 6.1.3. Projections through the dose distribution were taken using MATLABs *radon* function, then the FBP reconstruction performed using the *iradon* function.

Reconstruction accuracy was evaluated through the comparison of profiles through the centre of the dose distribution, between the original and reconstructed images. The RMSE between the profiles was calculated, using the same definitions for total RMSE, beam RMSE and CAX RMSE as defined in Section 3.3. In addition, the mean dose in a circular Region of Interest (ROI) 10 pixels in diameter on the beam CAX was measured for both images, and the percentage error between them calculated. The aim of the multi-projection reconstruction investigation was to find the number of projections required to reach a 2% reconstruction error. 2% uncertainty is approximately the level of dosimetric accuracy achievable using current clinical dosimetry protocols such as TRS-398 [32] or AAPM TG-51 [33], so this represents a level of reconstruction accuracy to aim for to ensure the uncertainty in dose determination using the OC dosimeter is similar to current methods.

### 6.1.1 Initial Reconstructions

The Filtered Back Projection reconstruction was performed for different number of projections ranging from 2 to 100, and the reconstruction accuracy metrics recorded for each reconstruction. This was done for square, rectangular, circular, and IMRT modelled photon beams. The reconstruction accuracy as a function of the number of projections used in the FBP reconstruction are plotted in Figure 6.1 below.

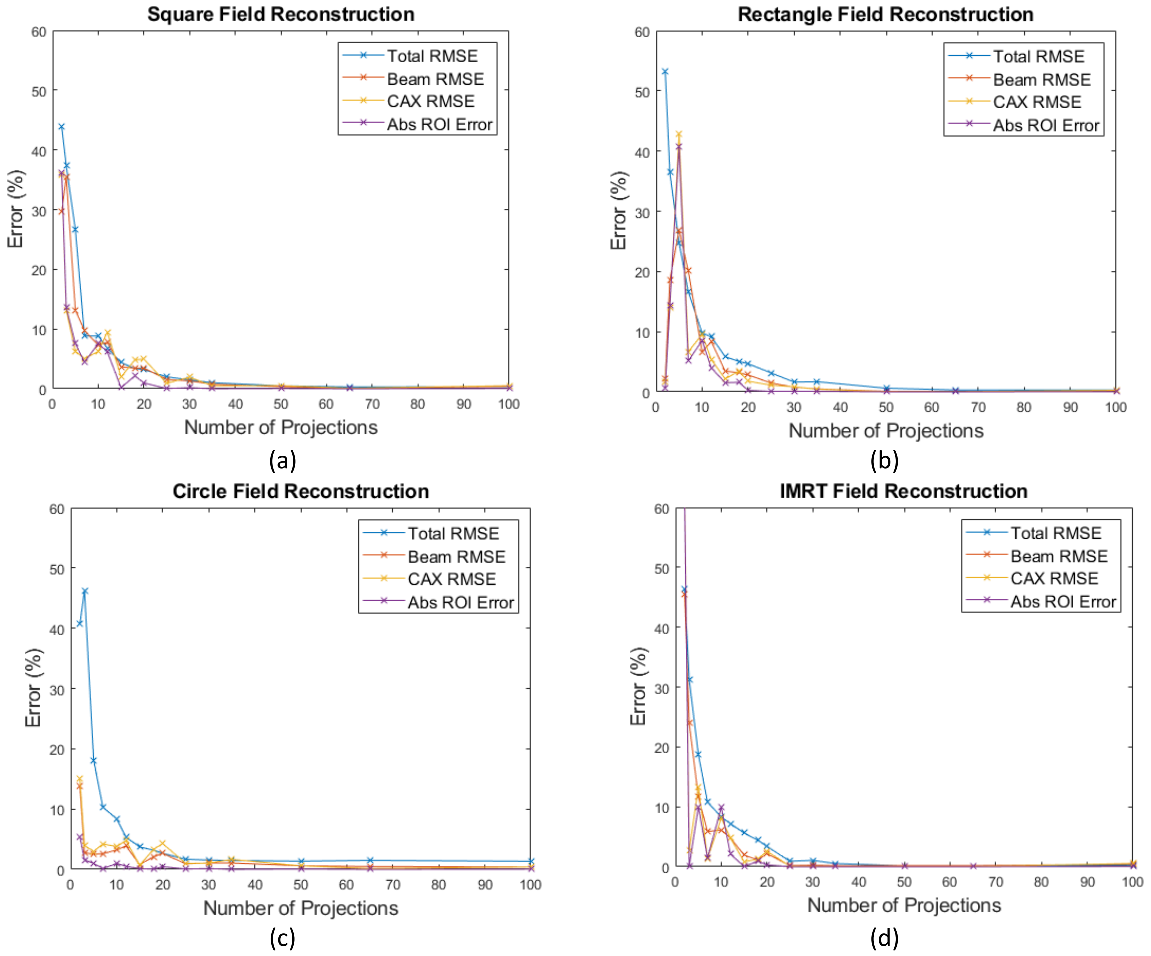

(a) (b) (c) (d)

*Figure 6.1. FBP reconstruction accuracy metrics with increasing numbers of projections. MATLAB modelled square (a), rectangle (b), circle (c), and IMRT (d) photon beams were investigated.*

The results show a predictable and consistent trend across all four beams, with the reconstruction accuracy increasing as the number of projections increase. The calculated error metrics were at their greatest for the reconstructions with low numbered projection reconstructions, with total RMSE errors greater than 30% measured for all fields. Interestingly, the two-projection rectangular beam reconstruction had a very low initial beam RMSE, CAX RMSE, and mean error metrics relative to the other beams. This was a result of the beam edge artefact in the region the accuracy metrics were calculated however, as described in Section 5.1.5, rather than an accurate reconstruction. This is evident from the corresponding large total RMSE for this reconstruction, that not all parts of the beam are being reconstructed accurately.

The reconstructed images for 15, 25 and 50 projections reconstructions are shown in Figure 6.2 for the IMRT field, along with comparisons for the original and reconstructed central profiles for these fields.

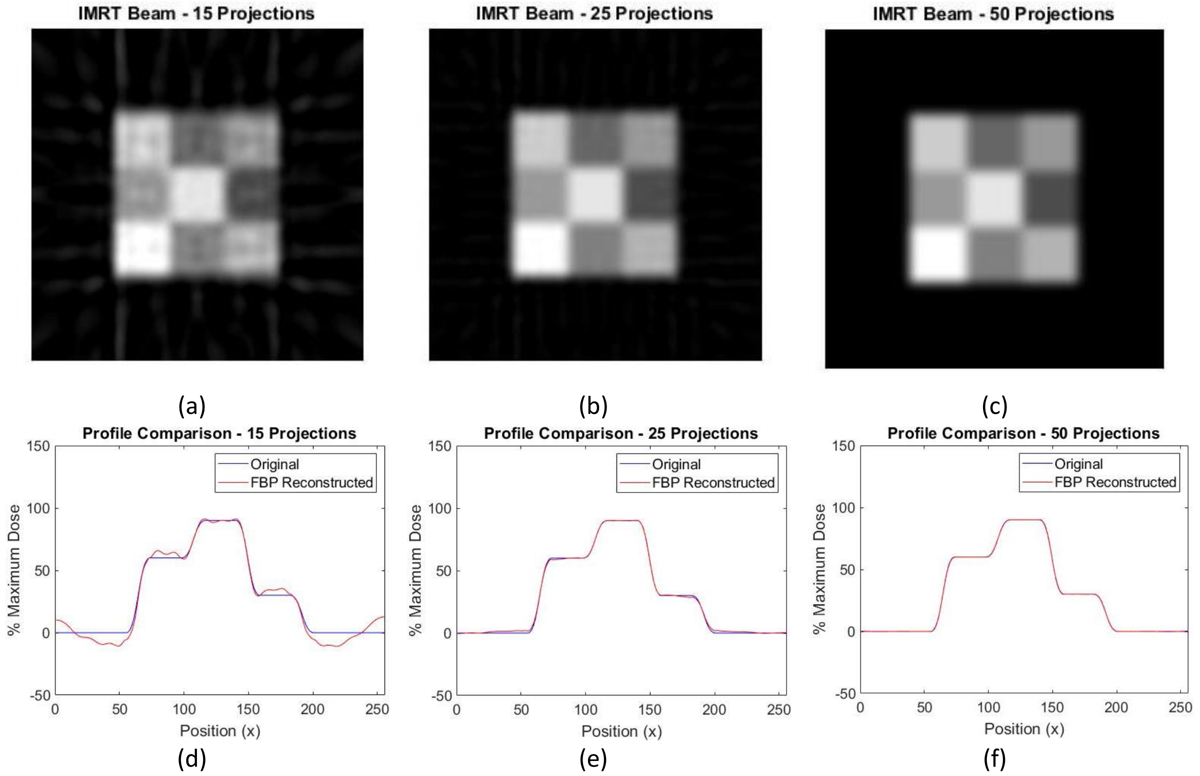

(a) (b) (c)

(d) (e) (f)

*Figure 6.2. Multi-projection IMRT field FBP reconstruction. Reconstructed dose distributions for 15 (a), 25 (b), and 50 (c) projection reconstructions. Profile comparisons between the original and reconstructed distributions for 15 (d), 25 (e), and 50 (f) projection reconstructions.*

As the number of projections increases, the accuracy metrics all show a rapid decrease, with the beam and CAX RMSE reduced to less than 2% and mean ROI error reduced to less than 0.5% by 25 projections for all fields. The reconstruction accuracy then plateaus, with only a gradual increase in accuracy between 25 projections and 100 projections. For the mean ROI errors this plateau reaches zero, indicating that with sufficient projections the mean value of the pixels within the ROI of the reconstructed dose distribution equals the mean of the same pixels in the original image. For the RMSE metrics this plateau never quite reaches zero, with the with the IMRT Beam RMSE reaching 0.2%, the circle Beam RMSE reaching 0.5%, and the square field CAX RMSE reaching 0.7%. This indicates that there are still some residual reconstruction differences in these dose distributions, that are still present regardless of the number of projections. Figure 6.2 shows the increase in reconstruction accuracy with projection number for the IMRT field. Reconstruction artefacts can be clearly seen for all the dose levels in the 15-projection reconstruction. For the 25-projection reconstruction these have reduced, with only slight discrepancies at the interface of each dose level observed. The 50-projection reconstruction profiles show a near exact reconstruction.

### 6.1.2 Beam Noise

The multi-projection reconstruction was then repeated with various levels of random noise was added as a percentage of the maximum dose in the modelled beam, to determine if noise affected the number of projections required to reach a 2% reconstruction accuracy relative to the no-noise reconstruction. The FBP reconstruction was repeated for projections ranging from 2 to 100, for MATLAB modelled square, rectangular, circular and IMRT fields with 0% to 5% noise added. Figure 6.3 shows the reconstruction accuracy as a function of number of projections for the IMRT field, with 2% and 5% noise added to the modelled beam. The level of added noise did not affect the number of projections required to reach the maximum reconstruction accuracy for these simple fields, with minimal improvement seen above 25 projections for all the reconstructed fields as in Section 6.1.2, for all levels of noise modelled. The difference between the mean value of a CAX ROI in the original and reconstructed beam also tended towards zero after 25 projections. But the noise did affect the level of maximum reconstruction accuracy achievable, with the RMSE metric reaching a minimum of 1% for the 2% added noise and 3% for the 5% added noise. These results were similar across all types of modelled beam.

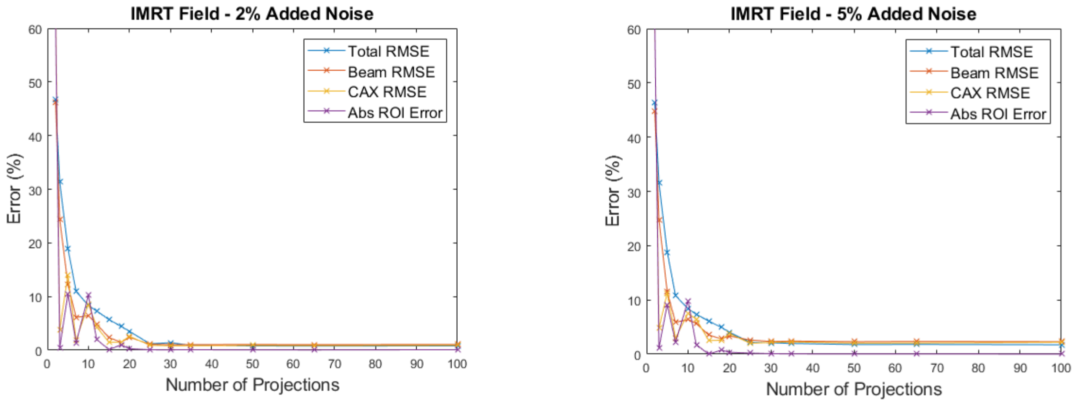

(a) (b)

*Figure 6.3. Multi-projection FBP reconstruction accuracy of an IMRT beam with modelled noise. A MATLAB modelled IMRT photon beam was used, with (a) 2% and (b) 5% noise added.*

The error in the reconstruction after 25 projections as indicated by the RMSE is in the order of half the level of noise that was added to the modelled beam. Figure 6.4 compares profiles through the centre of the original and reconstructed IMRT beam with 5% noise added, for reconstructions with 15, 25 and 50 projections. For the 25 and 50 projection reconstructions, the profiles show the reconstruction performs well at averaging out the noise in the original distribution, producing an approximation of the noise-free profile.

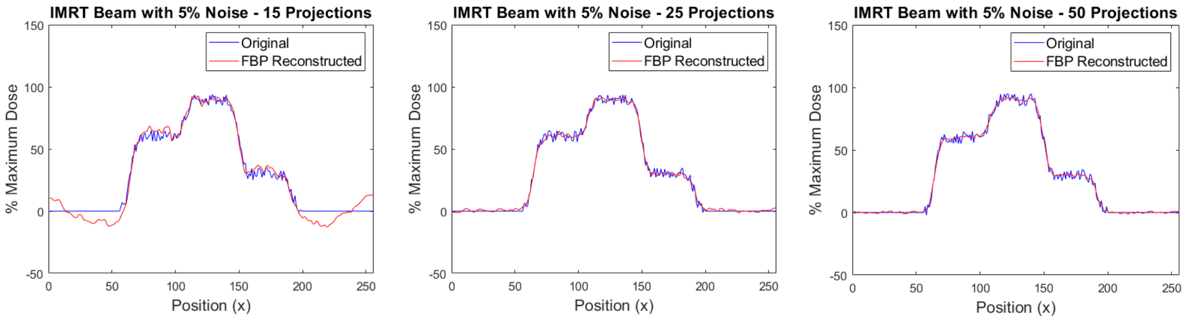

(a) (b) (c)

*Figure 6.4. Multi-projection FBP IMRT beam with noise profile comparison. The original MATLAB modelled IMRT beam and the FBP reconstructed dose distribution profiles are shown for 15 (a), 25 (b), and 50 (c) projection reconstructions, for beams with an additional 5% noise added.*

This, along with the mean ROI difference tending towards zero after 25 projections, suggests that adding noise to the reconstruction did not significantly affect the performance of the multi-projection reconstruction. The number of projections required to achieve a reconstruction to an accuracy of better than 2% remains 25 for noisy data.

### 6.1.3 Wedged Intensity

The final additional beam complexity investigated for the multi-projection reconstruction was the addition of a wedged intensity to the modelled beam. This was added following the methods of section 5.1.6. A wedge was not added to the IMRT beam, as this already contained multiple dose gradients within the radiation beam. The FBP reconstruction was repeated for numbers of projections ranging from 2 to 100, for MATLAB modelled square, rectangular, and circular fields, with wedge angles of 0 to 60° modelled.

The results from this investigation found that the presence of the wedge made no significant difference to the accuracy of the multi-projection reconstruction. The reconstruction accuracy improved rapidly with projection number for all beams, as in Section 6.1.1. This relationship between reconstruction accuracy and number of projections is shown in Figure 6.6 for the square field, with a 30° and 60° wedge angle modelled.

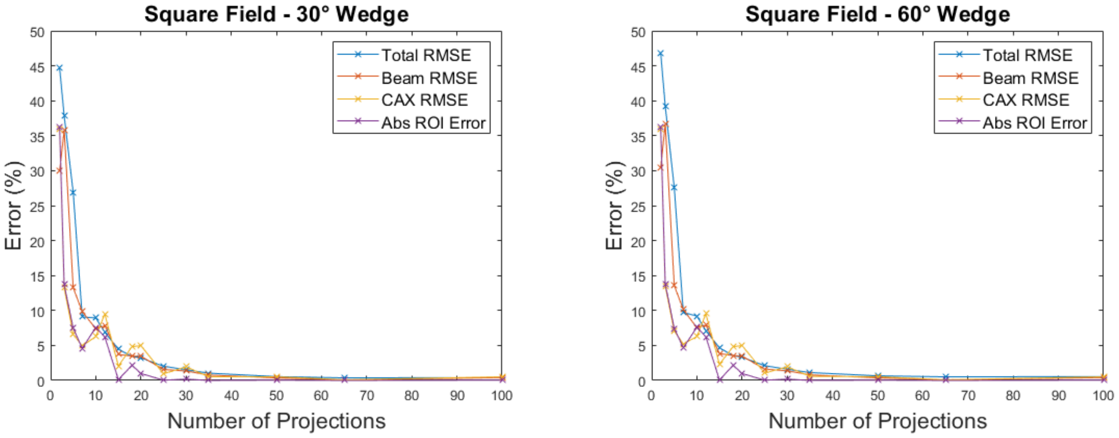

(a) (b)

*Figure 6.5. FBP wedged beam reconstruction accuracy and number of projections. MATLAB modelled wedged square photon beams with a (a) 30° and (b) 60° wedge angle were investigated.*

This accuracy improvement peaks at 25 projections, with the reconstruction accuracy remaining constant with the number of projections beyond this. This can also be seen through analysis of the reconstructed profiles. Shown in Figure 6.5 are the profiles through the reconstructed distribution for a square beam with a 60° wedge modelled, for 15, 25, and 50 projection reconstructions. All the reconstructions accurately account for the wedge angle, but the presence of artefacts in the 15-projection reconstruction reduces the corresponding reconstruction accuracy. These artefacts are reduced in the 25-projection reconstruction and not present in the 50-projection reconstruction.

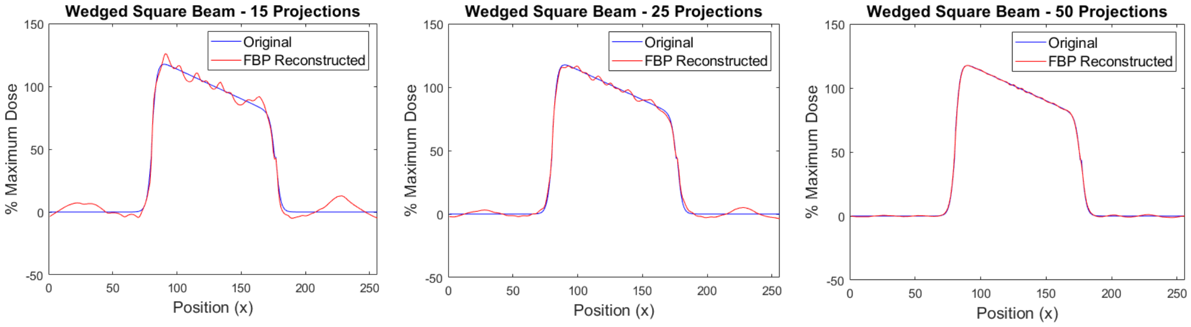

(a) (b) (c)

*Figure 6.6. Multi-projection FBP reconstructed wedged square beam profile comparison. The original MATLAB modelled wedged square beam and the FBP reconstructed dose distributions are shown for 15 (a), 25 (b), and 50 (c) projection reconstructions.*

## 6.2 Concluding Remarks

Square fields representative of clinical radiation beams proved unable to reconstruct accurately with the two-projection FBP or FFT reconstruction, as did the IMRT field and its multiple dose levels, so the number of projections required to achieve an accurate reconstruction of these complex fields was investigated in this chapter. Using a filtered back projection reconstruction algorithm, it was determined that 25 projections was required to reconstruct the IMRT beams with both the RMSE and mean error in a CAX region of interest below 2%. The same result was determined for the square, rectangular and circular beams also. This investigation was repeated for the same radiation beams with additional modelled noise, or a wedged intensity modifier applied and determined the noise and the wedge had no significant impact on the multi-projection FBP reconstruction accuracy. 25 projections remain the threshold for achieving a reconstruction accuracy of better than 2%.

It was decided not to investigate the FFT reconstruction used in this work for the multi-projection method, as the results for the simple fields with features of clinical radiation beams modelled were found to be more reliable for the FBP method, and it is suggested that the FBP reconstruction is expected to perform better than simple Fourier reconstruction methods such as the one implemented in this work. Further research into the FFT reconstruction is a potential area of future work, investigating the performance of a multi-projection FFT reconstruction relative to the FBP, and determining the number of projections required to reach the same level of accuracy.

As a 2% uncertainty is approximately the level of dosimetric accuracy achievable using current clinical dosimetry protocols such as TRS-398 [32] or AAPM TG-51 [33], this represents a level of reconstruction accuracy to aim for to ensure the uncertainty in dose determination using the OC dosimeter is similar to current methods. That 25 projections would be required achieve this level of accuracy for the square and IMRT fields using a FBP reconstruction will be applied to any future modifications to the OC dosimeter if a multi-projection tomographic reconstruction approach is pursued.

# Chapter 7: Discussion

Optical calorimetry is a novel dosimetric technique, that has a potential application in measuring the ultra-high dose rate beams used in emerging therapeutic techniques such as FLASH therapy. One of the features of OC dosimetry is that it outputs a 2D map of integrated dose. Performing a tomographic reconstruction upon this output will produce a 3D dose distribution, and could allow for the dose to be determined at any point within the radiation beam from a single measurement. This would make a 3D OC dosimeter a useful clinical tool, as a single measurement potentially could accurately obtain several important dosimetric quantities used to characterize clinical radiation beams. This would include information on the CAX dose at a range of depths, the 2D distribution of dose at a range of depths allowing for the calculation of flatness and symmetry, and the position of the beam edge and width of the beam penumbra allowing for the determination of beam field sizes. Current clinical methods for acquiring this data involves a number of repeated scanning measurements with an ion chamber or a diode, or careful handling and processing of film with a higher uncertainty in measurement [67]. The OC dosimeter also has advantages over traditional dosimetric methods for the characterisation of ultra-high dose rate FLASH therapy beams, as it avoids the need for a number of correction factors that increases the measurement uncertainty for traditional dosimetric methods in these beams [22]. These factors would position a 3D OC dosimeter as an important clinical dosimetry tool.

An important consideration for the design of a prototype 3D OC dosimeter is the increase in mechanical complexity of the dosimeter required to achieve the tomographic reconstruction. The OC dosimeter relies on extremely precise positioning and alignment of optical components to obtain reliable measurements, so there is a strong desire to minimise any modification to the dosimeter in order to expand its capabilities to measuring in three dimensions. As such, this study primarily focused on investigating the accuracy achievable with no modifications to the dosimeter for a single projection reconstruction using the inverse Abel transform, or for a two orthogonal projection technique using a filtered back projection or a fast Fourier transform algorithm. The reconstruction accuracy for a multiple-projection reconstruction was investigated also, to gain an indication of the number of projections required to achieve a reconstruction accuracy comparable to the uncertainty in current dosimetric methods. If it were decided to follow a multi-projection reconstruction approach, this would allow for the corresponding increase in mechanical complexity required to be estimated.

Current clinical dosimetric methods, such as ionization chamber measurements following international protocols such as IAEA TRS-398 or AAPM TG-51, can achieve measurements of dose with a corresponding uncertainty (k=2) of between 1.5 – 2% for MV photon beams, MeV electron beams, or MeV proton beams at conventional dose rates. For FLASH therapy, the ultra-high dose rate of these beams increases the uncertainty in dose measurement using traditional dosimetric techniques to greater than 5% [22,26,28]. These figures allow the selection of a 2% reconstruction error as a level of accuracy to aim for the tomographic reconstruction process. This target will position the 3D OC dosimeter to measure dose with a level of uncertainty comparable to current dosimetric methods, and better than current UHDR methods, while still considering that the tomographic reconstruction is only one of the sources of uncertainty in the optical calorimetry measurement process.

The reconstruction accuracy achievable for each of the three potential dosimeter designs, and the corresponding impact the designs have on reconstruction accuracy are summarised below, for different levels of complexity in the measured radiation field. How these reconstructions would correspond to the measurement of clinical dosimetric quantities is detailed, along with any limitations inherent to the corresponding reconstruction technique.

## 7.1 Radially Symmetric Field Reconstruction

The radially symmetric fields investigated included TOPAS modelled circular proton beams, and MATLAB modelled circular photon beams. This radial symmetry allows the use of the inverse Abel transform, implemented using the *PyAbel* package in Python, to reconstruct the full 3D distribution from a single projection. Obtaining an accurate 3D reconstruction from a single projection is advantageous for this method as this means the requirement for the OC dosimeter design remains simplified, so the output from the OC dosimeter can be used in its current state with no modifications and corresponding increase in mechanical complexity required. The reconstruction of these beams was investigated using two methods for simulating the dose integration process that occurs in the detector: manually summing the 3D distribution in one dimension, and using the virtual dosimeter model in FRED modelling software.

For the proton beams, the manually summed data were investigated first. The best performing method within the PyAbel package was the Onion Bordas method, capable of achieving a reconstruction error of less than 1% across both the $D_{max}$ profiles and central axis PDDs. This is well within the target 2% reconstruction accuracy, indicating that the inverse Abel transform is potentially a suitable solution for the 3D dosimeter. The effect the beam size had upon reconstruction accuracy was investigated, with similar accuracy found for sizes between 15mm and 40mm but slightly larger errors for the 5mm and 10mm. As detailed in Section 3.1 the absolute beam size is arbitrary, as magnification, minification, and beam expansion techniques could be used to scale the size of the beam image relative to the camera chip, rather it is the pixel resolution relative to the beam size of interest. This reduction in accuracy for the smaller beams suggests that the size of the beam as a proportion of the image array impacts the reconstruction accuracy. When the beam is narrow and less pixels are available for the reconstruction process, this was detrimental to the reconstruction quality. So, it is recommended that the optical componentry setup in the 3D OC dosimeter be arranged such that the imaged beam is no less than one quarter of the image array.

One area that was not investigated in this work was the effect the size the image array had on the reconstruction. As a large range of beams and reconstruction techniques were investigated, the size of the image array was limited to $256^3$ pixels to allow for the reconstruction of the 3D dose distributions within a reasonable timeframe for each beam. But current detector in the OC dosimeter is capable of capturing images at 1280x1024 pixels. One of the findings of Hickstein et al. 2019 was that the reconstruction accuracy of the inverse Abel transform increased as the number of pixels in the reconstructed distribution increases [83]. This was also seen in section 4.1.1, with the accuracy of the Gaussian distribution reconstruction increasing for the 255-pixel distribution relative to the 70-pixel distribution. As such, it is reasonable to expect a full $1024^3$ reconstruction to perform at a higher accuracy than the $256^3$ reconstructions performed here. While these would be more computationally expensive to compute, much of the characterisation of the tomographic reconstruction of these beams has been performed in this work, so a smaller range of beams would be needed to investigate. The effect this had on the reconstruction accuracy would be important information for determining the next steps for the 3D OC dosimeter development, and is an area of future work.

This level of reconstruction accuracy on the manually summed data in Section 4.2 suggests the 3D OC dosimeter has the potential to be well suited for making clinical dosimetry measurements for radially symmetric beams. The high reconstruction accuracy on the central axis suggests suitability for accurately determining dose outputs or measuring PDDs, while the low RMSE and good profile matching suggests accurate measuring of the beam penumbra and field edges. These imply the OC dosimeter can measure dose accurately both dosimetrically and geometrically. One area the OC dosimeter is limited however, would be for measurements of beam flatness and symmetry. As the inverse Abel transform assumes radial symmetry any information on beam asymmetries is averaged out over the beam in the reconstruction process, so no information on any potential flatness or symmetry errors can be gained.

When FRED integrated proton beams were used in Section 4.3, simulating the real-life performance of the OC dosimeter, the resulting projection data showed a large increase in noise relative to the manually summed data. This is representative of the noise that is inherent in the OC dosimeter system currently. Unfortunately, the inverse Abel transform reconstruction appears sensitive to this noise. This is potentially due to the nature of the numerical approximations to the inverse Abel integral of Equation 2.12. Each method within *PyAbel* attempts this approximation in a slightly different way, but commonly involving approximating the function with a series of simpler functions. The high levels of noise in the FRED data likely makes this approximation process less accurate and unreliable, and as a result the quality of the reconstruction is degraded. Attempts at filtering this noise out of the FRED projections were made in Section 4.3, resulting in a reasonable approximation of the manually summed projection, with only small discrepancies between the two evident. But this small discrepancy in the projection data results in large difference in the reconstructed data. Attempts at high levels of filtering were made, but this resulted in a blurring of the beam edge before it improved the central axis accuracy. A part of the utility of a 3D OC dosimeter is the ability to determine both dosimetric and geometric information of the dose distribution resulting from a radiation beam, so this compromise is undesirable. If the aim of the OC dosimeter was focused solely on determination of dose on the CAX, this compromise would be less of an issue. One area of filtering that was not investigated in this study was applying a filter to only the beam region of the projection, to try and improve the CAX accuracy without compromising the bema edge delineation. This is an area of future work, to further investigate filtering the FRED projections to determine of different filters or filtering techniques can improve reconstruction accuracy.

The final investigation of Section 4.3 found that all inverse Abel transform methods returned a near identical reconstruction of the same filtered FRED projection. There were large reconstruction errors, but these errors were the same for all the individual methods. This suggests the limitation on the accuracy of a tomographic reconstruction using the inverse Abel transform on the FRED projection data lies in the noise in the projection data, rather than the Abel transform itself. The high level of noise currently modelled in the virtual OC dosimeter in FRED distorts the projection data too much for the original dose distribution to be accurately determined. To attempt to improve the reconstruction quality, the level of noise in the FRED projections was reduced in Section 4.4, and the reconstruction accuracy was repeated with noise levels ranging between 1/2 and 1/16th of the full modelled noise. This reduction in noise simulates the ongoing and future refinement of OC dosimeter, aiming to improve performance by reducing sources of noise within the OC dosimeter system. This showed a clear improvement when the noise was reduced, with the reconstruction errors reducing from 10 – 20% to 4% for the 1/8th and 1/16th noise levels. This sets a target for the reduction in noise in the OC dosimeter system. For the single projection inverse Abel transform 3D dose reconstruction method to be realised, the level of noise in the OC dosimeter would need to be reduced substantially, to at least 1/8th of the current level of noise.

The use of a single-projection inverse Abel transform tomographic reconstruction is a promising option for a potential 3D OC dosimeter. While the noise levels in the current OC dosimeter mean that further refinement of the OC dosimeter is required before this becomes a possibility, the tomographic reconstruction accuracy showed clear improvement with reducing noise. If this is achieved, this study indicates that a reconstruction both dosimetrically and geometrically accurate is possible, with accurate CAX dose and beam edge determination at all depths within the radiation beam. The single-projection method presents no increase in mechanical complexity to the OC dosimeter design, increasing the ease of implementation. The limitations in this technique lie in it being limited to radially symmetric fields, and unable to resolve flatness and symmetry information from a beam.

The second type of radially symmetric beams investigated were simple circular photon beam models generated in MATLAB. But for all the inverse Abel transform photon beam reconstructions, prominent reconstruction artefacts on the central axis were observed. Aside from these artefacts, the reconstruction for the rest of the profiles were accurate. While the cause of these artifacts was not determined in this study, there is potential for an accurate reconstruction if they can be removed or filtered out. This was not investigated in this study, as the decision was made to focus on the proton beam models to correspond with the likely implementation of the OC dosimeter in FLASH therapy. This remains a potential area of future work.

The reconstruction of radially symmetric fields was also investigated using the two-projection reconstruction method. For this the MATLAB modelled circular beams were used, as these could easily be modified and additional complexities could be added, to characterise the reconstruction accuracy with various features of clinical radiation beams. Both a filtered back projection algorithm and a fast Fourier transform were investigated. While the two-projection method produced some accurate results in some specific cases, like determining the CAX dose for a FBP reconstruction, in general the two-projection method resulted in large reconstruction errors. This does not present a superior option to the single-projection inverse Abel transform for the fields compared. As the two-projection method would require the OC dosimeter be modified to capture two projections from orthogonal angles simultaneously, subsequently increasing the mechanical complexity of the dosimeter, it can be concluded that for radially symmetric fields the single-projection reconstruction using the inverse Abel transform is the better option.

Finally, the multi-projection method was used to investigate the reconstruction of radially symmetric fields. Using a FPB reconstruction, approximately 25-projections were required to achieve a reconstruction error of less than 2%, an accuracy comparable to the ideal performance of the single-projection method, and the level of accuracy in current clinical dosimetry techniques. The multi-projection method could be implemented clinically to determine the CAX dose and the beam edge, and was able to accurately reconstruct beam asymmetries such as a wedge angle. This shows it is capable of determining the flatness and symmetry of a radiation beam, which the single-projection method was not capable of.  The multi-projection method would present the superior tomographic reconstruction option, were it not for the large increase in mechanical complexity of the OC dosimeter required to modify it to capture 25 projections. This compares to capturing a single projection with the current OC dosimeter, with no modifications necessary.

The multi-projection method also appears to be insensitive to added noise, with it capable of reconstructing a radiation beam to the same accuracy when 5% random noise was added. The multi-projection method was not used for the FRED projection data due to time restraints, so determining whether the same level of noise reduction in the OC dosimeter is required to accurately reconstruct the FRED data as the single-projection data required is an area of future work. If the same level of noise reduction was required, then the additional mechanical complexity introduced by the multi-projection method would likely result in the single-projection method being the superior option. But if a lesser, more achievable level of noise reduction is required, then the challenge of the increased mechanical complexity might be preferable to finding further noise reductions.

In conclusion, for the tomographic reconstruction of a radially symmetric radiation field using the OC dosimeter, both the single-projection method and multi-projection method present as viable options, but both would require more work on the OC dosimeter refinement or design to fully implement them. The single-projection method is desirable from a mechanical complexity perspective but requires a reduced level of noise in the OC dosimeter system. The multi-projection method would require the mechanical complexity challenge to be tackled, so is only viable if this method would require smaller improvements to the noise in the dosimeter. Determining this and advising on the direction to take will be the first step of future work for this project.

## 7.2 Square Field Reconstruction

While the one-projection reconstruction method presents a promising reconstruction technique for the reconstruction of radially symmetric 3D dose distributions, this technique is not suitable for any radiation fields that do not have inherent radial symmetry. While this symmetry exists for the FLASH proton beams, a likely application for the OC dosimeter, many current clinical dosimetry practices are based upon the use of square fields [32,33]. To increase the utility of the OC dosimeter, and ensure it is not limited to only radially symmetric fields, the accuracy of reconstructing square fields was investigated.

The simplest modification to the OC dosimeter to potentially enable the reconstruction of square fields is to take two orthogonal projections. This would be easy to construct, with the addition of a second beam splitter to divide the object beam into two. They could then be directed to probe the test cell orthogonally, before recombining with the reference beam at a separate detector for each beam. This would allow for the simultaneous capture of two orthogonal projections, with minimal modification to the OC dosimeter construction. This desire to keep the mechanical complexity of any tomographic OC dosimeter minimised is the key motivation for the two-projection approach. If further projections are required, this would entail a much larger redesign of the optical components within the dosimeter, and alterations to the DHI reconstruction algorithms used to generate the phase map from the interferograms. While two projections are much less than what is used in a typical tomographic reconstruction, the fields being reconstructed are much simpler than the typical image being reconstructed, with only a square region of dose and background outside of that. As such, projections from two orthogonal angles would theoretically contain all the information within the dose distribution. Two-projection reconstructions were performed using filtered back projection and fast Fourier transform reconstruction algorithms.

The FBP reconstruction consistently resulted in reconstruction errors of 30% or more, suggesting a two-projection approach with FBP is not viable. This method could determine the location of the beam edges accurately, which is potentially useful dosimetric information. But without being able to accurately determine the dose within the radiation field, there is nothing to suggest this method would perform better than any of the currently available dosimetry methods. The FFT reconstruction performed much better than the FBP method for very simple square fields but broke down when any beam complexities were modelled. As even the simplest of clinical radiation fields will have noise and penumbra components, this suggests the two-projection method with the FFT reconstruction implemented in this study is not viable either. While the two-projection reconstruction approach is desirable from a mechanical complexity perspective, the corresponding reconstruction accuracy with FBP or FFT reconstruction methods was not to the level required for clinical use of the dosimeter, so these two-projection methods for the reconstruction of square fields is not recommended for future implementation for the OC dosimeter.

Similar to the radially symmetric field, the multi-projection approach was also implemented for the square field reconstruction, also concluding that approximately 25 projections are required to achieve a reconstruction accuracy of better than 2%. While the modification of the OC dosimeter to be capable of taking 25 projections would greatly increase the mechanical complexity, for the case of the square field reconstruction this appears to be necessary, as the two-projection approach was unable to perform this reconstruction to a reasonable accuracy. To determine dosimetric quantities such as CAX dose at different depths or flatness and symmetry from a square field using the OC dosimeter, the multi-projection approach would be required. For the reconstruction of square fields, the multi-projection approach is the recommended option.

## 7.3 Complex Field Reconstruction

The final type of field investigated in this study was the IMRT field, a complex field with a 3x3 checkerboard of different dose levels, creating multiple dose gradients across both dimensions within the radiation beam. While less complex than the dose distribution that would result from a true IMRT field being delivered to a water phantom, the presence of multiple dose levels and dose gradients across both dimensions ensures the main technical difficulties of an IMRT field are represented.

As this field is not radially symmetric, a single projection inverse Abel transform reconstruction was not attempted. Two-projection reconstruction was performed with both the FBP and FFT algorithms, resulting in CAX RMSE of 46% and 26% respectively. The multiple dose gradients presented too much complexity for these to reconstruct accurately, with the FBP reconstruction featuring large artefacts at the boundaries of each dose level, while the FFT reconstruction flattens the individual dose gradients out, reducing the ability to discriminate between the dose levels. This result was expected, from the results of the two-projection reconstruction of simple fields. It is concluded that the two-projection method is unable to accurately reconstruct any radiation beams with complex dose gradients.

To achieve an accurate reconstruction of the complex IMRT field, the multi-projection reconstruction technique was required. Similar to the circular and square field reconstructions, 25 projections were required to achieve a reconstruction accuracy of less than 2%. So, while this approach will involve an increase of the mechanical complexity of the OC dosimeter, it is the only method capable of generating a reconstruction of acceptable accuracy. Therefore, to reconstruct a multi-level 3D dose distribution from an IMRT field using the OC dosimeter, the multi-projection approach is recommended.

## 7.4 Future Work

The first area of future work arising from this study will be to investigate the sensitivity of a multi-projection FBP reconstruction to the noise in the FRED projection data, relative to the single-projection reconstruction using the inverse Abel transform. If the noise sensitivity is similar, then the extra mechanical complexity required for the multi-projection method should result in the single-projection method being the direction to pursue. But if the multi-projection method proves to be impacted less by the noise, then there are two possible immediate next steps for the development of a 3D OC dosimeter: reducing the noise in the OC dosimeter system to at least 1/8th of the current noise level to enhance the single-projection method, or accounting for the additional mechanical complexity in the OC dosimeter design and implementing the multi-projection method. Which is more feasible to achieve between reducing noise and modelling the extra complexity, or whether both are achievable, or neither are achievable, will determine the next step in the development of the 3D OC dosimeter.

One area to help reduce the level of the noise could be further investigation of the filtering of the FRED projection data. Only the uniform and Gaussian filters were tested, and these were applied to the whole projection data, with the limiting factor for the filtering being the increase in error at the beam edge as this became more blurred as the filtering increased. Whether other forms of filtering could be more effective, or applying a filter to only the central region of the projection such that the beam edge resolution is maintained are avenues that could reduce the impact of the noise on the reconstruction of the FRED data.

As detailed in Section 7.1, increasing the size of the image array is another potential avenue for improving reconstruction accuracy. The performance of the inverse Abel transform is expected to increase with the number of pixels in the distribution being reconstructed, due to an increased density of pixels to use in the reconstruction [83]. Increasing the resolution of the dose distributions from $256^3$ could present an easy avenue for increasing the reconstruction accuracy, coming at the cost of increasing the computational requirement of the reconstruction.

Another possible route for improving the reconstruction performance is to further investigate the use of the FFT reconstruction. The Fourier reconstruction algorithm investigated in this study was simple, with the two-projection reconstruction proving capable of perfectly reconstructing basic square fields but showing a decrease in accuracy as additional complexities were added to the modelled beam. Investigating the implementation of more advanced forms of Fourier reconstruction, such as those found in [94,95,119], and determine whether these result in a better reconstruction for more complex fields than the method implemented in this work. The use of the FFT reconstruction in the multi-projection reconstruction analysis was not able to be investigated in the timeframe of this work, so comparing this approach to the FBP approach, and specifically determining whether the target number of projections for reconstruction accuracy of less than 2% is greater or lesser than 25 would help guide the next steps of the 3D OC dosimeter development.

The cause of the CAX artefacts in the inverse Abel transform reconstruction of the MATLAB modelled beams was never fully determined, and avenues for reducing or removing this were not fully explored in this study. Investigating whether modifications to the inverse Abel transform, or using filtering methods to account for this artefact could improve the understanding of using the inverse Abel transform, or the types of filtering that could be effective for this application. Using TOPAS to model some photon dose distributions and contrasting this to the MATBLAB modelled dose distributions could also indicate whether it was the geometry of a photon beam, or the simple nature of the MATLAB beam models that was causing these reconstruction artefacts.

Finally, the application of tomosynthesis or iterative reconstruction algorithms to the reconstruction methods used here should provide improved reconstruction performance compared to the FPB or FFT methods. As described in Section 2.4.4, these advanced reconstruction techniques require more computing resources and are more difficult to implement, so were deemed outside the scope of the initial explorations into 3D OC dosimetry in this study. But these techniques are better performing at low projection numbers than FBP and the FFT [92,96,101]. They could be applied to the two-projection reconstruction method to improve the performance, potentially making this a more viable reconstruction option. Or they could be applied to the multi-projection reconstruction, reducing the number of projections required to achieve a reconstruction accuracy of acceptable quality, and hence potentially decreasing the mechanical complexity obstacle to overcome in the implementation of this multi-projection technique.

# Chapter 8: Conclusion

It is possible to generate three-dimensional dose distributions through tomographic reconstruction of the integrated dose output from an optical calorimetry dosimeter, but achieving a reconstruction of a clinically acceptable accuracy will require further refinement and development of the OC dosimeter. The single-projection reconstruction method using the inverse Abel transform has the potential to deliver accurate reconstructions of radially symmetric beams from the OC dosimeter as currently designed, however the levels of noise in the dosimeter will need to be reduced in order to achieve the desired reconstruction accuracy. The multi-projection reconstruction technique is the only viable technique tested in this study for the reconstruction of square fields, or fields with multiple dose levels. But the implementation of this technique will require modification to the OC dosimeter design to acquire at least 25 projections, at the cost of a large increase in the mechanical complexity of the dosimeter. Determining whether it is more feasible to reduce the noise in the OC dosimeter system to at least 1/8th of its current level or increase the mechanical complexity of the OC dosimeter system will likely decide which of the single-projection or multi-projection techniques is the most viable for the future development and construction of a 3D optical calorimetry dosimeter.

# Bibliography

[1] D. Hanahan, R.A. Weinberg. The Hallmarks of Cancer. *Cell*. 100 (2000) 57–70.

[2] H. Sung, J. Ferlay, R.L. Siegel, M. Laversanne, I. Soerjomataram, A. Jemal, F. Bray. Global Cancer Statistics 2020: GLOBOCAN Estimates of Incidence and Mortality Worldwide for 36 Cancers in 185 Countries. *CA: A Cancer Journal for Clinicians*. 71 (2021) 209–249.

[3] Ministry of Health. Cancer: Historical summary 1948 – 2017. Wellington: Ministry of Health. https://Www.Health.Govt.Nz/Publication/Cancer-Historical-Summary-1948-2017. (2020).

[4] New Zealand. Ministry of Health., Craig. Wright, Rebecca. Hislop. The price of cancer: the public price of registered cancer in New Zealand. Ministry of Health, 2011.

[5] L.G. Gomella, J. Johannes, E.J. Trabulsi. Current Prostate Cancer Treatments: Effect on Quality of Life. *Urology*. 73 (2009) S28–S35.

[6] A.J. Kerr, D. Dodwell, P. McGale, F. Holt, F. Duane, G. Mannu, S.C. Darby, C.W. Taylor. Adjuvant and neoadjuvant breast cancer treatments: A systematic review of their effects on mortality. *Cancer Treatment Reviews*. 105 (2022) 102375.

[7] J. Gomez-Millan. Radiation therapy in the elderly: More side effects and complications*? Critical Reviews in Oncology/Hematology*. 71 (2009) 70–78.

[8] J.S. Cooper, K. Fu, J. Marks, S. Silverman. Late effects of radiation therapy in the head and neck region*. International Journal of Radiation Oncology*Biology*Physics*. 31 (1995) 1141–1164.

[9] G. Delaney, S. Jacob, C. Featherstone, M. Barton. The role of radiotherapy in cancer treatment: Estimating optimal utilization from a review of evidence-based clinical guidelines. *Cancer*. 104 (2005) 1129–1137.

[10] R. Baskar, K.A. Lee, R. Yeo, K.-W. Yeoh. Cancer and Radiation Therapy: Current Advances and Future Directions*. International Journal of Medical Sciences*. 9 (2012) 193–199.

[11] S.M. Bentzen, L.S. Constine, J.O. Deasy, A. Eisbruch, A. Jackson, L.B. Marks, R.K. ten Haken, E.D. Yorke. Quantitative Analyses of Normal Tissue Effects in the Clinic (QUANTEC): An Introduction to the Scientific Issues*. International Journal of Radiation Oncology*Biology*Physics*. 76 (2010) S3–S9.

[12] L.G. Gomella, J. Johannes, E.J. Trabulsi. Current Prostate Cancer Treatments: Effect on Quality of Life. *Urology*. 73 (2009) S28–S35.

[13] A.E. Kayl, C.A. Meyers. Side-effects of chemotherapy and quality of life in ovarian and breast cancer patients*. Current Opinion in Obstetrics & Gynecology.* 18 (2006) 24–28.

[14] K. Nakamura, T. Sasaki, S. Ohga, T. Yoshitake, K. Terashima, K. Asai, K. Matsumoto, Y. Shioyama, H. Honda. Recent advances in radiation oncology: intensity-modulated radiotherapy, a clinical perspective*. International Journal of Clinical Oncology*. 19 (2014) 564–569.

[15] M. Teoh, C.H. Clark, K. Wood, S. Whitaker, A. Nisbet. Volumetric modulated arc therapy: a review of current literature and clinical use in practice. *The British Journal of Radiology*. 84 (2011) 967–996.

[16] International Commission on Radiation Units and Measurements. *ICRU Report 29: Dose specification for reporting external beam therapy with photons and electrons.* Bethesda, MD, 1978.

[17] International Commission on Radiation Units and Measurements. *ICRU Report 50: Prescribing, recording, and reporting photon beam therapy*. Bethesda, MD, 1993.

[18] International Commission on Radiation Units and Measurements. *ICRU Report 62: Prescribing, recording, and reporting photon beam therapy, Supplement to ICRU Report No. 50*. Bethesda, MD, 1999.

[19] C. Chargari, N. Magne, J.-B. Guy, C. Rancoule, A. Levy, K.A. Goodman, E. Deutsch. Optimize and refine therapeutic index in radiation therapy: Overview of a century. *Cancer Treatment Reviews*. 45 (2016) 58–67.

[20] M. Beasley. Complications of radiotherapy: improving the therapeutic index. *Cancer Imaging*. 5 (2005) 78–84.

[21] International Atomic Energy Agency. Accuracy Requirements and Uncertainties in Radiotherapy. *IAEA Human Health Series No. 31*, Vienna, 2016.

[22] N. Esplen, M.S. Mendonca, M. Bazalova-Carter. Physics and biology of ultrahigh dose-rate (FLASH) radiotherapy: A topical review. Physics in Medicine and Biology. 65 (2020).

[23] J.R. Hughes, J.L. Parsons. Flash radiotherapy: Current knowledge and future insights using proton-beam therapy. *International Journal of Molecular Sciences*. 21 (2020) 1–14.

[24] S. Jolly, H. Owen, M. Schippers, C. Welsch. Technical challenges for FLASH proton therapy. *Physica Medica*. 78 (2020) 71–82.

[25] M. Marinelli, G. Felici, F. Galante, A. Gasparini, L. Giuliano, S. Heinrich, M. Pacitti, G. Prestopino, V. Vanreusel, D. Verellen, C. Verona, G. Verona Rinati. Design, realization, and characterization of a novel diamond detector prototype for FLASH radiotherapy dosimetry. *Medical Physics*. 49 (2022)

[26] K. Kokurewicz, A. Schüller, E. Brunetti, A. Subiel, R. Kranzer, T. Hackel, M. Meier, R.P. Kapsch, D.A. Jaroszynski. Dosimetry for New Radiation Therapy Approaches Using High Energy Electron Accelerators. *Frontiers in Physics*. 8 (2020).

[27] F. di Martino, P. Barca, S. Barone, E. Bortoli, R. Borgheresi, S. de Stefano, M. di Francesco, L. Grasso, G. Lucia, S. Linsalata, D. Marfisi, M. Pacitti, G. Felici, L. Faillace. FLASH Radiotherapy With Electrons: Issues Related to the Production, Monitoring, and Dosimetric Characterization of the Beam. *Frontiers in Physics*. 8 (2020).

[28] S. Szpala, V. Huang, Y. Zhao, A. Kyle, A. Minchinton, T. Karan, K. Kohli. Dosimetry with a clinical linac adapted to FLASH electron beams. *Journal of Applied Clinical Medical Physics*. 22 (2021) 50–59.

[29] M. McManus, F. Romano, N.D. Lee, W. Farabolini, A. Gilardi, G. Royle, H. Palmans, A. Subiel. The challenge of ionisation chamber dosimetry in ultra-short pulsed high dose-rate Very High Energy Electron beams. *Scientific Reports*. 10 (2020) 9089.

[30] International Commission on Radiation Units and Measurements. *ICRU Report 71: Prescribing, recording, and reporting electron beam therapy*. Bethesda, MD, 2004.

[31] INTERNATIONAL ATOMIC ENERGY AGENCY. Accuracy Requirements and Uncertainties in Radiotherapy. *IAEA Human Health Series No. 31*, Vienna, 2016.

[32] International Atomic Energy Agency. *IAEA TRS-398: Absorbed Dose Determination in External Beam Radiotherapy.* Vienna, Austria, 2000.

[33] P.R. Almond, P.J. Biggs, B.M. Coursey, W.F. Hanson, M.S. Huq, R. Nath, D.W.O. Rogers. AAPM's TG-51 protocol for clinical reference dosimetry of high-energy photon and electron beams. *Medical Physics*. 26 (1999) 1847–1870.

[34] International Commission on Radiation Units and Measurements. ICRU Report 44: Tissue Substitutes in Radiation Dosimetry and Measurement. Bethesda, MD, 1989.

[35] B. Chauvenet, D. Baltès, F. Delaunay. Comparison of graphite-to-water absorbed-dose transfers for Co photon beams using ionometry and Fricke dosimetry. *Physics in Medicine and Biology*. 42 (1997) 2053–2063.

[36] A. Cavan, J. Meyer. Digital holographic interferometry: A novel optical calorimetry technique for radiation dosimetry. *Medical Physics*. 41 (2014).

[37] L. Hubley, J. Roberts, J. Meyer, A. Moggré, S. Marsh. Optical-radiation-calorimeter refinement by virtual-sensitivity analysis. *Sensors (Switzerland).* 19 (2019).

[38] J. Renaud, H. Palmans, A. Sarfehnia, J. Seuntjens. Absorbed dose calorimetry. *Physics in Medicine & Biology*. 65 (2020) 05TR02.

[39] P.J. Allisy, D.T. Burns, P. Andreo. International framework of traceability for radiation dosimetry quantities. *Metrologia*. 46 (2009) S1–S8.

[40] C.K. Ross, N. v Klassen. Water calorimetry for radiation dosimetry. *Physics in Medicine and Biology*. 41 (1996) 1–29.

[41] E. Flores-Martinez, M.J. Malin, J. Radtke, L.A. DeWerd. Challenges and opportunities in calorimetry for clinical radiation dosimetry. *AIP Conference Proceedings*. 1747 (2016) 110001

[42] P.R. Almond, H. Svensson. Ionization Chamber Dosimetry for Photon and Electron Beams. *Acta Radiologica: Therapy, Physics, Biology*. 16 (1977) 177–186.

[43] A. Nisbet, D.I. Thwaites. Polarity and ion recombination correction factors for ionization chambers employed in electron beam dosimetry. *Physics in Medicine and Biology*. 43 (1998) 435–443.

[44] A.S. Guerra, R.F. Laitano, M. Pimpinella. Experimental determination of the beam quality dependence factors, kQ, for ionization chambers used in photon and electron dosimetry. *Physics in Medicine and Biology*. 40 (1995) 1177–1190.

[45] G. Martin-Martin, P.B. Aguilar, B. Barbés, E. Guibelalde. Assessment of ion recombination correction and polarity effects for specific ionization chambers in flattening-filter-free photon beams. *Physica Medica*. 67 (2019) 176–184.

[46] K. Zink, J. Wulff. Beam quality corrections for parallel-plate ion chambers in electron reference dosimetry. *Physics in Medicine and Biology*. 57 (2012) 1831–1854.

[47] L.J. Schreiner. Review of Fricke gel dosimeters. *Journal of Physics: Conference Series*. 3 (2004) 9–21.

[48] S. Devic, N. Tomic, D. Lewis. Reference radiochromic film dosimetry: Review of technical aspects. *Physica Medica*. 32 (2016) 541–556.

[49] S. Devic. Radiochromic film dosimetry: Past, present, and future. *Physica Medica.* 27 (2011) 122–134.

[50] A. Niroomand-Rad, S. Chiu-Tsao, M.P. Grams, D.F. Lewis, C.G. Soares, L.J. van Battum, I.J. Das, S. Trichter, M.W. Kissick, G. Massillon-JL, P.E. Alvarez, M.F. Chan. Report of AAPM Task Group 235 Radiochromic Film Dosimetry: An Update to TG-55. *Medical Physics*. 47 (2020) 5986–6025.

[51] E.K. Hussmann. A Holographic Interferometer for Measuring Radiation Energy Deposition Profiles in Transparent Liquids. *Applied Optics*. 10 (1971) 182.

[52] E.K. Hussmann, W.L. McLaughlin. Dose-Distribution Measurement of High-Intensity Pulsed Radiation by Means of Holographic Interferometry. *Radiation Research*. 47 (1971) 1.

[53] A. Miller, E.K. Hussmann, W.L. McLaughlin. Interferometer for measuring fast changes of refractive index and temperature in transparent liquids. *Review of Scientific Instruments*. 46 (1975) 1635–1638.

[54] A. Miller. Holography and interferometry in dosimetry. *Nukleonika*. 24 (1979) 907–925.

[55] A. Cavan, J. Meyer. A novel optical calorimetry dosimetry approach applied to an HDR Brachytherapy source. *Journal of Physics: Conference Series.* 444 (2013) 012069.

[56] J. Roberts, A. Moggré, S. Marsh, J. Meyer. Optical Calorimetry for Radiation Dosimetry. in: *NZPEM*, 2020.

[57] J. Roberts, A. Moggré, S. Marsh, M. Juergen. Optical Calorimetry for Radiation Dosimetry. in: *AAPM*, 2020.

[58] J. Roberts, A. Moggré, S. Marsh, J. Meyer. Converting a Decommissioned Linear Accelerator to Deliver Ultra-High Dose Rates. in: *NZPEM*, 2021.

[59] J. Roberts, A. Moggré, S. Marsh, J. Meyer. Optical Calorimetry, a Promising Dosimetry Technique for FLASH Radiotherapy. in: *FRPT*, 2021.

[60] R.F. Laitano, A.S. Guerra, M. Pimpinella, C. Caporali, A. Petrucci. Charge collection efficiency in ionization chambers exposed to electron beams with high dose per pulse. *Physics in Medicine and Biology*. 51 (2006) 6419–6436.

[61] P. Hariharan. Optical interferometry. *Reports on Progress in Physics*. 54 (1991) 339–390.

[62] T. Kries. *Handbook of Holographic Interferometry: Optical and Digital Methods*. Wiley-VCH, Weinham, 2005.

[63] U. Schnars, W.P.O. Jüptner. Digital recording and reconstruction of holograms in hologram interferometry and shearography. *Applied Optics*. 33 (1994) 4373.

[64] U. Schnars, W. Jueptner. *Digital Holography*. Springer, 2005.

[65] A.N. Bashkatov, E.A. Genina. Water refractive index in dependence on temperature and wavelength: a simple approximation. in: *Proceedings of the SPIE*, 2003: pp. 393–395.

[66] D. Lide. *CRC Handbook of Chemistry and Physics.* Boca Raton, FL, 2005.

[67] I.J. Das, C.-W. Cheng, R.J. Watts, A. Ahnesjö, J. Gibbons, X.A. Li, J. Lowenstein, R.K. Mitra, W.E. Simon, T.C. Zhu. Accelerator beam data commissioning equipment and procedures: Report of the TG-106 of the Therapy Physics Committee of the AAPM. *Medical Physics*. 35 (2008) 4186–4215.

[68] H. Paganetti, E. Blakely, A. Carabe-Fernandez, D.J. Carlson, I.J. Das, L. Dong, D. Grosshans, K.D. Held, R. Mohan, V. Moiseenko, A. Niemierko, R.D. Stewart, H. Willers. Report of the AAPM TG-256 on the relative biological effectiveness of proton beams in radiation therapy. *Medical Physics*. 46 (2019) e53–e78.

[69] S. Vynckier, D.E. Bonnett, D.T.L. Jones. Code of practice for clinical proton dosimetry. *Radiotherapy and Oncology*. 20 (1991) 53–63.

[70] International Electrotechnical Commission. *IEC 60976: Medical electrical equipment - Medical electron accelerators - Functional performance characteristics.* Geneva, Switzerland, 2007.

[71] B. Arjomandy, P. Taylor, C. Ainsley, S. Safai, N. Sahoo, M. Pankuch, J.B. Farr, S. Yong Park, E. Klein, J. Flanz, E.D. Yorke, D. Followill, Y. Kase. AAPM task group 224: Comprehensive proton therapy machine quality assurance. *Medical Physics*. 46 (2019).

[72] International Commission on Radiation Units and Measurements. *ICRU Report 78: Prescribing, Recording, and Reporting Proton-Beam Therapy*. Glasglow, UK, 2007.

[73] International Commission on Radiation Units and Measurements. *ICRU Report 24: Determination of Absorbed Dose in a Patient Irradiated by Beams of X or Gamma Rays in Radiotherapy Procedures.* Bethesda, MD, 1976.

[74] G. Pretzier. A New Method For Numerical Abel-Inversion*.* *Z. Naturforsch*. 46a (1991) 639–641.

[75] F. Cignoli, S. de Iuliis, V. Manta, G. Zizak. Two-dimensional two-wavelength emission technique for soot diagnostics. *Applied Optics*. 40 (2001) 5370.

[76] J. Glasser, J. Chapelle, J. Boettner. Abel Inversion Applied to Plasma Spectroscopy: a New Interactive Method*.* *Applied Optics*. 17 (1978) 3750–3754.

[77] D.W. Chandler, P.L. Houston. Two-dimensional imaging of state-selected photodissociation products detected by multiphoton ionization. *The Journal of Chemical Physics*. 87 (1987) 1445–1447.

[78] G.A. Garcia, L. Nahon, I. Powis. Two-dimensional charged particle image inversion using a polar basis function expansion. *Review of Scientific Instruments.* 75 (2004) 4989–4996.

[79] V. Dribinski, A. Ossadtchi, V.A. Mandelshtam, H. Reisler. Reconstruction of Abel-transformable images: The Gaussian basis-set expansion Abel transform method. *Review of Scientific Instruments*. 73 (2002) 2634–2642.

[80] E.W. Hansen, P.-L. Law. Recursive methods for computing the Abel transform and its inverse. *Journal of the Optical Society of America*. 2 (1985) 510.

[81] C.J. Dasch. One-dimensional tomography: a comparison of Abel, onion-peeling, and filtered backprojection methods. *Applied Optics*. 31 (1992) 1146.

[82] K.J. Daun, K.A. Thomson, F. Liu, G.J. Smallwood. Deconvolution of axisymmetric flame properties using Tikhonov regularization. *Applied Optics*. 45 (2006) 4638.

[83] D.D. Hickstein, S.T. Gibson, R. Yurchak, D.D. Das, M. Ryazanov. A direct comparison of high-speed methods for the numerical Abel transform*.* *Review of Scientific Instruments*. 90 (2019) 065115.

[84] S. Gibson, D.D. Hickstein, R. Yurchak, M. Ryazanov, D. Das, G. Shih. PyAbel/PyAbel: v0.8.5. https://pyabel.readthedocs.io/en/latest/, 2022. Accessed February 2022.

[85] C. Bordas, F. Paulig, H. Helm, D.L. Huestis. Photoelectron imaging spectrometry: Principle and inversion method. *Review of Scientific Instruments*. 67 (1996) 2257–2268.

[86] R. Yurchak. Direct iabel/fabel implementation. https://Github.Com/PyAbel/PyAbel/Pull/52. 2015. Accessed October 2021.

[87] M.R. Ashraf, M. Rahman, R. Zhang, X. Cao, B.B. Williams, P.J. Hoopes, D.J. Gladstone, B.W. Pogue, P. Bruza. Technical Note: Single-pulse beam characterization for FLASH-RT using optical imaging in a water tank. *Medical Physics*. 48 (2021) 2673–2681.

[88] P. van Marlen, M. Dahele, M. Folkerts, E. Abel, B.J. Slotman, W.F.A.R. Verbakel. Bringing FLASH to the Clinic: Treatment Planning Considerations for Ultrahigh Dose-Rate Proton Beams. *International Journal of Radiation Oncology Biology Physics*. 106 (2020) 621–629.

[89] D. Slatkin, P. Spanne, F. Dilmanian, M. Sandborg. Microbeam radiation therapy. *Medical Physics*. 19 (1992) 1395–1400.

[90] T.S. Durrani, D. Bisset. The Radon transform and its properties. *GEOPHYSICS*. 49 (1984) 1180–1187.

[91] G. Beylkin. Discrete radon transform. *IEEE Transactions on Acoustics, Speech, and Signal Processing*. 35 (1987) 162–172.

[92] M.J. Willemink, P.B. Noël. The evolution of image reconstruction for CT—from filtered back projection to artificial intelligence. *European Radiology*. 29 (2019) 2185–2195.

[93] H. Stark, J. Woods, I. Paul, R. Hingorani. Direct Fourier reconstruction in computer tomography. *IEEE Transactions on Acoustics, Speech, and Signal Processing*. 29 (1981) 237–245.

[94] D. Gottleib, B. Gustafsson, P. Forssen. On the direct Fourier method for computer tomography. *IEEE Transactions on Medical Imaging*. 19 (2000) 223–232.

[95] S.S. Chandra, N. Normand, A. Kingston, J. Guedon, I. Svalbe. Robust Digital Image Reconstruction via the Discrete Fourier Slice Theorem. *IEEE Signal Processing Letters*. 21 (2014) 682–686.

[96] M. Beister, D. Kolditz, W.A. Kalender. Iterative reconstruction methods in X-ray CT. *Physica Medica.* 28 (2012) 94–108.

[97] A. Padole, R.D. Ali Khawaja, M.K. Kalra, S. Singh. CT Radiation Dose and Iterative Reconstruction Techniques. *American Journal of Roentgenology*. 204 (2015) W384–W392.

[98] J.T. Dobbins, H.P. McAdams. Chest tomosynthesis: Technical principles and clinical update. *European Journal of Radiology*. 72 (2009) 244–251.

[99] I. Sechopoulos. A review of breast tomosynthesis. Part I. The image acquisition process. *Medical Physics*. 40 (2013) 014301.

[100] J.T. Dobbins. Tomosynthesis imaging: At a translational crossroads. *Medical Physics*. 36 (2009) 1956–1967.

[101] J.T. Dobbins, D.J. Godfrey. Digital x-ray tomosynthesis: current state of the art and clinical potential. *Physics in Medicine and Biology*. 48 (2003) R65–R106.

[102] J. Perl, J. Shin, J. Schümann, B. Faddegon, H. Paganetti. TOPAS: An innovative proton Monte Carlo platform for research and clinical applications. *Medical Physics*. 39 (2012) 6818–6837.

[103] B. Faddegon, J. Ramos-Méndez, J. Schuemann, A. McNamara, J. Shin, J. Perl, H. Paganetti. The TOPAS tool for particle simulation, a Monte Carlo simulation tool for physics, biology and clinical research. *Physica Medica*. 72 (2020) 114–121.

[104] M. Testa, J. Schümann, H.-M. Lu, J. Shin, B. Faddegon, J. Perl, H. Paganetti. Experimental validation of the TOPAS Monte Carlo system for passive scattering proton therapy. *Medical Physics*. 40 (2013) 121719.

[105] H. Liu, Z. Li, R. Slopsema, L. Hong, X. Pei, X.G. Xu. TOPAS Monte Carlo simulation for double scattering proton therapy and dosimetric evaluation. *Physica Medica*. 62 (2019) 53–62.

[106] K.-S. Baumann, S. Kaupa, C. Bach, R. Engenhart-Cabillic, K. Zink. Monte Carlo calculation of beam quality correction factors in proton beams using TOPAS/GEANT4. *Physics in Medicine & Biology*. 65 (2020) 055015.

[107] F. Berumen, Y. Ma, J. Ramos-Méndez, J. Perl, L. Beaulieu. Validation of the TOPAS Monte Carlo toolkit for HDR brachytherapy simulations. *Brachytherapy*. 20 (2021) 911–921.

[108] H. Liu, J.Y. Chang. Proton therapy in clinical practice. *Chinese Journal of Cancer*. 30 (2011) 315–326.

[109] I.J. Das, C.-W. Cheng, R.J. Watts, A. Ahnesjö, J. Gibbons, X.A. Li, J. Lowenstein, R.K. Mitra, W.E. Simon, T.C. Zhu. Accelerator beam data commissioning equipment and procedures: Report of

the TG-106 of the Therapy Physics Committee of the AAPM. *Medical Physics*. 35 (2008) 4186–4215.

[110] H. Paganetti, E. Blakely, A. Carabe-Fernandez, D.J. Carlson, I.J. Das, L. Dong, D. Grosshans, K.D. Held, R. Mohan, V. Moiseenko, A. Niemierko, R.D. Stewart, H. Willers. Report of the AAPM TG-256 on the relative biological effectiveness of proton beams in radiation therapy. *Medical Physics*. 46 (2019) e53–e78.

[111] S. Vynckier, D.E. Bonnett, D.T.L. Jones. Code of practice for clinical proton dosimetry. *Radiotherapy and Oncology*. 20 (1991) 53–63.

[112] H. Liu, J.Y. Chang Proton therapy in clinical practice. *Chinese Journal of Cancer*. 30 (2011) 315–326.

[113] G.A. Mastin. Adaptive filters for digital image noise smoothing: An evaluation*. Computer Vision, Graphics, and Image Processing*. 31 (1985) 103–121.

[114] P. Kowalski, R. Smyk. Review and comparison of smoothing algorithms for one-dimensional data noise reduction. In: 2018 International Interdisciplinary PhD Workshop (IIPhDW), *IEEE*, 2018: pp. 277–281.

[115] The MathWorks Inc., radon - Radon transform, https://Au.Mathworks.Com/Help/Images/Ref/Radon.Html. Accessed June 2020.

[116] The MathWorks Inc., iradon - Inverse Radon transform, https://Au.Mathworks.Com/Help/Images/Ref/Iradon.Html. Accessed June 2020.

[117] C. Onal, A. Sonmez, G. Arslan, E. Oymak, A. Kotek, E. Efe, S. Sonmez, Y. Dolek. Dosimetric comparison of the field-in-field technique and tangential wedged beams for breast irradiation. *Japanese Journal of Radiology*. 30 (2012) 218–226.

[118] T. Zhang, J. Bi, Y. Zhi, J. Peng, L. Chen, L. Li. A two-axis tilt control system on a turntable for rotating-optical-cavity experiments. *Review of Scientific Instruments*. 89 (2018) 125120.

[119] J. Walden. Analysis of the direct Fourier method for computer tomography. *IEEE Transactions on Medical Imaging*. 19 (2000) 211–222.